Nanopore/Nanotube Pattern Formation through Focused Ion Beam Guided Anodization

Zhipeng Tian

Thesis submitted to the faculty of the
Virginia Polytechnic Institute and State University
in partial fulfillment of the requirements for the degree of

MASTER OF SCIENCE

In

Materials Science and Engineering

Kathy Lu, Chair

David Clark

Alex O. Aning

Keywords: Anodization, Focused Ion Beam, Patterning, Porous Aluminum Oxide, Titania Nanotube

December 1, 2010
Blacksburg, VA

Nanopore/Nanotube Pattern Formation through Focused Ion Beam Guided Anodization

Zhipeng Tian

Abstract

Anodization is a kind of method that can produce oxide layer in a large area and on flexible shaped metals. In some specific conditions, anodic oxide layers exhibit interesting nanopore/nanotube structures. In this work, focused ion beam patterning method is introduced to general anodization, aiming to make highly ordered anodic porous alumina and titania nanotubes.

Focused ion beam guided porous anodic alumina is carried out by pre-designing hexagonal and square guiding patterns with different interpore distances on well electropolished Al foil before anodization. After anodization, the guiding interpore distance is found to affect the new pores' locations and shapes. Two important elements, electrical field and mechanical stress, are discussed for the development of the guiding pores and the generation of new pores. Based on the proposed pore growth mechanism, novel patterns, non-spherical pores, and large patterns across the grain boundaries are successfully produced.

The research on focused ion beam guided anodic titania nanotubes begins with surface polishing. The influence of four polishing conditions, as-received, chemically polished, mechanically polished, and electropolished samples, are investigated. A polished smooth sample provides a desired surface for focused ion beam guided anodization. Hexagonal guiding patterns with different interpore distances are created on Ti surface. Ordered nanotube arrays are produced, and the structure of the anodized guiding pattern is identified.

Acknowledgements

First of all, I would like to express my deep gratitude to my advisor, Dr. Kathy Lu, for bring me to her group. You give me the first chance to experience the research in the USA, which I will cherish all over my life. Thank you very much for your professional and patient guidance, and continuous financial and technical support. What I learned from you not only the academic knowledge, but also working spirit, time arrangement, and more important a trust person.

I thank my committee members Dr. David Clark and Dr. Alex Aning. Thank you for your time and valuable comments.

I give great thanks to my roommates, classmates and cooperators Bo Chen and Wenle Li. I cannot use better words to express the help I benefit from you two and the happy time we spend together. It is a beautiful memory never fad. Good luck guys!

I thank Tongan Jin and Manoj Mahapatra for their good cooperation. I would like to thank ICTAS Specialist John McIntosh, Stephen McCartney for their patient training and help to the equipments. Thanks Yanxi Li for the help of AFM and Dr. Wenwei Ge for the DC power supply. Thanks Yuchang Wu, Yuan Zhou and Menghui Li for their assistance and friendship.

It is impossible to list all of my good friends at Blacksburg. I benefit a lot from their kind help.

A special thank will give to my parents for their endless love and encouragement.

Contents

List of figures:

List of tables:

Chapter 1 Introduction

1.1 Anodizaition

1.1.1 Introduction to anodization

Anodization is a traditional process to grow oxide layer on metal surface. The procedure is carried out in an electrochemical cell, including an anode (positive electrode), a counter electrode, the electrolyte in between the two electrodes and outer power source. The above four parts compose a series circuit. Usually, the power source is a DC power to keep one electrode positive potential always. Typical electrochemical cell also equipped with a third electrode called "reference electrode" to identify the applied voltage precisely.

In the anodization set up, the object metal/alloy is installed at the anode. The counter electrodes are usually Pt, carbon, or other alloys that are not reactive with the electrolyte, so the process is also called anodizing.

The electrochemcial cell set up can be used in different ways. In some occasions, metals are set as the counter electrode. They react with the electrolyte and are lost, and then go to the anode. This process is called galvanization. If no chemical reaction happens at both two electrodes, but just using the electrical field to move the charged particles/colloids in the electrolyte and adhere to the electrode, it is called electrochemical deposition.

1.1.2 Application of anodization

Anodic oxide layer is different from the thermal created oxide layer on metal, which should be treated at a high temperature, and usually at low vacuum or in some protective gas environment. Anodization can conveniently generate uniform oxide layer in large area. By adjusting the electrical field distribution, anodization can also apply to metal/alloy with versatile surface shapes, like curved surface. Besides that, the thickness of anodic oxide layer can be conveniently controlled by oxidation current and time.

Because of this advantage, anodization method has been widely chosen in the industry. The major application is to generate a condensed oxide layer on the metal/alloy surface to provide better properties than bare metal. This anodic oxide layer can increase the corrosion resistance and wear resistance. Anodization has been applied to Al, Ti, Mg, Ta, Nb, W, Hf, and Zr metal until now. Besides the pure metal, oxide layer can also be generated on the surface of Al and Ti alloys like TiAl, TiNb and TiZr, even more complex alloys like Ti_6Al_7Nb and Ti_6Al_4V.

1.1.3 Previous work on anodic film

Anodization has beem applied to several kinds of metals and metal alloys. Researchers found out that in some specific anodization conditions, novel morphologies formed on the anodic surface, like pores or tubes, instead of a condensed oxide layer. This section will focus on the anodic surface morphologies for different specimens and anodic conditions.

1.1.3.1 Anodic metal with novel morphologies

Al metal is most common used for anodization. Besides that, some other metals are also suitable for anodization and make nanostructure. Table 1 summarizes the anodization conditions and resultant morphologies for different metals in particular electrolytes and applied voltages.

Table 1 Anodization conditions and morphologies for metals

Metal	**Applied voltage**	**Electrolyte**	**Morphology**
Al	~ 25 V [1]	Sulfuric acid	Nanopores
	~ 40 V [2]	Oxalic acid	Nanopores
	~ 195 V [3]	Phosphoric acid	Nanopores
Ti	~ 20 V [4]	HF	Nanotubes
	~ 60 V [5]	Ethylene/fluoride	Nanotubes
	~ 20 V [6]	Glycerol/fluoride	Nanotubes
Ta	20 V [7]	H_2SO_4/HF	Nanopores
Nb	20 V [8]	H_2SO_4/HF	Nanopores
W	~ 40 V[9]	NaF	Nanopores
Hf	~ 50 V [10]	H_2SO_4/NaF	Nanopores
Zr	20 V [11]	$(NH_4)_2SO_4/NH_4F$	Nanotubes
Sn	~ 12 V [12]	Oxalic acid	Nanopores

Among the above metals, Al and Ti have been researched most for their versatile preparation conditions in different electrolytes. The size of Al_2O_3 nanopores is sensitive to the applied voltage. Besides that, the change of electrolyte in the component, concentration, PH, current density and temperature will also affect the final Al_2O_3 morphology.

1.1.3.2 Anodic alloys

Anodic oxide layer on the alloy surface can increase the corrosion resistance. Once again, anodizing in some specific conditions will obtain some novel surface morphology. Table 2 summarizes the anodization conditions and resultant morphologies for different alloys in particular electrolytes and applied voltages.

Table 2 Anodization conditions and morphologies for alloys

Metal	**Applied voltage**	**Electrolyte**	**Morphology**
TiAl	~ 40 V [13]	H_2SO_4/HF	Nanotubes
TiNb	20 V [14]	NaH_2PO_4/HF	Nanotubes
TiZr	20 V [15]	$(NH_4)_2SO_4/NH_4F$	Nanotubes
Ti_6Al_7Nb	20 V [16]	$(NH_4)_2SO_4/NH_4F$	Nanotubes
$Ti_{29}Nb_{13}Nb_{4.6}Zr$	~ 15 V [17]	$(NH_4)_2SO_4/NH_4F$	Nanotubes

Compared with Table 1 and Table 2, most of the anodic metals (besides Ti and Zr) will get a porous structure in specific anodization conditions. Ti and Ti alloys tend to grow nanotube structure. All the electrolytes used to generate nanotubes contain fluoride ions. Though some publications have tried to explain the phenomena of nanotube formation, the inherent mechanism why anodic Ti and Ti alloy tend to generate nanotube morphology is still unclear.

1.2 Focused ion beam

1.2.1 Introduction to focused ion beam

Focused ion beam, a technology that focuses high voltage accelerated liquid ions to bombast target area, has become one of the popular methods designing various types of nanostructures. Several kinds of liquid ions have been used as ion sources, including Al, As, Au, B, Be, Bi, Cs, Cu, Ga, Ge, Er, Fe, H, In, Li, Ni, P, Pb, Pd, Pr, Pt, Si, Sn, U and Zn [18], among which the Ga^+ is one of the most common used ion source to carry out patterning/etching/milling process. Compared to electrons, ion atoms are over 1000 times heavier, which can directly hit other atoms out. At the same accelerate voltage 30 KV, Electrical beam can only generate secondary electrons, but ion beam can "write" nano-patterns or produces nano-structures on the target materials directly. One advantage of the ion beam fabrication is its un-contact patterning without any mask. By moving the target under pre-design program, the ion beam can conveniently generate a large area of patterns, larger than 500 μm × 500 μm.

Several elements govern the ion beam effects. They are ion beam current, accelerate voltage, dwell time and pixel spacing. The ion beam current can change from 1 pA to 10 nA. Small ion beam current also means tiny ion beam spot. At 1 pA ion bean current, the focused ion spot size can be less than 5 nm. Accelerate voltage controls the ion etching or implantation depth. Dwell time, pixel spacing, pass number, and ion dose are all equipment parameters. Dwell time defines how long the ion beam spot stops at one point in each pass. Pixel spacing is the distance between two ion beam hit centers. Pass number indicates how many times the ion beam goes through the whole pattern. Ion dose is the total amount of the ions that hit the target materials. It is determined by ion current, dwell time, and pass number. Ion dose per pixel/spot is one important parameter that quantifies the ion beam effect.

Figure 1-1 shows a real FIB equipment. Figure 1-1 (a) is a picture of the Helios NanoLab 600 dual beam FIB. “Dual beam” means not only ion beam, but electron beam is equipped inside. The e-beam can conduct Pt deposition, at the same time act as a SEM. Those two guns in Figure 1-1 (b), ion beam gun (Ⅰ) and e-beam gun (Ⅱ) have an angle of 52°. When ion beam is milling on the target material, image can be taken by e-beam at an angle of 52°. In this case, dual beam FIB could supervise in-situ growth.

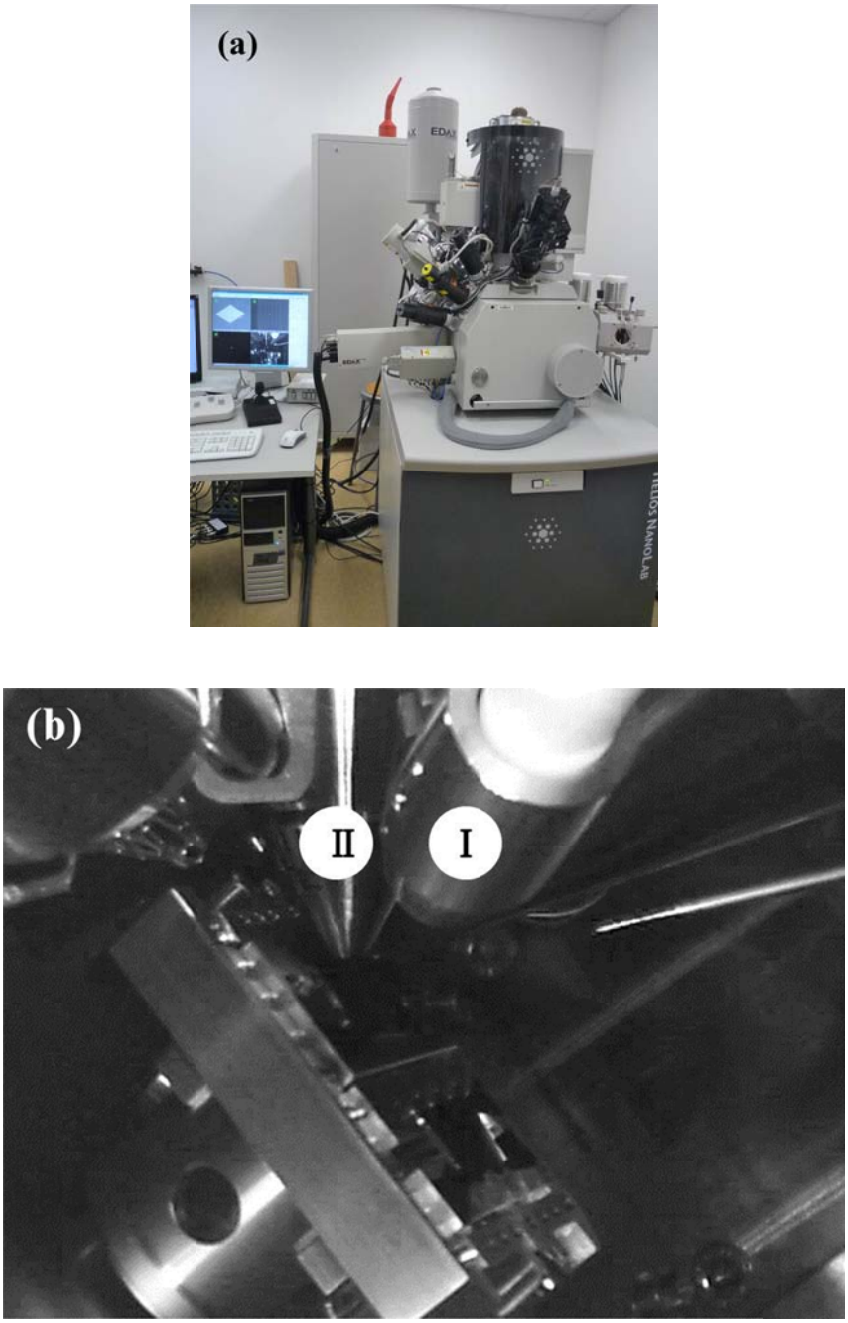

Figure 1-1 Images of FEI Helios NanoLab 600 Dual Beam FIB. (a) FIB facility; (b) The e-beam gun and ion beam gun equipped in FIB.

1.2.2 Reaction between ion beam and materials

The reaction between ion beam and the solid materials can be classified by the nature of the interactions.

Milling is understood as the elastic collision of physical sputtering when the ion bombardment on the target materials happens. Sputtering occurs due to a series of elastic collision when the incident ions transfer momentum to the target materials in the collision region. If the solid atoms receive enough kinetic energy that beyond the surface binding energy, they will eject as sputtered atoms out of the surface. In general situation, the sputtered atoms will deposit onto the substrate again, which is called redeposition. Redeposition is one of the reasons that cause the milling patterns to become "V" shaped or reverse pyramid in depth direction.

Inelastic interaction between incident ions and target atoms during the ion bombardment will generate phonons, plasmons (in metal) and secondary electrons. Here secondary electrons are what we commonly use to take images. Besides secondary electrons, secondary ions will also generate in the ion beam bombardment region. Images taken by the secondary ions provide different types of information, compared to the secondary electron imaging. Ion beam can only penetrate very shallow depth. Take 30 KV accelerated Ga^{+} ions for example, the penetration depth limited to tens of nanometers, therefore the secondary ion beam image directly reflect the surface information within the ion beam collision area.

1.2.3 Nano-fabrication under focused ion beam

Direct writing is one of the FIB nanofabrication technologies. It focuses the ion beam directly onto the substrate and creates pattern. The ion beam spot size determines the resolution. There are many reports on making nano-scale pores, lines and layered structures.

Since the focused ion beam stream has a Gauss distribution, the pores are not column like, but reverse pyramid liked structure, or so-called V shape. In this case, FIB cannot make high aspect ratio nano-pores. Typically, under 30 KV accelerate voltage, the aspect ratio of the pore length and diameter will not exceed five [19]. Lee et al [20], investigated the FIB patterned nano-pore shape under AFM. The FIB patterned pore diameter is less than 20 nm. They also reported rings appear on the edge of each FIB drilled pores. These rings are higher than the substrate. It is the redeposition of target materials and the swelling due to the amorphization effect. Researches have filled in the FIB patterned pores on the GaAs substrate with In metal, making use of this pyramid liked probe as the atomic force microscope tip [21].

FIB direct writing contains two kinds of operations. One approach is using a very strong ion dose to remove atoms from the target, which is called etching or milling. Another approach is to deposit other atoms on the target, which is called ion beam induced deposition. This process can deposit useful materials on almost any chosen target in nano-scale precision. For a practical example in this thesis, we pumped in methylcyclopentadienyl platinum trimethyl precursor gas using a tiny tube very near the bombardment area. The Pt organic precursor gas was split by high energy ion beam, leaving Pt metal on the target surface. This Pt layer can provide good conductivity to

prevent charging, at the same time, protects the surface. If the area is not hit by ion beam, not such deposition will happen. In this case, ion beam induced deposition is also a kind of method to build nano-structure on the surface.

1.3 Objective: ion beam guided anodization

For general anodic nanopores/nanotubes, their arrangement is random. In other words, the only advantage we make use of is large surface area, which is enough for many applications. However, in some occasions we need to avoid local effect, like nanostructured capacitor, or want to control the location precisely, such as hard disk storage, ordered structure is necessary.

Much effort has been provided to generate well-arranged nanopore arrays using guiding effect, like nano-imprint [22] and lithography [23]. The reports on ordered porous structure mostly concentrate on anodic alumina. Some phenomena have been observed for the ordered anodic alumina, such as light propagates through 2D photonic crystal [24].

In this study, the FIB patterning function and the anodization process are combined together, making highly ordered nanopore/nanotube arrays. Besides that, the nanoporous structure is expected to be controllable.

1.4 References

1. Masuda, H., F. Hasegwa, and S. Ono, Self-ordering of cell arrangement of anodic porous alumina formed in sulfuric acid solution. *Journal of the Electrochemical Society*, 1997. **144**(5) p. L127-L130.
2. Li, F.Y., L. Zhang, and R.M. Metzger, On the growth of highly ordered pores in anodized aluminum oxide. *Chemistry of Materials*, 1998. **10**(9) p. 2470-2480.
3. Masuda, H., K. Yada, and A. Osaka, Self-ordering of cell configuration of anodic porous alumina with large-size pores in phosphoric acid solution. *Japanese Journal of Applied Physics Part 2-Letters*, 1998. **37**(11A) p. L1340-L1342.
4. Gong, D., C.A. Grimes, O.K. Varghese, W.C. Hu, R.S. Singh, Z. Chen, and E.C. Dickey, Titanium oxide nanotube arrays prepared by anodic oxidation. *Journal of Materials Research*, 2001. **16**(12) p. 3331-3334.
5. Wang, J. and Z.Q. Lin, Freestanding TiO2 nanotube arrays with ultrahigh aspect ratio via electrochemical anodization. *Chemistry of Materials*, 2008. **20**(4) p. 1257-1261.
6. Macak, J.M., H. Tsuchiya, L. Taveira, S. Aldabergerova, and P. Schmuki, Smooth anodic TiO2 nanotubes. *Angewandte Chemie-International Edition*, 2005. **44**(45) p. 7463-7465.
7. Sieber, I., B. Kannan, and P. Schmuki, Self-assembled porous tantalum oxide prepared in H2SO4/HF electrolytes. *Electrochemical and Solid State Letters*, 2005. **8**(3) p. J10-J12.

8. Sieber, I., H. Hildebrand, A. Friedrich, and P. Schmuki, Formation of self-organized niobium porous oxide on niobium. *Electrochemistry Communications*, 2005. **7**(1) p. 97-100.

9. Tsuchiya, H., J.M. Macak, I. Sieber, L. Taveira, A. Ghicov, K. Sirotna, and P. Schmuki, Self-organized porous WO3 formed in NaF electrolytes. *Electrochemistry Communications*, 2005. **7**(3) p. 295-298.

10. Tsuchiya, H. and P. Schmuki, Self-organized high aspect ratio porous hafnium oxide prepared by electrochemical anodization. *Electrochemistry Communications*, 2005. **7**(1) p. 49-52.

11. Tsuchiya, H., J.M. Macak, L. Taveira, and P. Schmuki, Fabrication and characterization of smooth high aspect ratio zirconia nanotubes. *Chemical Physics Letters*, 2005. **410**(4-6) p. 188-191.

12. Shin, H.C., J. Dong, and M.L. Liu, Porous tin oxides prepared using an anodic oxidation process. *Advanced Materials*, 2004. **16**(3) p. 237-240.

13. Berger, S., H. Tsuchiya, and P. Schmuki, Transition from Nanopores to Nanotubes: Self-Ordered Anodic Oxide Structures on Titanium−Aluminides. *Chemistry of Materials*, 2008. **20**(10) p. 3245-3247.

14. Ghicov, A., S. Aldabergenova, H. Tsuchyia, and P. Schmuki, TiO2-Nb2O5 nanotubes with electrochemically tunable morphologies. *Angewandte Chemie-International Edition*, 2006. **45**(42) p. 6993-6996.

15. Yasuda, K. and P. Schmuki, Electrochemical formation of self-organized zirconium titanate nanotube multilayers. *Electrochemistry Communications*, 2007. **9**(4) p. 615-619.

16. Macak, J.M., H. Tsuchiya, L. Taveira, A. Ghicov, and P. Schmuki, Self-organized nanotubular oxide layers on Ti-6Al-7Nb and Ti-6Al-4V formed by anodization in NH4F solutions. *Journal of Biomedical Materials Research Part A*, 2005. **75A**(4) p. 928-933.

17. Tsuchiya, H., J.M. Macak, A. Ghicov, Y.C. Tang, S. Fujimoto, M. Niinomi, T. Noda, and P. Schmuki, Nanotube oxide coating on Ti-29Nb-13Ta-4.6Zr alloy prepared by self-organizing anodization. *Electrochimica Acta*, 2006. **52**(1) p. 94-101.

18. Tseng, A.A., Recent developments in micromilling using focused ion beam technology. *Journal of Micromechanics and Microengineering*, 2004. **14**(4) p. R15-R34.

19. Tseng, A.A., Recent developments in nanofabrication using focused ion beams. *Small*, 2005. **1**(10) p. 924-939.

20. Li, H.W., D.J. Kang, M.G. Blamire, and W.T.S. Huck, Focused ion beam fabrication of silicon print masters. *Nanotechnology*, 2003. **14**(2) p. 220-223.

21. Ohkouchi, S., Y. Nakamura, H. Nakamura, and K. Asakawa, Indium nano-dot arrays formed by field-induced deposition with a Nano-Jet Probe for site-controlled InAs/GaAs quantum dots. *Thin Solid Films*, 2004. **464-65** p. 233-236.

22. Yasui, K., T. Morikawa, K. Nishio, and H. Masuda, Patterned magnetic recording media using anodic porous alumina with single domain hole configurations of 63 nm hole interval. *Japanese Journal of Applied Physics Part 2-Letters & Express Letters*, 2005. **44**(12-15) p. L469-L471.

23. Sun, Z.J. and H.K. Kim, Growth of ordered, single-domain, alumina nanopore arrays with holographically patterned aluminum films. *Applied Physics Letters*, 2002. **81**(18) p. 3458-3460.

24. Yanagishita, T., K. Nishio, and H. Masuda, Two-dimensional photonic crystal composed of ordered polymer nanopillar arrays with high aspect ratios using anodic porous alumina templates. *Applied Physics Express*, 2008. **1**(1) p. 012002.

Chapter 2 Ion beam guided anodic aluminum oxide

2.1 Introduction to porous anodic aluminum oxide

Anodic aluminum oxide (AAO) is originally applied to passivate and to protect Al from corrosion and abrasion. However, under some specific anodization conditions, like anodizing in specific acids with a certain range of applied voltage, nano-scaled porous structure is obtained, instead of a condensed oxide layer. This large area structured surface leads AAO to many applications as catalysis supports or as templates. Researchers have developed many ways to control the AAO morphology, pore diameter, porosity, and length by varying the growing environments. Porous AAO is popular chosen as template to make nano-pillars.

2.1.1 Porous anodic aluminum oxide under different electrolytes

Selecting the electrolyte is the first step when doing anodization. It has been found that porous AAO can be formed in sulfuric acid, oxalic acid, phosphoric acid, and some mixed acid solutions only in narrow anodization reaction windows, which means in different electrolytes the optimized applied voltage or current density are different.

2.1.1.1 Porous anodic aluminum oxide under sulfuric acid

Anodization under sulfuric acid needs the smallest applied voltage (~ 25 V) to generate relative good arranged pore arrays.[1, 2] Among all the electrolytes, AAO generated in the sulfuric acid has the largest porosity due to its smallest interpore distance

and thin pore walls. At ~25 V, the interpore distance is ~ 65 nm. In previous work, researchers have varied the applied voltage around 25 V (from 20 V to 27 V) to investigate the best self-organized pore arrangement [3]. They found that for sulfuric acid, the pore arrangement was very sensitive to the applied voltage; even small change can clearly affect the anodized pore arrays. The stable anodization in sulfuric acid is usually difficult to maintain when the applied voltage goes beyond 27 V because of an occurrence of breakdown or "burning" effect [4]. When "burning" effect starts, the current density tremendously increases and the total anodic template is destroyed in the electrolyte under a high electric field. To solve the problem, constant current method was carried out, which confines the largest current density to avoid "burning" [5, 6].

2.1.1.2 Porous anodic aluminum oxide under oxalic acid

A relative ordered AAO porous structure is obtained in the oxalic acid electrolyte at ~ 40 V applied voltage. The interpore distance of AAO is approximately 100 nm at this given voltage. Different from such narrow anodization window in the sulfuric acid electrolyte, the applied voltage can vary from 30 V to 80 V for oxalic acid.[7-9] In this case, the interpore distance has a range of 70 - 140 nm. In this voltage range, better arranged pores, though not perfect periodic porous structure can be created, compared to other applied voltage. However, the electrolyte concentration should be slightly changed according to the applied voltage. Zhao et al [10], have discussed anodization conditions in the oxalic acid and the correlated results; the oxalic acid concentration is 0.3 M for 30 V, 0.4 M for 40 V, and 0.5 M for 50 V. If anodizing Al foil in 0.5 M oxalic acid at 60 V, the surface will burn and finally get Al_2O_3 nanowires. When oxidizing in the oxalic acid,

very large aspect ratio pores was obtained. In Masuda et al's work, the aspect ratio was over 150 and a pore density of 10^{10} cm^{-2} was obtained [9].

2.1.1.3 Porous anodic aluminum oxide under phosphoric acid

Anodization in the phosphoric acid electrolyte is also commonly chosen for AAO fabrication. The applied voltage is the largest in phosphoric acid within all of the electrolytes. The applied voltage range that has been used is from 120V to 195 V.[11, 12] In this voltage range, the interpore distance varies from 300 nm to 500 nm. It exhibits that preparing AAO in the phosphoric acid can best tolerate the applied voltage change. The reason why this can happen has not been clearly understood. However, some research work has made use of the voltage tolerance and created novel structure. Lee et al, used a big/small alternated anodization voltage to modulated the nanopore morphology and successfully obtained a bamboo liked AAO pores [13]. Too large current density needs to be avoid when anodizing Al foil in the phosphoric acid [14], which sometimes results in local destroy, or "burning" [15]. The "burning" effect is similar to which was reported for the sulfuric acid. In this case, constant current anodization is chosen to avoid "burning" [16].

2.1.1.4 Porous anodic aluminum oxide under mixed acids

Instead of anodizing in the above three traditional electrolytes, researchers also tried to do anodization in a multiple acids mixture electrolyte or multiple electrolytes. Some novel porous AAO structures have been reported. Rauf et al [17], got a layered

structure by anodizing Al foil successively in the sulfuric acid and oxalic acid. An interface appears clearly when changing the electrolyte. The connection between the two electrolytes and the initial of the second layer were discussed. Electrolytes composed of sulfuric acid/oxalic acid mixture have also been investigated.[18, 19] However, the use of mixed acids electrolytes is not popular. One reason to choose this kind of mixture is to cover the anodization voltage range which is not suitable for any single acid. In Shingubara et al's work [18], they use a 32 V applied voltage, which is higher than optimized voltage in the single sulfuric acid but lower than that in the single oxalic acid.

2.1.2 Application of anodic aluminum oxide template

AAO template has been widely used as the catalyst support, largely due to its relatively stable nature, and a great range of large surface area and porosities, which are a benefit to many catalytic applications.

With a melting point as high as 2072 °C, AAO shows relative stability at a very high temperature when working as a catalytic substrate. To fully understand the possibility of working at a high temperature, Lippens et al. [20], studied the phase transform of Al_2O_3 from room temperature to very high temperature, started from boehmite and pseudo-beohmite. Starting from boehmite, it will transform to γ-Al_2O_3 at 450 °C, then δ-Al_2O_3 at 600 °C, (θ+α)-Al_2O_3 at 1050 °C, α-Al_2O_3 at 1200 °C. Started from pseudo-boehmite, the first phase transform starts at 300 °C to γ-Al_2O_3, then δ-Al_2O_3 at 900 °C, (θ+α)-Al_2O_3 at 1000 °C, α-Al_2O_3 at 1200 °C. Other work also reported the change of surface area and the porosity of Al_2O_3 with the temperature [21]. Those

researches provided basic experimental results supporting the application of Al_2O_3 in the area of catalysis. One example is to use alumina supported metal as the catalysts in the thermal reforming of methane [22]. the working temperature is as high as 1000 °C.

Benefit from the development of nano-scaled template fabrication, some well-arranged AAO has been used as 2D photonic crystals.[23, 24] In these works, other materials, especially metals or those with specific refractive indexes were filled inside the AAO pores. After melting the AAO, the rest of nano-pillar arrays can be studied as the 2D photonic crystals. However, these nano-pillar arrays were not perfectly periodic structures due to the non-perfect AAO pore arrangement, as well as non-perfect filling into the nanopores. The 2D photonic crystal does not have a sharp tip reflection spectrum but expands to ~ 100 nm [25]. However, the well-ordered AAO has presented its potential application to the photonic crystal. For other applications in the optics area, one interesting application is to fill polymers in the AAO pores. AAO molded polymer arrays can optimize its surface antireflection property.[26-29]

2.2 Guided anodization

Guided anodization is to make shallow holes on the metal surface before anodization. In the anodization process, the guided holes trend to react fast with the electrolyte and develop quickly, so that the deeper anodic pores can grow following the guiding patterns. However, materials have their intrinsic characteristics in nature. Not all the anodic pores will generate according to the guiding pattern. The guiding function has a limited effective range which has to match the material's inherent nature. One example

is to create shallow stripes, concaves, or both kinds of features on the Al surface from different electropolishing conditions before the anodization.[30] These shallow surface features are generally on the scale of several nanometers. However, they have not been proven effective in guiding pore development.[31]

2.2.1 Nano-indentation and nano-imprint guided anodization

Two major methods to make ordered pores are nano-indentation and nano-imprint. Both of them are contact patterning methods. Nano-indentation is to indent shallow holes on the Al foil surface using AFM probe.[32, 33] For this method, the indenter tip greatly influences the pore shape and depth. Load variation and tip wear/deformation create different pore sizes. Often times, only triangle pores can be produced. Mold nano-imprint is another popular method to make guiding holes on the Al foil using SiC[9, 34] and Si_3N_4[35, 36] molds. Figure 2-1 is a sketch of nano-imprint guided anodization [7]. Typically, the molds need to have enough mechanical strength for imprinting, high quality surface smoothness, and sufficient resolution. In Asoh et al's work [7], single crystal SiC warfare was used as the mold substrate. After e-beam etching/lithography, nano-scale round convex array was made on the mode. The mold will imprint concave array on Al surface as the guiding pattern. For the mold nano-imprint method, any misalignment between the mold and the substrate can cause local pressure variation and thus inhomogeneous pores or even defects. Due to the resolution, it is difficult to indent the pattern with an interpore distance less than 50 nm using the mold nano-imprint.

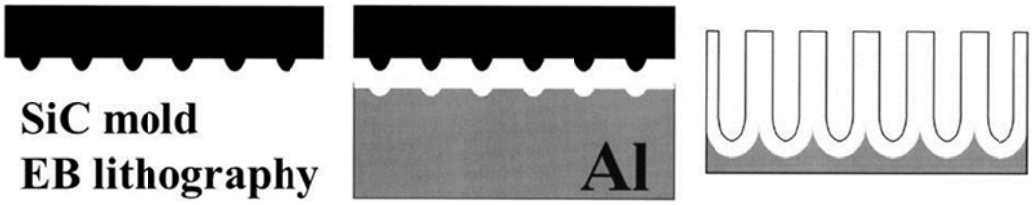

Figure 2-1 Sketch of the Nano-imprint guided anodization.

2.2.2 Holographic lithography and focused ion beam guided anodization

To avoid the pore variation and defects generated in the contact mode pre-patterning, holographic lithography [37] and FIB milling [38-40] have been introduced to create patterns on the Al surface. Both of them can make guiding patterns without touching the sample surface. The holographic lithography is one kind of photolithography. Grating with specific period needs to prepare first. This method can pattern large areas but the resolution is restricted by the light wavelength and the grating precision. The pore size and the interpore distance are fixed depending on the grating. In contrast, the FIB lithography has a much better resolution. Figure 2-2 sketches the process of FIB guided anodization. First, some specific guiding patterns are created by ion milling on the Al surface. Then after the andization, these patterns can fully develop inside the substrate due to the guiding effect. The ion beam spot size can be adjusted to less than 10 nm, and the patterning is fast and has no need of any mask [41]. Sophisticated channel patterns have been created using the FIB lithography by purposely closing or opening the pores pre-created by the anodization [42, 43]. However, the FIB pattern guided anodization is not well understood, and its potential in creating complicated pore patterns needs to be explored.

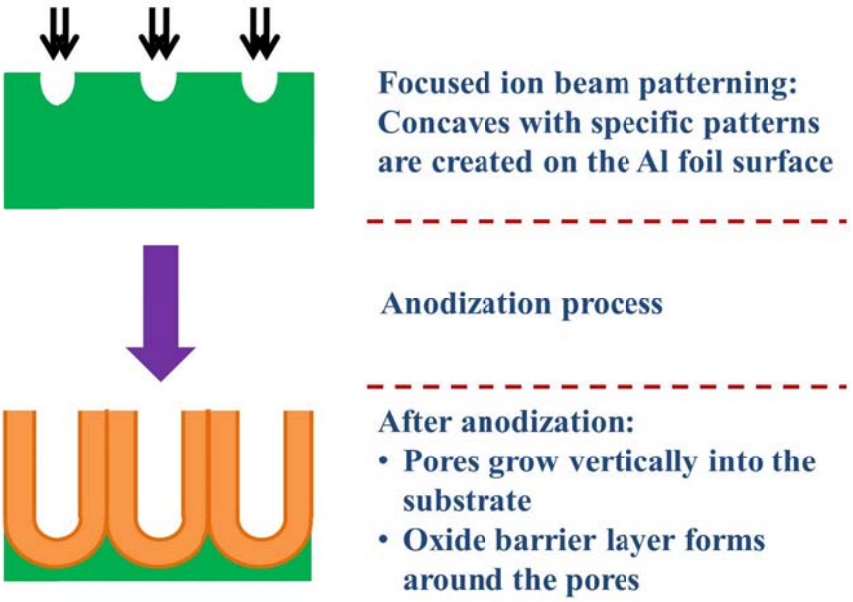

Figure 2-2 Sketch on FIB guided anodization process.

2.3 Experimental section

2.3.1 Anodization set up

The anodization was carried out in an electrochemical cell. Figure 2-3 shows the electrochemical cell and the DC power source for anodization. Target metal piece is clamped at anode (Ⅰ) and the Pt mesh is fixed at the counter electrode (Ⅱ). DC power (Ⅲ) can provide constant voltage (≤ 300 V) and constant current (≤ 400 mA) modes. Stir machine (Ⅳ) provides a vigorous stirring if necessary.

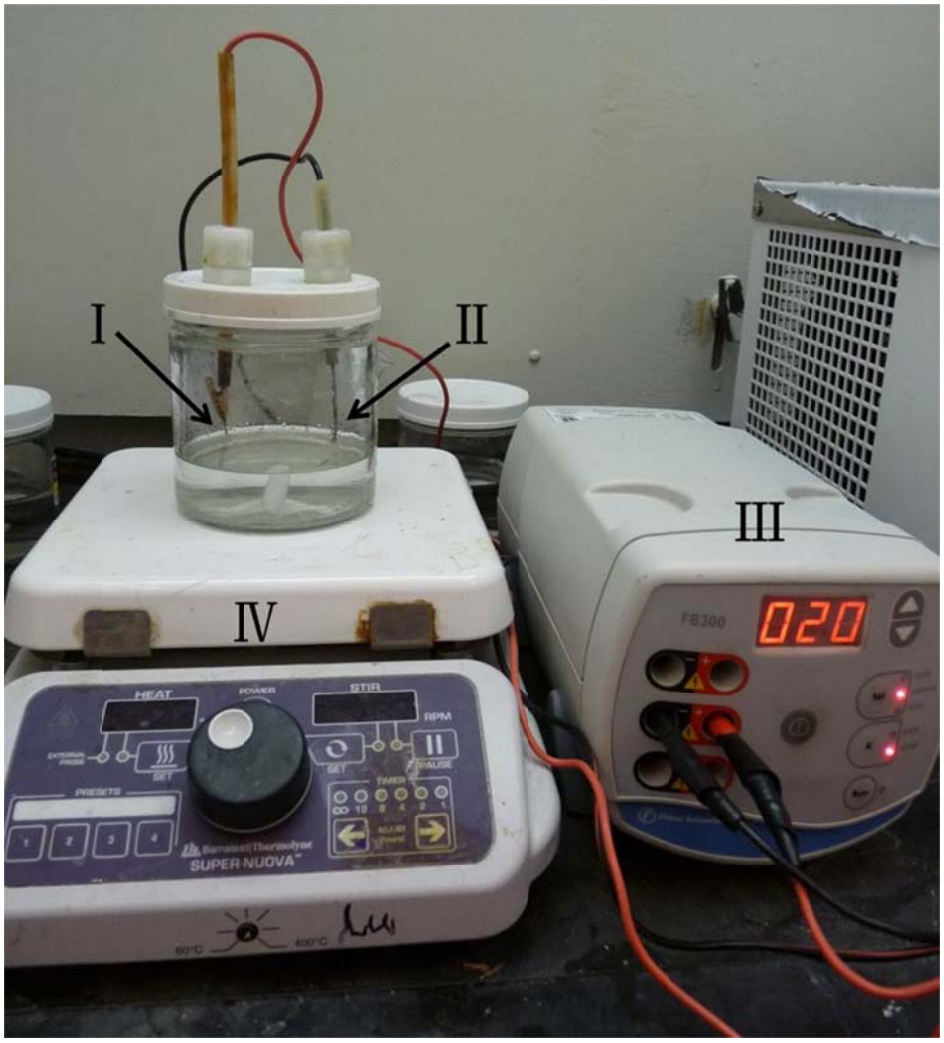

Figure 2-3 Electrochemical cell and DC power source.

Figure 2-4 is a constant temperature tank keeping the electrolyte at the target temperature. During the anodization, the electrical cell was immersed into the liquid medium inside the tank, in which way to keep the target temperature. Ethenal/water mixture is used as the liquid medium.

Figure 2-4 Constant temperature tank.

2.3.2 Al foil polishing

High purity aluminum foils (99.999%, Goodfellow Corporation, Oakdale, PA) with 0.3 mm thickness were cut to 1.0 cm × 2.2 cm size. They were then thermal treated in a high purity argon atmosphere at 773 K for 2 hours to release the stress and increase the grain size. After that, the aluminum foils were cleaned by ethanol and acetone, and then treated in a 0.5 wt% NaOH solution for 10 minutes to chemically etch out the Al_2O_3 layer on the Al surface.

To get a smooth surface, two polishing methods have been tried, mechanical polishing and electropolishing. In the mechanical polishing process, Al foil was first polished by 360 grit SiC polishing paper until the surface is uniform, and then switched

to 1200 grit SiC polishing paper. After that the sample was polished successively by 5 μm, 1 μm, 0.1 μm, and 0.03 μm Al_2O_3 aqueous suspensions until mirror reflection.

Electropolishing is carried out in an electrochemical cell the same as anodization. The NaOH treated Al foils were electropolished in a mixture of perchloric acid and ethanol (volume ratio 4:1) for 6-8 minutes at a constant voltage of 12 V to obtain a mirror reflect surface. The polished samples were kept in ethanol or acetone for further use.

2.3.3 Focused ion beam condition

A FIB microscope (Helios NanoLab 600 Dual Beam, FEI Company, Hillsboro, OR) was employed to pre-pattern the Al surface before the anodization. The applied voltage was 30 KeV. The ion current was 9.7 pA. The ion beam scanned the pattern surface multiple times for each pore array. The beam dwell time at a specific location per scan was $3\,\mu s$. The total number of scans was set by trial and error based on the pattern quality. The FIB patterns and pore sizes were designed by the software Serif DrawPlus 7 (Serif, Nottingham, UK) using vector-enabled pixel images. Each pixel in the pore pattern designs was scaled to 1 nm in the actual FIB created patterns. There were only two contrasts in the pattern designs. In Figure 2-5, the high contrast (white) part of the pixel images was designed to be removed and the low contrast (dark) part of the pixel images was designed to be retained. Hexagonal and square pore patterns were created by the FIB lithography. The interpore distances were 250-800 nm. This FIB patterning approach had the advantage of reproducing any designed pore patterns but the image file size could be extremely large, especially if a large pattern area was involved. It also took a long time to create the pore patterns. In consideration of this, another method was used

for large area FIB patterning. In the latter approach, a hexagonal pattern from the FIB microscope software package was used. The ion beam was controlled to create one pore in one scan only until the entire array was completed. This enabled the creation of large surface area hexagonal patterns (such as 30 μm × 30 μm size) in a short time. The pore size and depth were carefully controlled as discussed.

Figure 2-5 is a typical example of the as-imported bmp format image. After FIB etching according to this image, nanopores array pattern will appear on the sample surface since the white spot will be explore under the ion beam and design to be removed. We can easily control the desired pore size and interpore distance by change the image design. It provides an easy and applicable way to research the guiding effects on the AAO template growth.

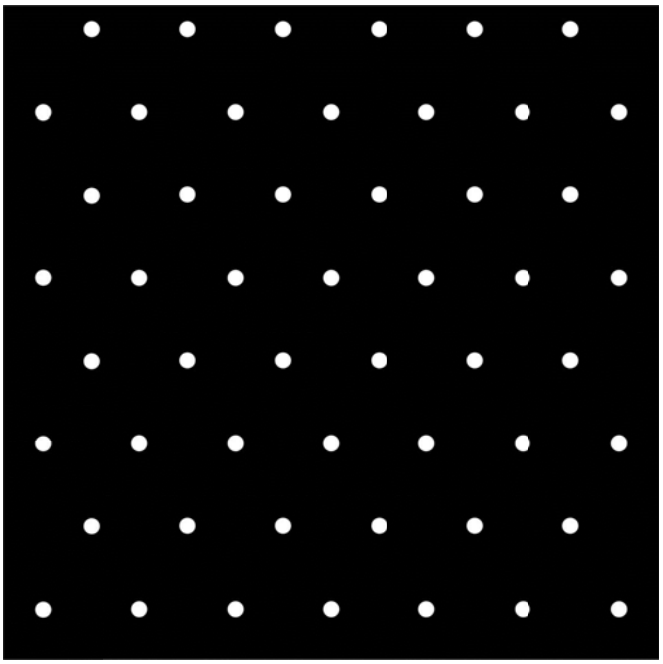

Figure 2-5 Hexagonal pattern design for FIB milling.

2.3.4 Anodization condition

The anodization was process at 0 °C in a 0.3 M phosphoric acid electrolyte via a constant current method for 6 minutes. The current density was 20 mA/cm^2. After the anodization, pore widening was carried out in 5 wt% phosphoric acid at room temperature for 30 minutes.

2.4 Results and discussion

2.4.1 Surface morphology

2.4.1.1 Polishing effect

Figures 2-6 are SEM images of the Al foil surface before and after polishing. The as-received sample (Figure 2-6(a)) presents a rough surface. Figure 2-6(b) shows the mechanically polished and then electropolished sample. Random dark spots caused by mechanical polishing cannot remove which prevents mechanical polishing from further study.

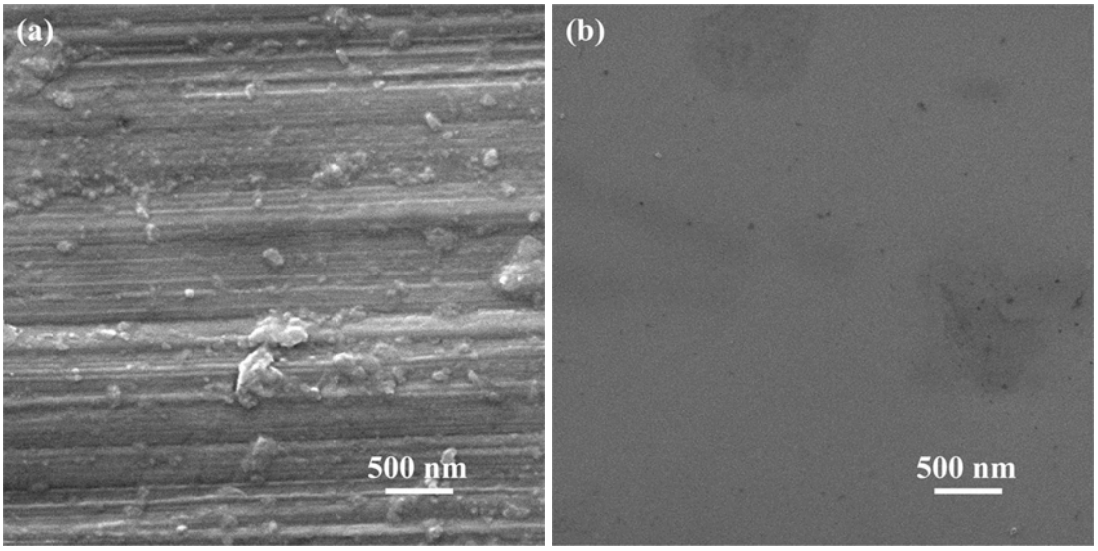

Figure 2-6 Different polishing effect on the Al foil. (a) As received sample; (b) mechanically polished and then electropolished sample.

Electropolishing is also common used to make the surface roughness in nano-scale. Figure 2-7 shows SEM image of the electropolished surface. There are some very shallow stracks on the surface induced by electropolishing. A similar phenomenon was reported before.[30] Electropolishing can create shallow stripes, concaves, or both kinds of features on the Al surface depending on electropolishing conditions. These shallow surface features are generally on the scale of several nanometers. However, they were not effective in guiding pore development.[31]

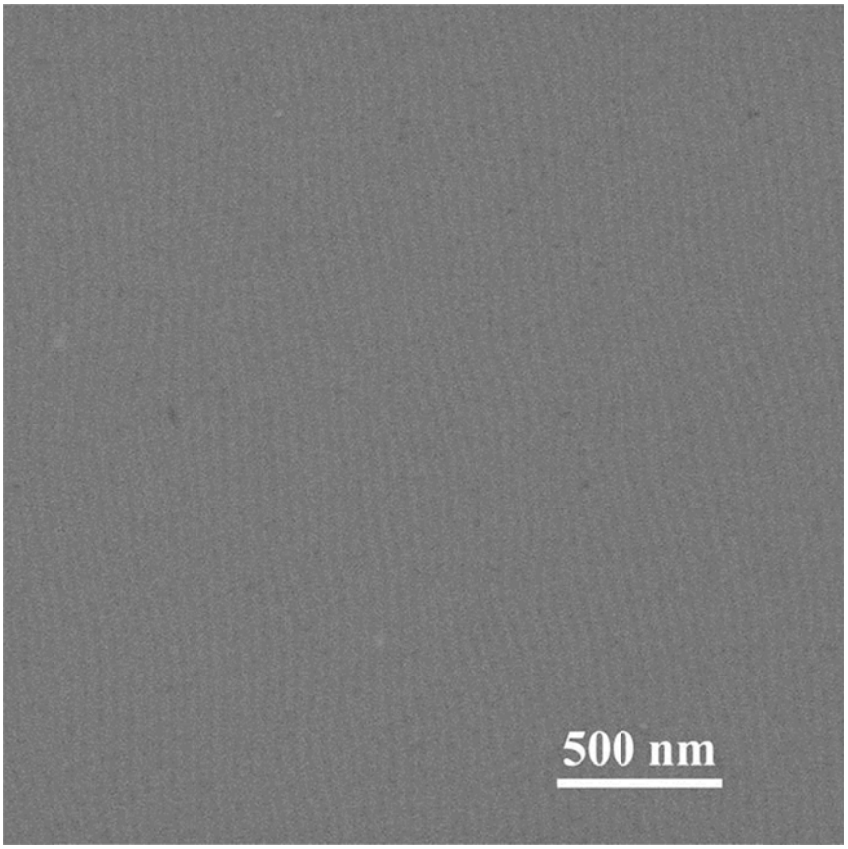

Figure 2-7 Electropolished Al foil.

Figure 2-8 shows AFM image of the electropolished Al surface with an area of 1 μm × 1 μm. The measurement indicates that the surface roughness is less than 1 nm [44]. Based on our recent work, the main function of the electropolishing is to provide a smooth Al surface for the subsequent anodization process [45, 46]. The smoothness desirably offers the surface condition to study the FIB patterning effect on pore pattern formation by the anodization.

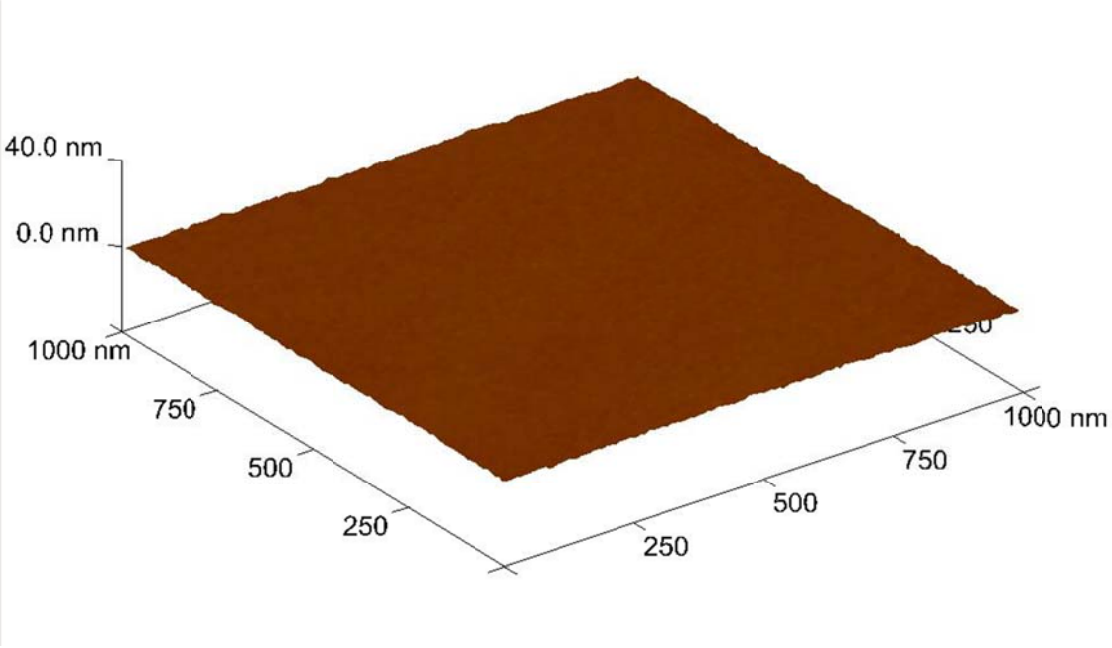

Figure 2-8 AFM measurement for electropolished Al foil.

2.4.1.2 FIB guiding patterns

Hexagonal and square patterns were created by FIB. Figure shows the SEM images of the hexagonally arranged FIB pore patterns before the anodization. The pore size is designed and also measured to be 50 nm for all the patterns. The interpore distances are designed and measured to be 250 nm, 350 nm, and 500 nm for Figures 2-9 (a) to (c), respectively. The pattern arrays are designed and measured to be 3 μm × 3 μm in size. The pore size, shape, and arrangements are very consistent. The pore shape is slightly elongated in the vertical direction, a result of elongated ion beam shape for this specific study. Around each pore, there is a white ring layer of ~ 25 nm thick, which indicates the Al surface change during the FIB milling. It is a result of Al amorphization and the implantation of the high atomic number Ga^+ [47]. In our work [44], line scan

images from atomic force microscopy across the patterns have been carried out. It shows very consistent pore size, shape, depth, and periodicity.

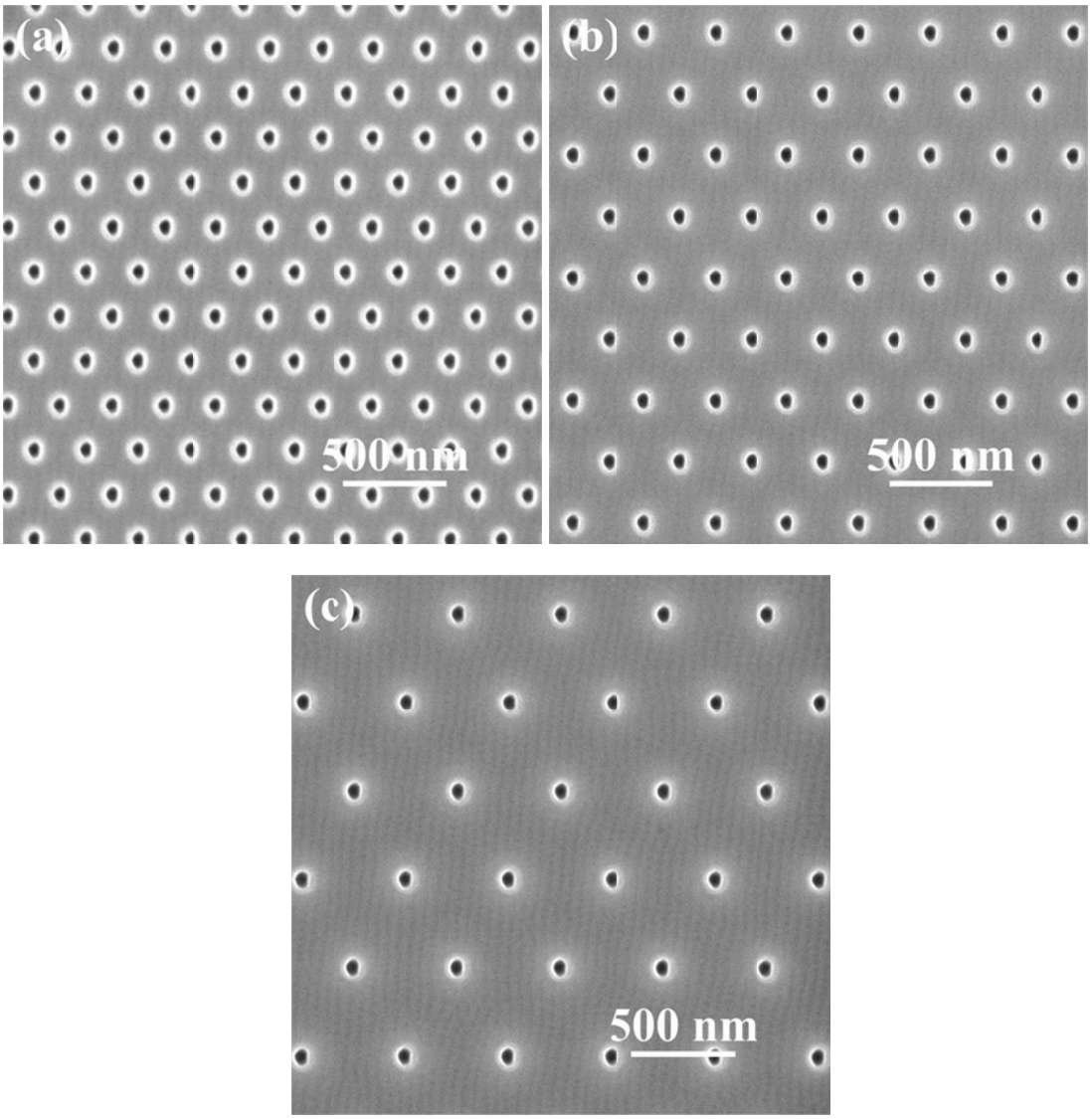

Figure 2-9 Images of hexagonal pore patterns created by the FIB patterning before the anodization. The pore size is 50 nm. The interpore distances are 250 nm (a), 350 nm (b), and 500 nm (c).

Figure 2-10 shows the SEM images of the FIB pore patterns in a square arrangement before the anodization. The reason to make square pattern is because general anodization can only create hexagonal arrangement in nature. It is very interesting to reveal whether or not guiding force can overcome the self-organization effect. The FIB milling pattern size is designed and measured the same as those from the hexagonal patterns in Figures 2-10 (a) to (c). The pore shape is also slightly elongated in the vertical direction. The white rings are also apparent around the pores. This demonstrates the repeatability of the FIB patterning process. The causes are the same as explained before.

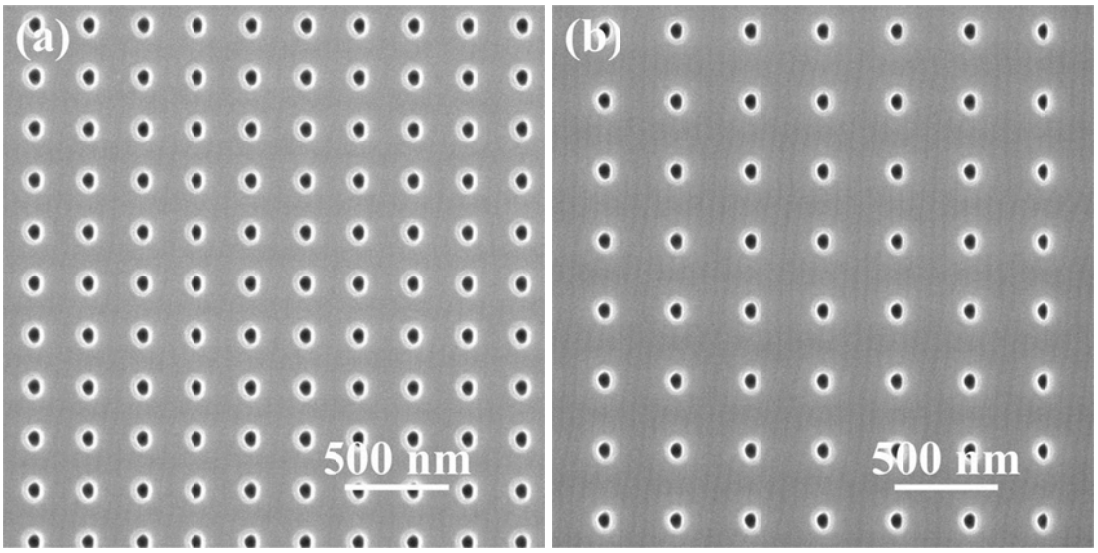

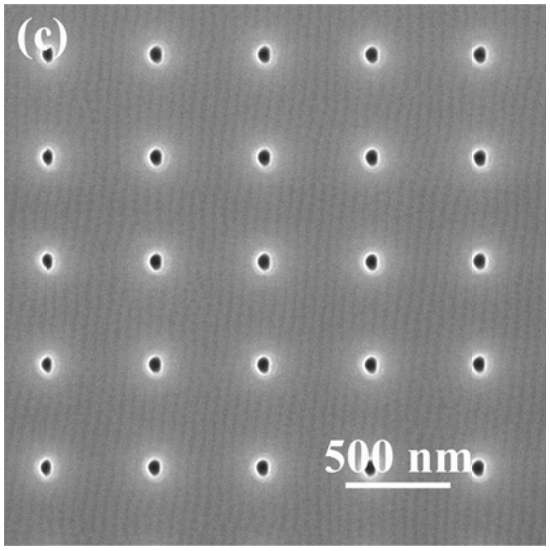

Figure 2-10 Images of square pore patterns created by the FIB patterning before the anodization. The pore size is 50 nm. The interpore distances are 250 nm (a), 350 nm (b), and 500 nm (c).

To understand the influence of the FIB patterned pore arrangement and the interpore distance on further pore development during the anodization, all the pores created by the FIB process should have very similar diameter and depth. This requirement depends not only on the design of the patterns but also on the FIB voltage and the Ga^+ ion beam dose applied at each pore. In this study, the FIB voltage is controlled the same at 30 KeV for all the experiments; the ion dose is controlled by the ion beam current (9.7 pA) and the beam exposure time. Since the patterns in Figures 2-9 and 2-10 have different interpore distances and pore arrangements, the total FIB exposure time varies but each pore has the same ion exposure. The total FIB exposure time is 35 s, 21 s, and 10.4 s for Figures 2-9 (a) to (c) respectively and 33.8 s, 20 s, and 5 s for Figures 2-10(a) to (c), respectively. For each pore, the ion beam exposure time is ~110 ms.

2.4.1.3 Nanopore arrays after anodization

Figure 2-11 shows the SEM images of the FIB patterns after the anodization. Figures 2-11 (a) - (c) are the anodized results of Figure 2-9 (a) - (c), respectively. After the anodization, the pore size increases from 50 nm to ~110 nm for all the patterns. The hexagonal patterns are maintained and the interpore distance remains the same at 250 nm, 350 nm, and 500 nm respectively. The pores are more spherical. The white rings around the pores largely disappear for all the images. This means the FIB patterned pores mainly serve as the guiding sites for further pore growth. The anodization has effectively removed the amorphorized and Ga+ implanted Al layer around the pores.

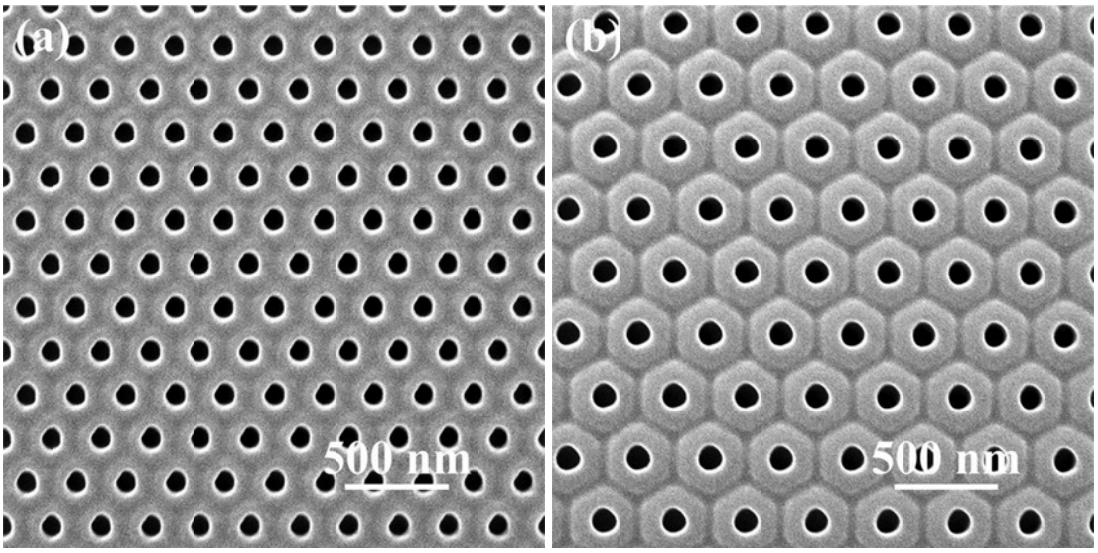

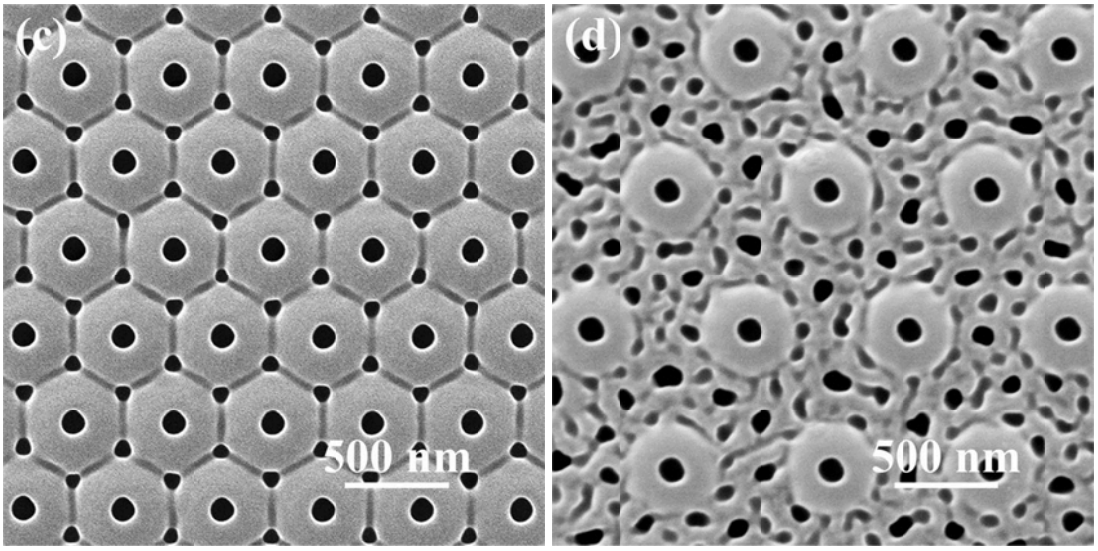

Figure 2-11 Images of the hexagonal FIB patterns after the anodization. The interpore distances are 250 nm (a), 350 nm (b), 500 nm (c), and 800 nm (d).

For the 250 nm interpore distance pattern, the Al matrix is homogeneous; no visible pattern is observed around the pores (Figure 2-11(a)). When the interpore distance increases to 350 nm, a hexagonally shaped cell forms around each pore and these cells connect into a hexagonal mosaic for the FIB patterned area (Figure 2-11(b)). When the interpore distance increases to 500 nm (Figure 2-11(c)), the hexagonal mosaic becomes more visible. More interestingly, uniform-sized and well-arranged small pores appear at the tri-junctions of the cells from the initial hexagonal pore pattern. The small pore size is 70 nm. In combination, a set of large pores with hexagonal arrangement is ideally meshed with a set of small pores arranged at the six corners of a hexagonal mosaic after the anodizaion. The hexagonal mosaic formation is the pre-requisite and serves as the guide for the small pore pattern formation. In our study, it has been identified that the interpore distance of the FIB patterned pores must fall within a specific range for the hexagonal

mosaic and subsequently small pore pattern to form. For the hexagonal pore pattern from the FIB lithography, the hexagonal mosaic appears when the interpore distance is ~350 nm (Figure 2-11(b)); small pores appear when the interpore distance is ~ 500 nm (Figure 2-11(c)). When the interpore distance increases to 800 nm, the small pore size and arrangement become irregular (Figure 2-11(d)). This means the guiding function of the FIB patterns needs to be considered with the anodization condition. For the phosphoric acid electrolyte, the naturally occurring pore distance is 300-500 nm.[11, 15] The FIB guided anodization can extend the interpore distance of an ordered pattern to both the smaller and the larger interpore distance directions. However, random pores form when the interpore distance is too large.

Figure 2-12 shows the square FIB patterns after the anodization. For Figures 2-12(a) to (c), the interpore distances are again 250 nm, 350 nm, and 500 nm respectively, an anodized result of Figures 2-10(a) - (c), correspondingly. After the anodization, the original square pore patterns remain the same as those from the FIB lithography. The pore size has grown from 50 nm to ~110 nm. The pore shape is more spherical. The white rings around the FIB patterned pores have also substantially diminished. This means the FIB patterned pores are effective in guiding the square pore pattern development, which is fundamentally different from the self-organized hexagonal pore pattern observed for pure anodization and opens exciting new areas for the FIB guided anodizaion. There have been reports on square pore pattern creation by nano-indentation and mold imprint guided anodization.[1, 48, 49] However, the pore pattern quality has much to be desired and the fundamental mechanism is not understood.

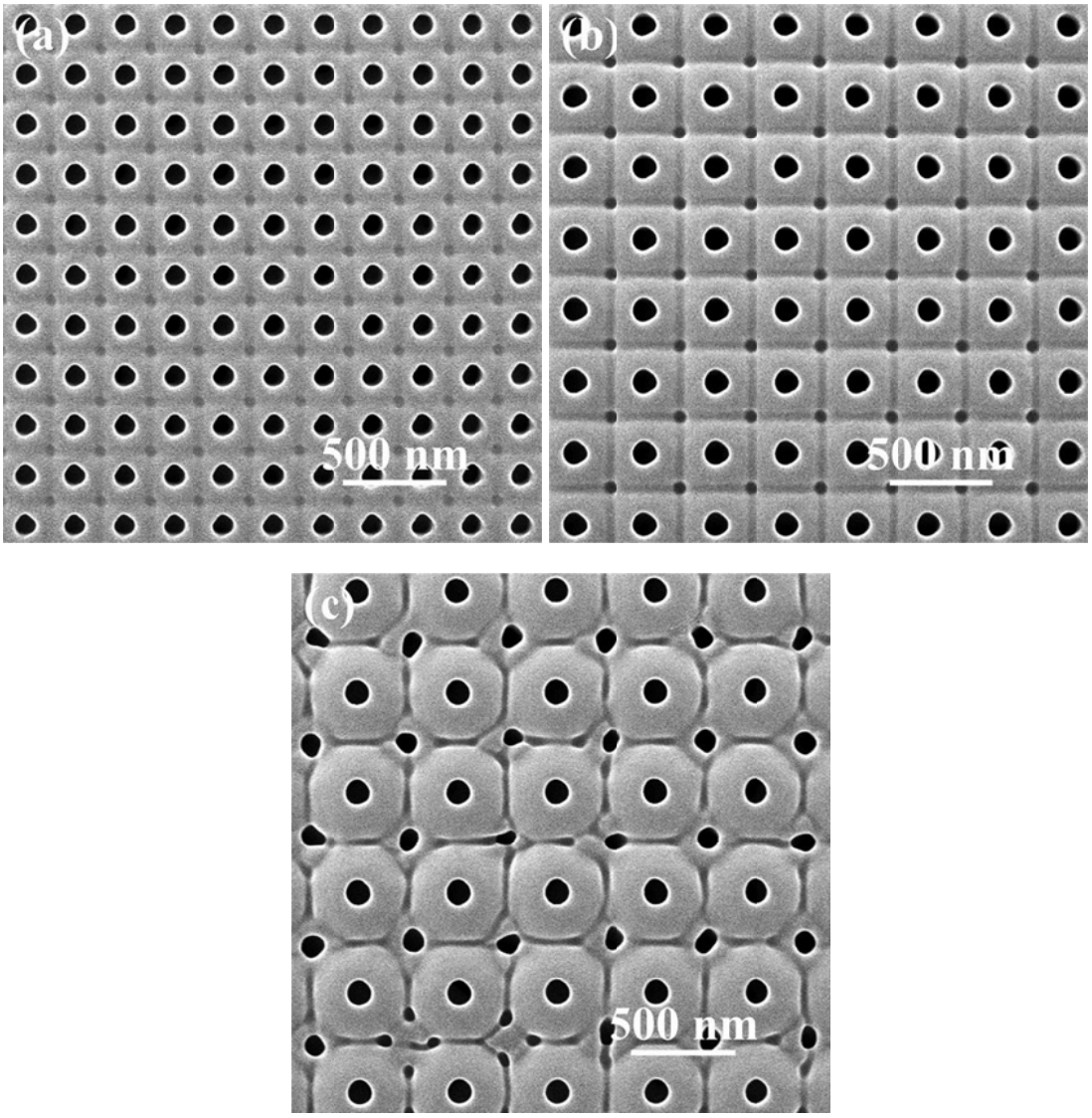

Figure 2-12 Images of the square patterns after the anodization. The interpore distances are 250 nm (a), 350 nm (b), and 500 nm (c).

For the FIB lithography guided square pore pattern anodization, a square cell starts to appear around each pore at 250 nm interpore distance (Figure 2-12(a)). At the corners of each square cell, smaller pores appear and mesh perfectly with the larger pores. In combination, a set of large pores with square arrangement is ideally meshed with a set

of small pores with the same square arrangement. As the interpore distance increases to 350 nm (Figure 2-12(b)), the square cell around each pore becomes more visible. The small pores at the corners of each square cell grow larger. Again, this shows the unique and versatile capability of the FIB guided anodization that has not been known so far. The square patterns, especially the meshed large and small pore sizes, represent exciting possibilities in patterning. When the interpore distance increases to 500 nm (Figure 2-12(c)), the small pores grow but their size and shape start to become irregular. Even though the growth of the small pores is still restricted in-between the FIB patterned large pores, multiple, instead of one, pores start to appear at some locations. This again indicates that the guiding function of the FIB patterned pores has an effective range. In this study, the interpore distance range for effective square pattern guidance is 200-400 nm.

Comparing the hexagonal patterns (Figures 2-11) and the square patterns (Figures 2-12), it can be observed that for the square patterns the interpore distance shifts to smaller values for the cell around each pore to appear, for the new small pores to form, and for the small pore packing to become irregular. The 200-400 nm effective interpore distance range for the square patterns overlaps to a certain extent with the 300-500 nm hexagonal pattern interpore distance. The fundamental cause is explained in the next section.

2.4.2 Mechanism of FIB guided anodization

2.4.2.1 Introduction to pure anodization

This study shows that the FIB patterned pores and the smaller pores from the anodization only can be meshed into well-organized and more sophisticated patterns after the anodization. The well-meshed large and small pore patterns can be created for both the hexagonal and square patterns. To understand this process, pure anodization should be examined first. Figure 2-13 shows the chemical reaction scheme of the pore formation. The Al metal acts as the anode and loses electrons at the metal/oxide interface:

$$Al \rightarrow Al^{3+}+3e^{-} \quad (1)$$

The Al^{3+} ions move from the metal layer to the electrolyte while the O^{2-} ions move in the reverse direction under the electrical field. The Al^{3+} and O^{2-} ions react and form the alumina barrier layer:

$$2Al^{3+}+3O^{2-} \rightarrow Al_2O_3 \quad (2)$$

At the oxide/electrolyte interface, the oxide layer dissolves:

$$Al_2O_3+6H^{+} \rightarrow 2Al^{3+}+3H_2O \quad (3)$$

For a given applied voltage, the continuous loss of Al at the metal/alumina interface and of Al_2O_3 at the alumina/electrolyte interface generates a steady anodization process and the pores grow deeper with time. For the self-organized pore growth by anodization alone, the electrical and mechanical stress fields around the pores are widely accepted as two major factors in dictating nanopore pattern formation [49-51].

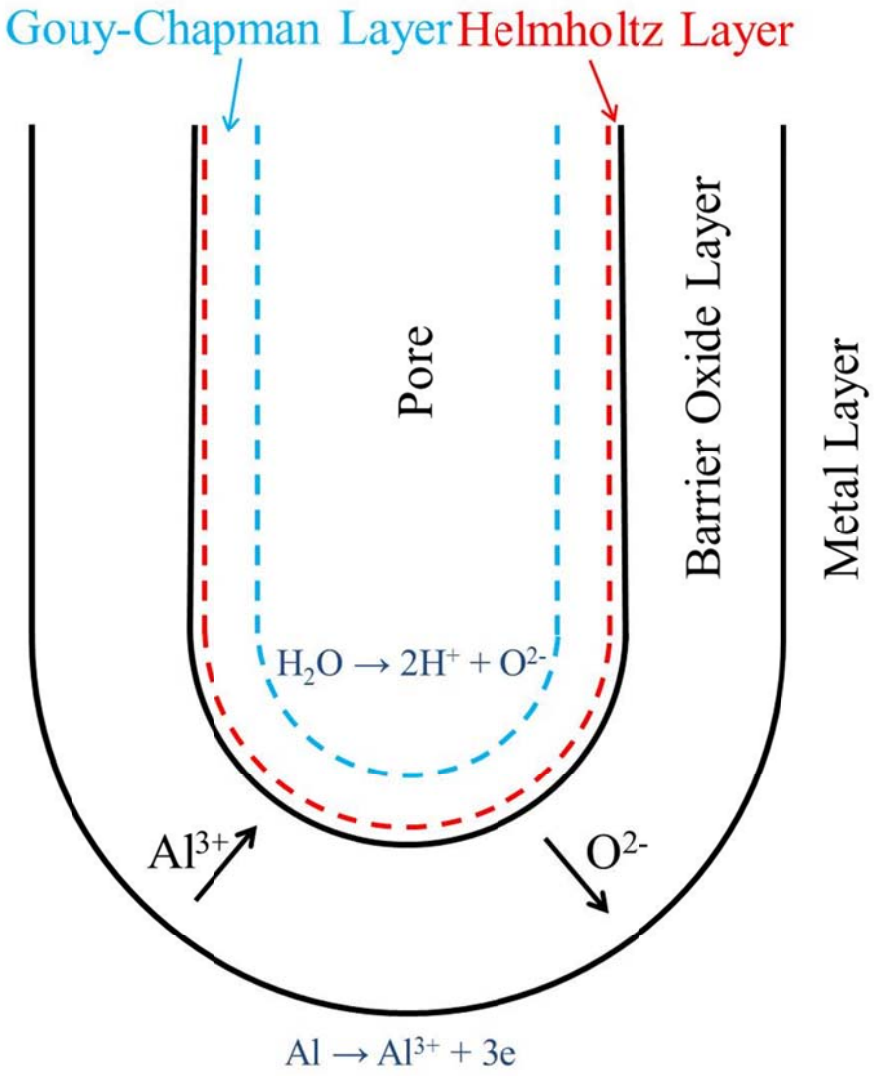

Figure 2-13 Chemical reaction scheme of the pore formation during anodization.

2.4.2.2 Electrical field effect

During the anodization, Al^{3+} ions are mobile in the oxidized AlO_x ($0<x<1.5$) layer around the pores and migrate from Al across the Al/AlO_x interface into the oxide barrier layer in the presence of the voltage. The Al^{3+} ions near the oxide/electrolyte interface drift through the AlO_x layer and eject into the solution at the oxide/electrolyte interface.

O^{2-} ions originated from water at the oxide/electrolyte interface and migrate into the barrier layer. More AlO_x forms in the barrier layer [52]. The AlO_x outer layer, sometimes aluminum hydroxide, at the oxide/electrolyte interface dissolves to maintain charge neutrality. Al^{3+} ion loss to the electrolyte is a prerequisite for the AlO_x barrier layer growth. For the pore growth front, there are four layers to be considered from the electrolyte to the Al metal: the Gouy-Chapman layer in the electrolyte near the oxide/electrolyte interface, the Helmholtz layer at the oxide/electrolyte interface, the growing oxide barrier layer, and the metal layer extending far into the Al (Figure 2-13) [53]. Faster ejection of Al^{3+} ions into the electrolyte and O^{2-} migration to the metal/oxide interface facilitate pore surface oxidation and pore growth. The oxide layer is generally O^{2-} deficient because of the slow O^{2-} diffusion.

Based on the field-enhanced oxide dissolution theory[54-58], the pore bottom ion dissolution and diffusion are the main events during the steady state anodization. As a result, preferential dissolution of AlO_x and pore growth mainly occur at the pore bottom. The voltage across the four layers from the electrolyte to the metal can be expressed as:

$$V_E = V_G + V_H + V_O + V_M \tag{2.1}$$

V_G, V_H, V_O, and V_M are the respective voltages across the Gouy-Chapman layer, the Helmholtz layer, the growing oxide layer, and the metal layer. V_H and V_M are related to the pH of the electrolyte and the metal resistivity. They do not change significantly with the anodization. V_H can be expressed as:[52]

$$V_H \approx -\frac{\alpha kT}{e}(pH) \tag{2.2}$$

In Eq. (2.2), k is Boltzmann constant, T is temperature, e represents the unite charge of a single electron, and α is a constant. V_O, however, increases significantly with the anodization time due to the oxide layer thickness increase. Since the overall applied

voltage V is mostly constant, V_G is sufficiently high at the beginning of the anodization. This ensures intense transport of the electrolyte ions to the oxide layer across the Gouy-Chapman layer. As V_O increases, V_G decreases and the ion transfer slows down. The formation of the oxide layer also slows down. If the pore bottom are assumed to have a hemispherical shape, the electrical field around the pores generated by charge Q can be approximately described as [59]:

$$E = \frac{1}{2\pi\varepsilon}\frac{Q}{L} \tag{2.3}$$

E is the electrical field at the point of interest. L is the distance between the charge center and the examined point. ε is the effective permittivity of the material:

$$\varepsilon = \frac{(R_2\varepsilon_1 - R_1\varepsilon_2)\ln\frac{R_2}{R_1}}{(R_2 - R_1)\ln\frac{R_2\varepsilon_1}{R_1\varepsilon_2}} \tag{2.4}$$

ε_1 and ε_2 are the dielectric permittivity of Al_2O_3 and Al respectively. R_1 is the pore diameter and R_2 is the distance from the pore center to the oxide barrier layer outer boundary. The derivation of Eq. (2.4) is given in the appendix. As Eq. (2.3) shows, the electrical field diminishes from the pore center to the barrier layer outer boundary. The pore growth in the direction perpendicular to the pore walls completely stops when the oxide layer is thick enough to reach $V_G = 0$. This is why the oxide barrier layer has a limited thickness and the interpore distance of pure anodization has a strong relationship with the applied voltage, which is 2.5 nm/V [11].

When the FIB patterned concaves are present, ion diffusion across the flat Al surface is much slower because the Al on the flat surface has much fewer defects and no foreign ion implantation compared to the surrounding areas of the concaves patterned by

the FIB. As the anodization continues, the pore growth rate in the pore diametrical direction decreases and reaches zero as is describe before. The applied voltage controls the thickness limitation of the barrier layer. In the pore depth direction, the continuous loss of Al at the metal/alumina interface and the dissolution of Al_2O_3 at the alumina/electrolyte interface reach a balance, generating a steady state anodization so that the pores grow deeper with time.

2.4.2.3 Mechanical stress effect

During the anodization, the Al material undergoes a series of changes under the electrical field, including the oxidization of the Al matrix to AlO_x. The mechanical stress field mainly comes from the volume expansion of Al to AlO_x due to the oxidation of the Al metal. The molar volume expansion can be expressed as:

$$V_m = \frac{M_{AlO_x}}{\rho_{AlO_x}} - \frac{M_{Al}}{\rho_{Al}} \tag{2.5}$$

V_m is the molar volume expansion of Al to AlO_x. M_{AlOx} and M_{Al} are the molecular weights of AlO_x and Al respectively. ρ_{AlOx} and ρ_{Al} are the densities of AlO_x and Al respectively. V_m equals to about 2.75 cm^3/mol when x is 1.5. For a specific anodization condition, the total amount of Al anodized can be estimated by measuring the Al^{3+} concentration in the electrolyte, Al_{aq}^{3+}, and relating this value to the total amount of oxidized Al calculated from the charge flow during the anodization ($Al_{tot} = 1/3\int Idt$). The volume expansion ξ can be determined by:

$$\xi = (1 - \frac{Al_{aq}^{3+}}{1/3\int Idt}) \times \frac{\rho_{Al}}{F_W \times \rho_{AlO_x}} \tag{2.6}$$

F_W is the weight fraction of Al^{3+} ions in AlO_x.[55] Based on Eq. (2.6), the volume expansion for a specific anodization condition can be calculated. For the self-organized pores to form, a force promoting the medium range order must exist in addition to the force promoting the short range order. It has been proposed that ξ should be ~0.2 for the medium range force to be effective.[55] This means a fairly large volume expansion is needed for the anodized pores to arrange. Even though this reported value might have a large error, the volume expansion ξ can be expected to be around 0.05 ~ 0.1.

During the anodization, the temperature around the pores increases because of the chemical reaction heat generated at the pore-electrolyte interface. This induces thermal stress because of the thermal expansion coefficient difference between Al and AlO_x. Since the heat can be dissipated fairly quickly in the electrolyte, the temperature increase is believed to be less than 20°C [60]. For simple estimation, thermal volume expansion ξ_T can be described as:

$$\xi_T = 3(a_{Al} - a_{Al_2O_3}) \times \Delta T \tag{2.7}$$

α_{Al} and α_{Al2O3} are the linear thermal expansion coefficients of Al and Al_2O_3 respectively. a_{Al} is 22.4 × 10^{-6} K^{-1} (Ref. [61]) and $a_{Al_2O_3}$ is 7.2 × 10^{-6} K^{-1} (Ref. [62]). ξ_T is about 8.52 × 10^{-4} K^{-1} when the temperature increase is 20°C. This value is much smaller than the volume expansion ξ from Al to Al_2O_3. Therefore, the thermal stress effect from the temperature increase can be ignored.

In addition to the oxidization during the anodization, the amorphization of Al crystalline phase and the implantation of the Ga^+ ions during the FIB patterning cause additional mechanical stress even before the anodization [63]. The effective range for this stress is around 24 nm from the ion beam bombardment center [64]. However, the exact

magnitude is FIB patterning condition related (ion dose, accelerating voltage, etc) and difficult to quantify because of the short range in the Al matrix.

In combination, the mechanical stress σ_M around the FIB patterned concaves can be expressed as:

$$\sigma_M = \sigma_\xi + \sigma_T + \sigma_A + \sigma_{Ga} \tag{2.8}$$

σ_ξ is volume expansion stress, σ_T is temperature induced stress, σ_A is Al amorphization stress, σ_{Ga} is Ga^+ ion implantation induced stress. Even though the magnitudes of σ_A and σ_{Ga} are unclear, σ substantially contributes to the preferential oxidation and dissolution of Al around the FIB patterned concaves into the electrolyte.

In addition to the mechanical stress field around each FIB patterned concave, the anodization is also affected by the ion diffusion across the Al/AlO_x interface. The amorphization of the Al crystalline phase and the implantation of the Ga^+ ions during the FIB patterning facilitate the ion diffusion because of the creation of easy diffusion paths. An Al-Ga alloy is also believed to react with water and generate Al_2O_3 [65]. The more active Al matrix contributes to the more dominating guiding function from the FIB patterned concaves, which can effectively guide the pore growth and pattern development during the anodization.

As mentioned above, since the ion diffusion is along the electrical field direction, the mechanical stress field has the same direction as the electrical field. Previous research indicated that the volume expansion of aluminum to alumina generates a repulsive force to the neighboring pores and promotes the formation of self-ordered patterns.[52] In addition, the ion implantation and Al amorphization from the FIB patterning also introduce stresses that are conducive to the patterned pore growth. The edges of the

patterned pores are active sites for the anodization. This explains why all the FIB patterned pores grow to a similar size (Figures 2-11 and Figures 2-12). The guiding effect of the FIB patterned pores is so effective that the square patterns from the FIB lithography can further develop into square pore arrays during the anodization.

2.4.2.3 FIB patterned pore characteristics

To describe the FIB guided pore pattern evolution process, two terms need to be defined first. The first term is the effective pore boundary, the shallow area in Figure 2-14, which represents the oxide barrier outer layer from each pore. The second is the terminal pore size, the dash circle in Figure 2-14, which represents the pore diameter when a pore stops growing without any constraining effect from its surroundings.

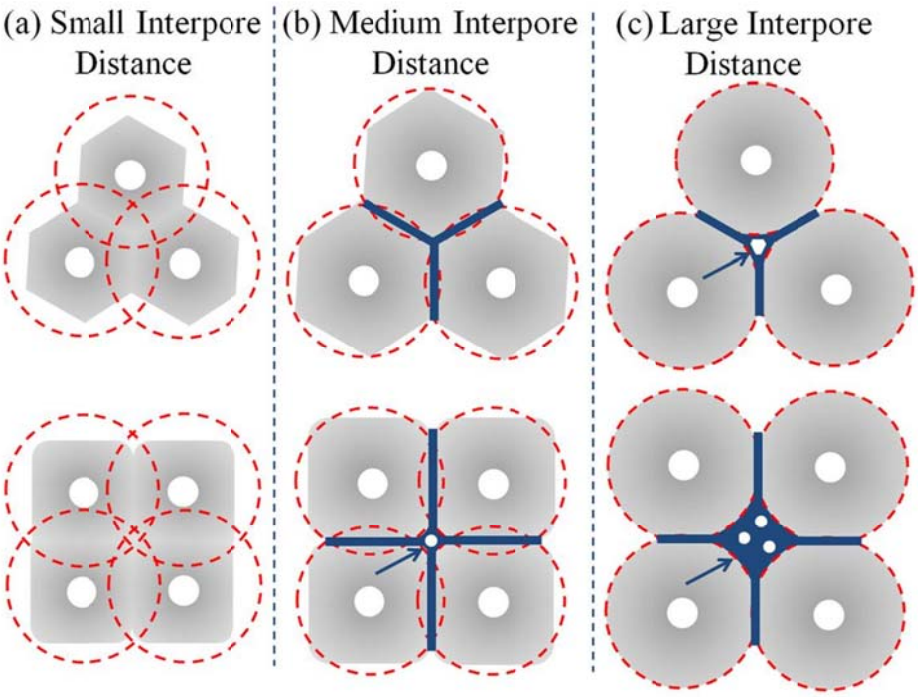

Figure 2-14 Interpore distance effect on the interaction of neighboring oxide barrier layers and new pore formation. The arrow indicates the bare Al surface areas that new pores may form. For the same terminal pore size and interpore distance, the square patterns have larger Al surface areas at the quadral junctions. As a result, new pores form and develop first.

The electrical field and the mechanical stress field affect the neighboring pore development by influencing the oxide barrier layer growth at various interpore distances. When the interpore distance is small, the effective pore boundaries from neighboring pores overlap before the pore size reaches the terminal pore size. No effective pore boundary is seen since the entire surface is AlO_x and the pore size is pseudo terminal pore size because the pores are constrained form growing larger. The FIB patterned pore arrangement remains intact and no new pore formation occurs. When the interpore

distance is larger than that of the pseudo terminal pore size condition but less than that allowing for the classical formation of new pores on the Al surface (Figure 2-11(a) and Figure 2-12(a)), the effective pore boundaries from adjacent pores may just overlap or are only slightly apart. Stripes in hexagonal and square patterns form depending on the pore pattern involved. The slightly separated effective pore boundaries may even allow new pore formation (Figure 2-11(b) and Figure 2-12(b)). When the interpore distance is much larger than that of the terminal pore case, the effective pore boundaries never overlap. Random pores form and grow in-between the FIB patterned pores (Figure 2-11(d) and Figuer 2-12(c)). For the anodization of square patterns at 20 mA/cm^2 current density in 0.3 M phosphoric acid at 0°C, the interpore distance should be < 150 nm to avoid effective pore boundary appearance and < 350 nm to avoid random pore formation. The terminal pore size is about 450 nm. For hexagonal pore patterns, the interpore distance should be < 250 nm to avoid effective pore boundary appearance and < 500 nm to avoid random pore formation. The terminal pore size is almost the same as that of the square patterns.

As observed, the interpore distance range for the new pore formation and meshing is 400-600 nm for the FIB patterned hexagonal pore arrays while it is 300-450 nm for the FIB patterned square pore arrays. These ranges look different and seem to indicate a shift to the smaller interpore distance values for the square pore patterns. A closer examination of these two types of patterns, however, reveals that the critical distance is the longest spacing for the two neighboring pore centers in a cell (Figure 2-15). “d” is the distance from a new small pore to a closest neighboring large pore and can be calculated for a given interpore distance “D” and arrangement of the large pores. For the hexagonal

patterns, the value is $d = \frac{\sqrt{3}}{3}D \approx 0.577D$. For the square patterns, $d = \frac{\sqrt{2}}{2}D \approx 0.707D$. So the d value is about the same for the two kinds of patterns in Figs. 2-11 and 2-12. The similar d value reveals that the fundamental mechanism for the new pore formation and growth is the same: the confinement of the available Al surface. Accordingly, the square patterns shift to a small interpore distance D for effective guidance of new pore formation and growth. The availability and shape/size of Al regions dictate if and how new pores grow. Additionally, new pore formation locations can be reliably predicted based on the FIB created pore patterns.

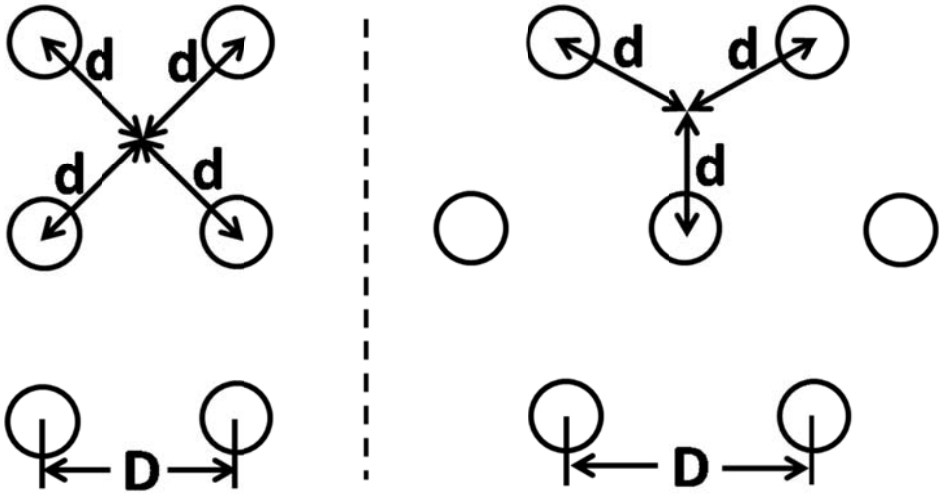

Figure 2-15 Schematic of the relationship between the interpore distance (D) and the small pore locations in square and hexagonal patterns.

2.4.2.4 Cross-section investigation

After the anodization, the pores grow deep; atomic force microscopy becomes unsuitable to measure the consistency among the pores. In consideration of this, to further understand the pore formation mechanism, a cross section SEM image of the anodized

pores is shown by FIB cutting of the square pattern with 350 nm interpore distance (Figure 2-16).

Figure 2-16(a) is from the pattern cross-sectioned about 250 nm deep while Figure 2-16(b) is from the pattern cross-sectioned nearly 2.5 μm deep. It can be seen that the square pore pattern arrangement is well maintained. In Figure 2-16(a), new, small pores form and mesh well with the large pores. The small pores reside in the symmetrical, quadral junction centers of the electrical field and the mechanical stress field. The small pores disappear when the sample is cross-sectioned to 2.5 μm deep and only the FIB patterned large pores can be seen (Figure 2-16(b)). This indicates that the FIB patterned pores develop first and grow deeper than the newly formed small pores. The exact pore depth difference is a function of the FIB patterned concave size and depth and the anodization condition. Another phenomenon is that the FIB patterned pores mostly grow in the vertical direction based on the field-enhanced oxide dissolution theory discussed before. The anodized pore size is not much larger than the FIB patterned concave size, 115 nm vs 60 nm. More importantly, the pore growth direction is not vertical but tilts outward at the pattern edges. This can be understood as follows. With the FIB pattern guiding effect, the pores in the patterned area develop first and faster than those in the surrounding un-patterned areas. The different pore depth growth rates induce unbalanced volume expansion at the pattern edges, which generates outward mechanical stress from the involving pore centers. The unbalanced mechanical stress causes the pores near the edges to tilt away from the pattern. For the specific anodization condition in Figure 2-16, the mechanical stress field affects not only the pores along the pattern edges but also four or five pores into the pattern. Another observation related to the mechanical stress field is

that the patterned surface is higher than the surrounding un-patterned area at about 40 nm (Figure 2-16(b)). A similar phenomenon was reported for the nano-indentation method.[32] The height difference is believed to result from the Al armophorization and Ga^+ implantation from the FIB patterning, the corresponding mechanical stress field difference, and the surface volume expansion difference at the initial anodization stage when the anodization rate at the patterned area is much higher than that at the un-patterned area. Figure 2-16(c) shows the oxide barrier layer along the pore walls and at the pore bottoms. The pore diameter at the pore bottom is about 115 nm, the same as that at the top. It confirms that uniform diameter pores can be generated using the FIB guided anodization.

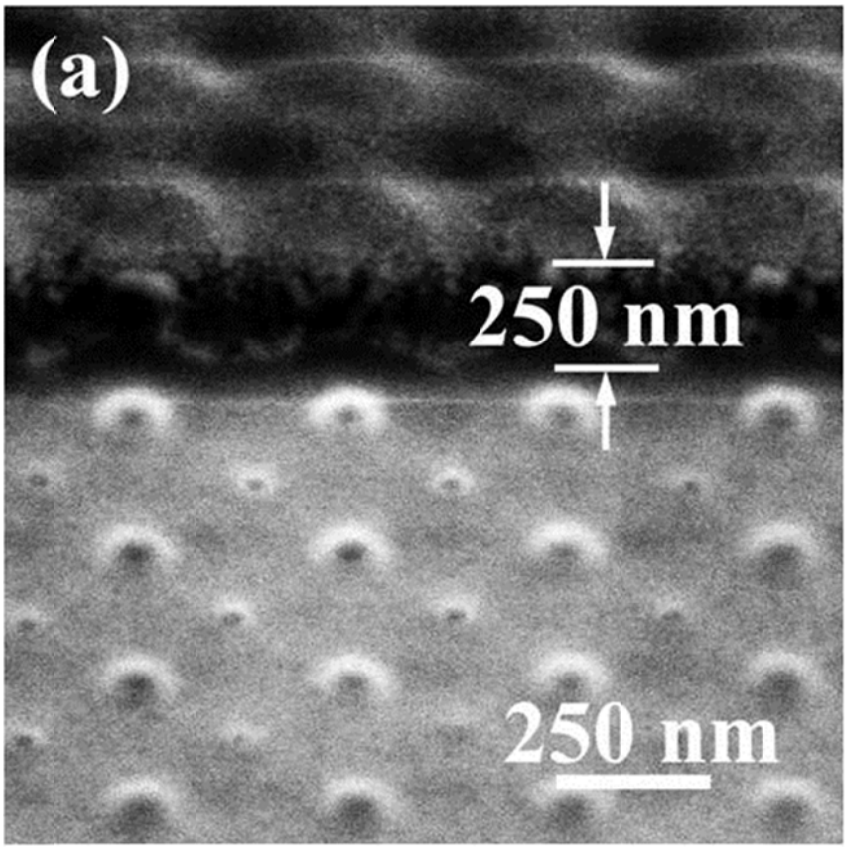
(a)
250 nm
250 nm

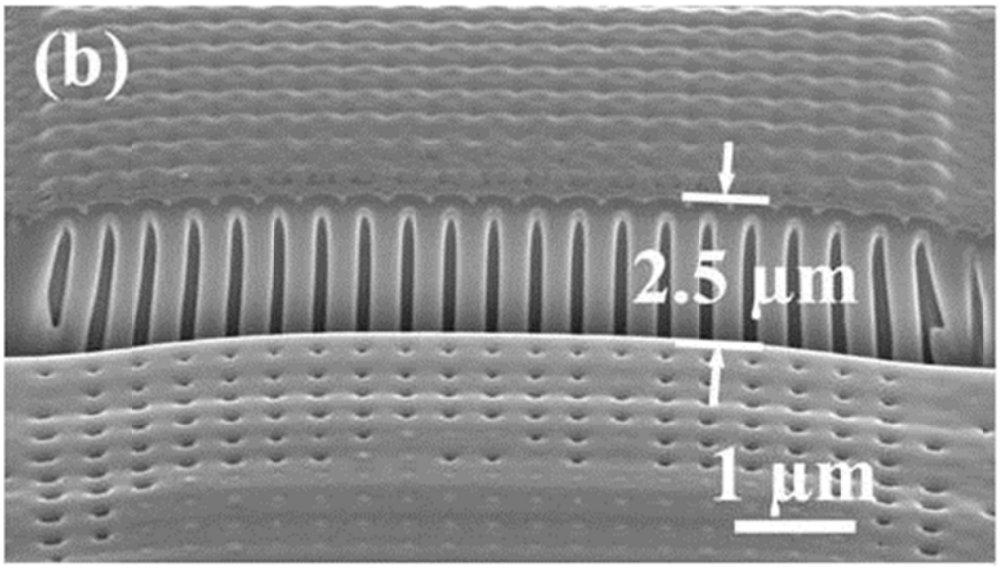
(b)
2.5 μm
1 μm

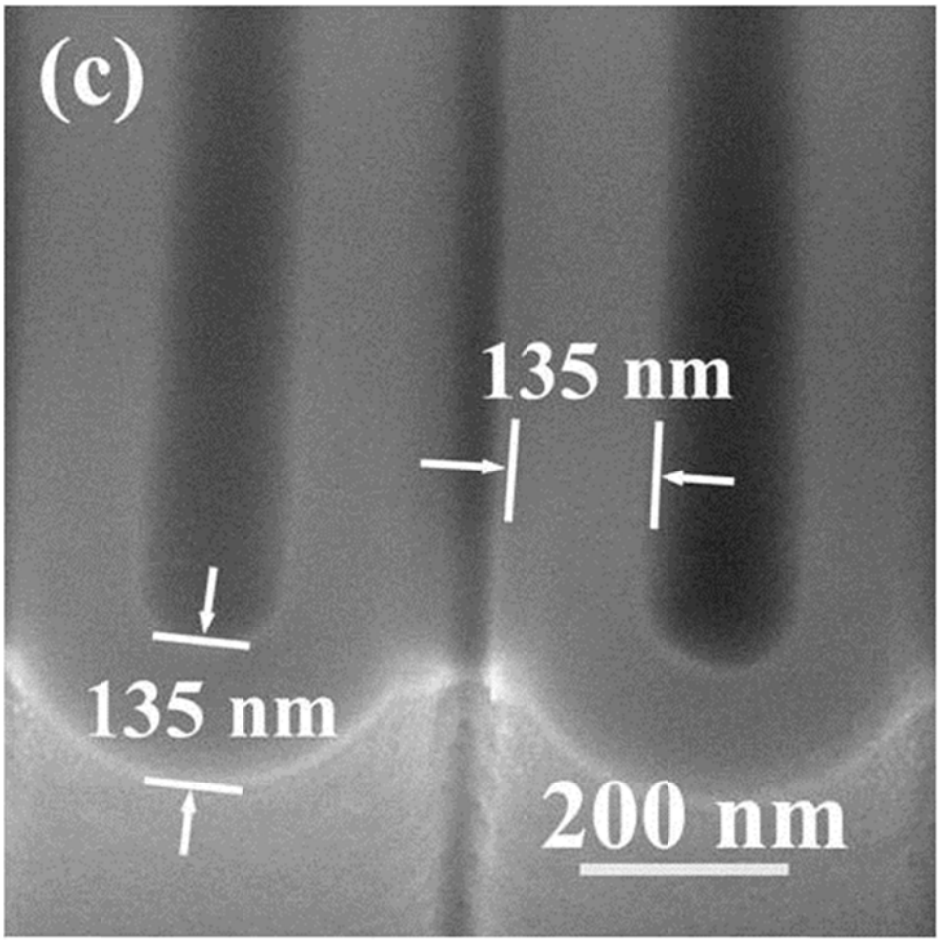

Figure 2-16 Cross section images of the anodized pores for a square pattern with 350 nm interpore distance. The anodization condition is 20 mA/cm^2 for 6 minutes in 0.3 M phosphoric acid. The anodization temperature is 0 °C. (a) Sample cross-sectioned 250 nm deep, (b) sample cross-sectioned 2.5 μm deep, (c) oxide barrier layer along the pore walls and at the pore bottoms. The viewing angle is tilted at 52° so the cross-section depth appears shorter.

2.4.2.5 FIB patterning across the grain boundary

For pure anodization, the stresses accumulated at grain boundaries and defects may disturb the formation and development of the ordered pore patterns. Grain boundaries are known to affect the pore array orientation and distort the ordered pattern for self-organized hexagonal pattern formation [66]. Figure 2-17 shows the Al grains by chemical etching the electropolished Al foil. It is very clear that after annealing in Ar condition, the grain size is roughly 500 μm. Large sized grains will benefit to the anodization research. The chemical etching electrolyte is composed of hydrochloric acid, nitric acid, and hydrofluoric acid with a volume ratio 50:47:3.

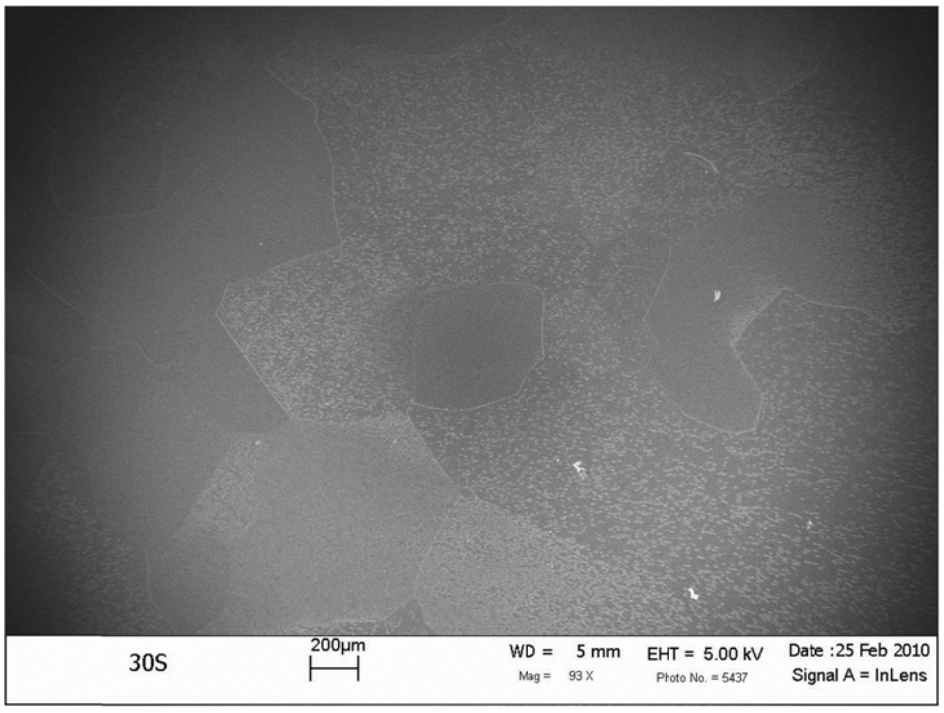

Figure 2-17 Al grain measured by chemical etching. Different crystal orientations have different chemical activity. The grains distinguish directly from the chemical etching morphologies.

EBSD (Figure 2-18) measurement of the annealed and electropolished Al foil matches with the chemical etching result, the grain size is in hundreds of microns scale. The EBSD test lasts approximately 12 hours. It successfully exhibits the crystal orientation rotation among the grains. The left part of Figure 2-18 shows the simulation result of the boundaries rotation angles.

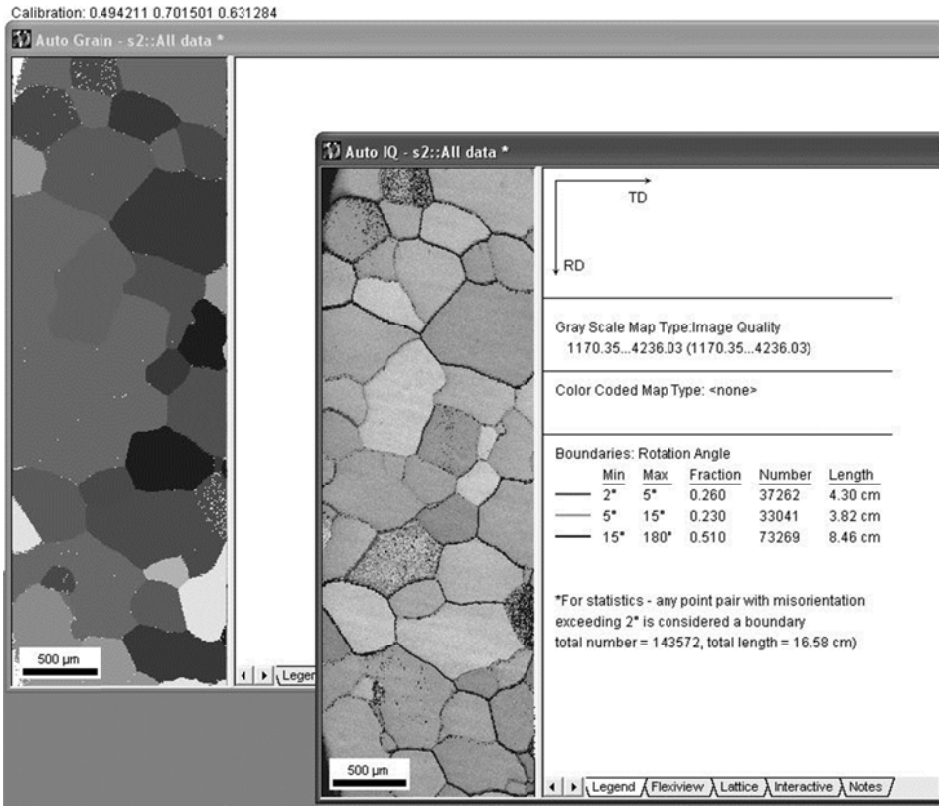

Figure 2-18 Al grains tested by EBSD. The calculation result (left) simulates the boundaries rotation angle among the grains.

Pore nucleation is more likely to occur randomly because both grain boundaries and defects distribute randomly. The FIB guided anodization is able to overcome the influence of grain boundaries and defects in dictating pore formation and growth. One

example to demonstrate such an advantage is the pore formation and growth across a grain boundary. In this study, a 10 μm × 10 μm FIB patterned hexagonal pore array (Figure 2-19(a)), which crosses a grain boundary, has been created using the beam spot exposure method. The total FIB exposure time is 60 s and the interpore distance for the hexagonal pattern is 250 nm. The arrow indicates the location (slightly tilted left to right from the image top to the bottom) where the grain boundary goes through the FIB pattern. Figure 2-19(b) shows the FIB guided anodization results. Outside the FIB patterned area, pores trend to generate along the grain boundary. The local stress and defects accumulates along the grain boundary may be the force triggering the pore growth. However, the patterned areas retain well organized pore arrangement after the anodization. The grain boundaries in the region do not have an obvious effect on the growth of the FIB patterned pores. The actual mechanism is still unclear. It is highly possible that the stress cause by Ga^{+} ion implantation and Al surface amorphization can overcome the grain boundary stress.

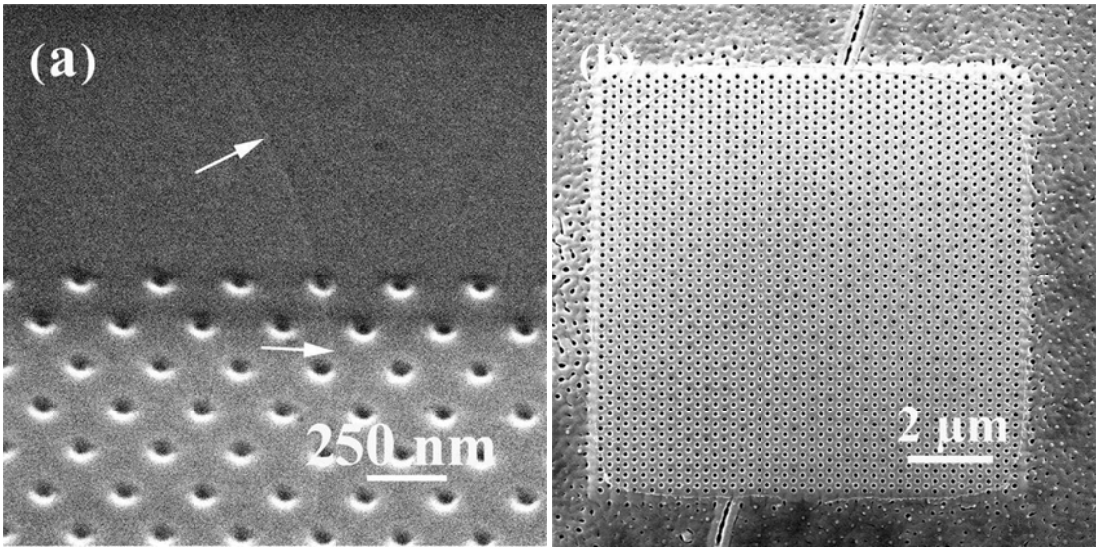

Figure 2-19 Hexagonal pore array formed across a grain boundary under the FIB guided anodization.

2.4.3 Novel patterns designed by FIB guided anodization

So far, the discussion has been focused on the guiding function of FIB patterned concaves with carefully designed arrangements. The electrical field and the mechanical stress field are spherical around each pore. It is very interesting to see the anodic results if the patterned pore shape is not spherical or the guiding pore arrangement is irregular. In previous work, the square and triangle shaped pores were created [51]. This section will focus on the pore shape and arrangement.

2.4.3.1 Elongated pores

In order to understand the effects of the electrical and mechanical stress fields, non-spherical pore shapes and unique pore arrangement can be created. Figure 2-20(a)

insert shows elongated guiding concaves created by the FIB patterning. The interpore distance for the ellipses is 350 nm. The concave size is 150 nm in the long direction and 50 nm in the short direction. The white rings around the FIB patterned concaves are the amorphorized and Ga^+ implanted Al regions. After the anodization in 0.3 M phosphoric acid with 20 mA/cm^2 current density for 6 mins at 0°C, the anodized Al layer around the FIB patterned concaves also shows an elliptical shape (Figure 2-20(a)); the pore size increases to 250 nm in the long direction and 80 nm in the short direction. The oxidized barrier layer thickness is about 135 nm. During the anodization, the elliptical pores grow under the guidance of the FIB patterned concaves. The electrical and mechanical stress fields guide the pore development. The local Al amorphization and the Ga^+ implantation activate the patterned concave surfaces and govern the initial growth of the FIB patterned pores. More importantly, the electrical field and the mechanical stress field due to the Al volume expansion exist in elliptical shapes to direct further pore growth. Since the pore centers are in a square arrangement and the interpore distance is 350 nm (the upper limit to avoid new pore formation), the effective pore boundaries appear but no new pores form. Figure 2-10(b) shows the new pore formation in-between the elongated pores after the anodization. The FIB patterned concave size is 100 nm in the long direction and 50 nm in the short direction. The FIB pattern interpore distance is 350 nm. The anodized pore size is about 140 nm in the long direction and 70 nm in the short direction. With the continued growth of the large pores during the anodization, new pores not only form but also grow in a unique direction. The new pores in Figure 2-20(b) are at the quadral junctions of the elongated pores and the pore growth direction is 90° from the long direction of the original elongated concaves. The distribution of the oxide barrier layers

and the formation of a new small pore is sketched in the insert of Figure 2-20(b). Areas I, II, III represent the anodized pore, the oxide barrier layer, and the newly generated pore respectively. The oxide layers outside the FIB patterned pores dictate the pore shapes and the growth direction.

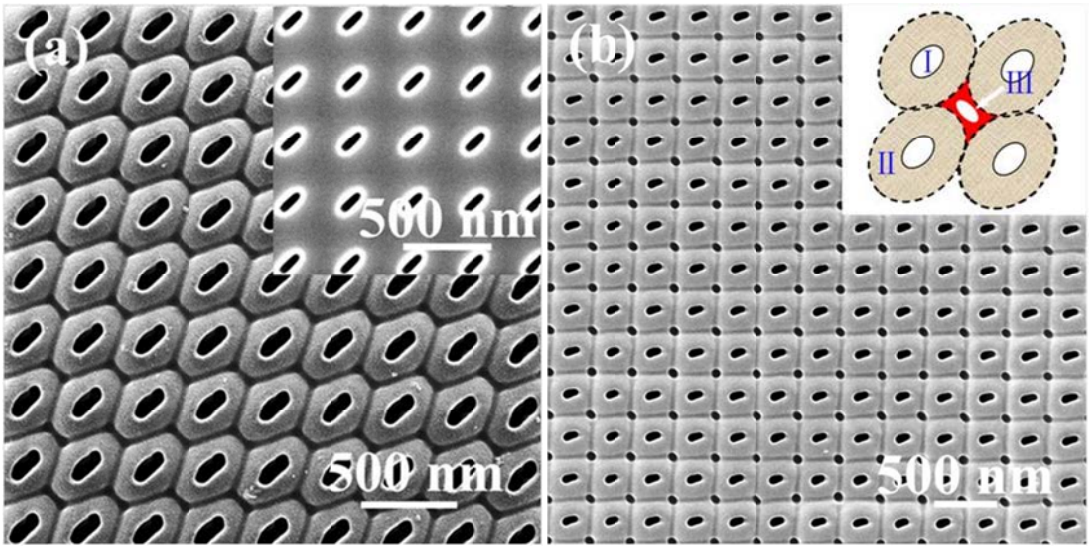

Figure 2-20 Square arrangements of elliptical pores at 350 nm interpore distance created by the FIB guided anodization at 20 mA/cm^2 current density for 6 mins in 0.3 M phosphoric acid. The anodization temperature is 0°C. (a) The long axis for the elliptical pores is 150 nm and the short axis is 50 nm. The insert shows the FIB patterned pores before the anodization. (b) The long axis for the elliptical pores is 100 nm and the short axis is 50 nm. The insert shows the formation process of the new, small pores. Areas I, II, III represent the anodized pore, the oxide barrier layer, and the newly generated pore respectively.

Comparing Figures 2-20(a) and (b), even though the FIB patterned guiding pores have the same 350 nm interpore distance, the anodization result is different. This is

mainly caused by the difference in the FIB patterned concave sizes. The FIB patterned pore size in Figure 2-20(a) is 150 nm while it is only 100 nm in Figure 2-20(b) in the long axis direction. The length of the FIB patterned pores in the short axis direction is 50 nm for both Figures 2-20(a) and (b). As a result of the different concave sizes in the long direction, the geometries of the electrical field and the mechanical stress field and the growth of the oxide barrier layers around the pores are different. The electrical field defines the pseudo terminal pore size. The mechanical stress field along the oxide barrier layer growth direction and the amorphorized and Ga^+ implanted layer outside the pores dictate the new pore shapes and the growth direction. As a result, non-spherical pores are created by the pre-defined, FIB patterned elliptical pores. Because of the shorter long axis dimension, there is some space for new pore formation in Figure 2-20(b). New pores grow almost perpendicular to the long axis direction and also have elongated shapes. The phenomenon in Figure 2-20 again proves that the FIB patterning can guide the pore arrangement, pore shape, and new pore formation. Both spherical and non-spherical pore shapes can be created. The interpore distance and the FIB patterned concave shapes need to be jointly considered for the FIB guided pore development.

2.4.3.2 Novel pattern design

Based on the above results, more exciting pore shapes and patterns can be created by controlling the FIB patterned concave shapes and the interpore distance. This can be achieved either by limiting the interpore distance to a small value so that no new pores can be generated, or by controlling the location and shape of the FIB patterned concaves so that new pores form and grow under the guidance of the FIB patterning. This offers a versatile approach of creating different pore shapes and unique pore patterns. An

interesting pattern generated is shown in Figures 2-21 by the FIB patterning of two overlaid square concave patterns at 45° followed by the anodization in 0.3 M phosphoric acid at 20 mA current density for 6 mins at 0°C. Figure 2-21(a) shows the original FIB pattern. As seen, the FIB patterned pores grow based on the designed pattern during the anodization (Figure 2-21(b)). The original FIB patterned pores grow and mesh with the new pores when the interpore distance is large enough for new pores to form. When the un-patterned Al surface area among the oxide barrier layers is large, new pores form randomly. The work rotating the two square arrangements to different overlap angles, so as to obtain different periods, is now on going.

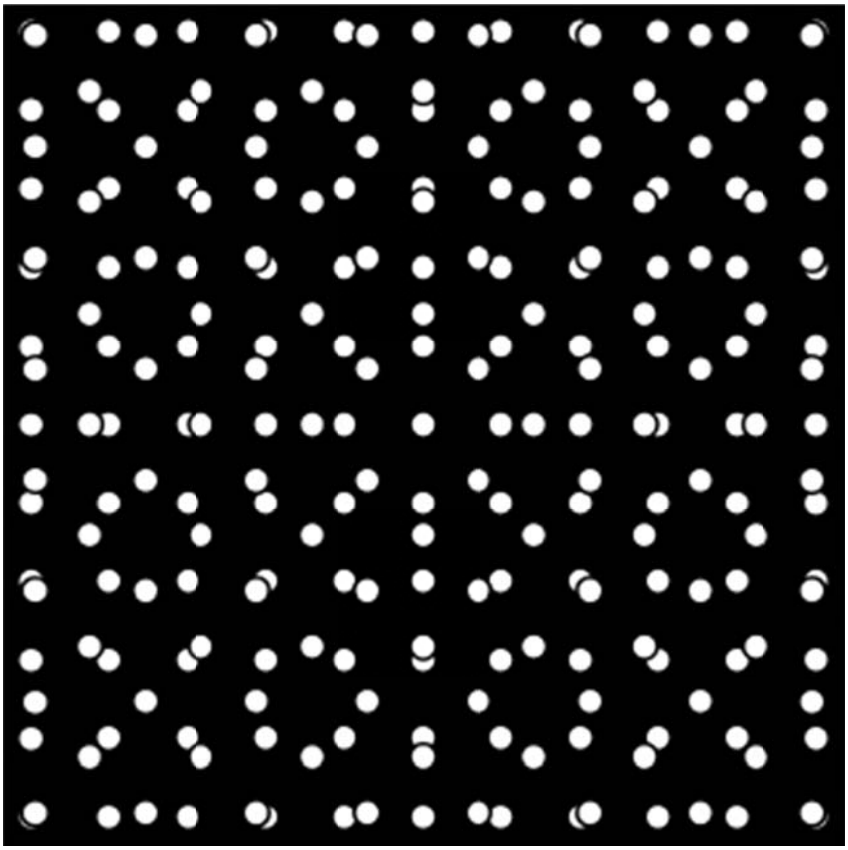

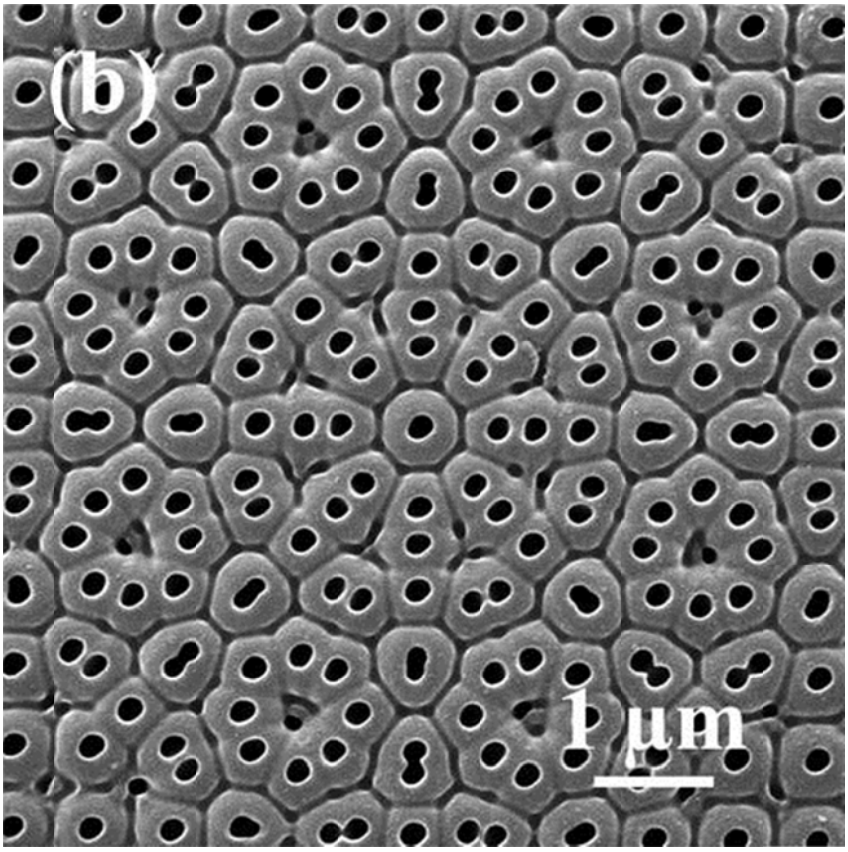

Figure 2-21 Anodization result of two FIB guiding patterns overlaid at 45°. (a) as-designed FIB pattern; (b) anodization result carried out at 20 mA/cm^2 current density for 6 mins in 0.3 M phosphoric acid at 0°C.

2.4.4 FIB patterns across large area

The FIB patterned area is limited, depends on the equipment itself. The FEI Helios NanoLab 600 Dual Beam FIB can mill in a size of 600 µm × 600 µm. theoretically; it is possible to exactly move the sample to make continuous patterns. It has mentioned before that small FIB pattern have strong edge effect. To reduce the edge effect, pattern area as large as 30 µm × 30 µm was investigated (Figure 2-22(a)). The image shows clearly that FIB can uniformly pattern through a large area. After the anodization (Figure 2-22(b)),

the FIB milled ordered pattern maintains well. The whole anodic patterned surface is also very uniform. It improves that FIB guided anodization can be applied to the large area.

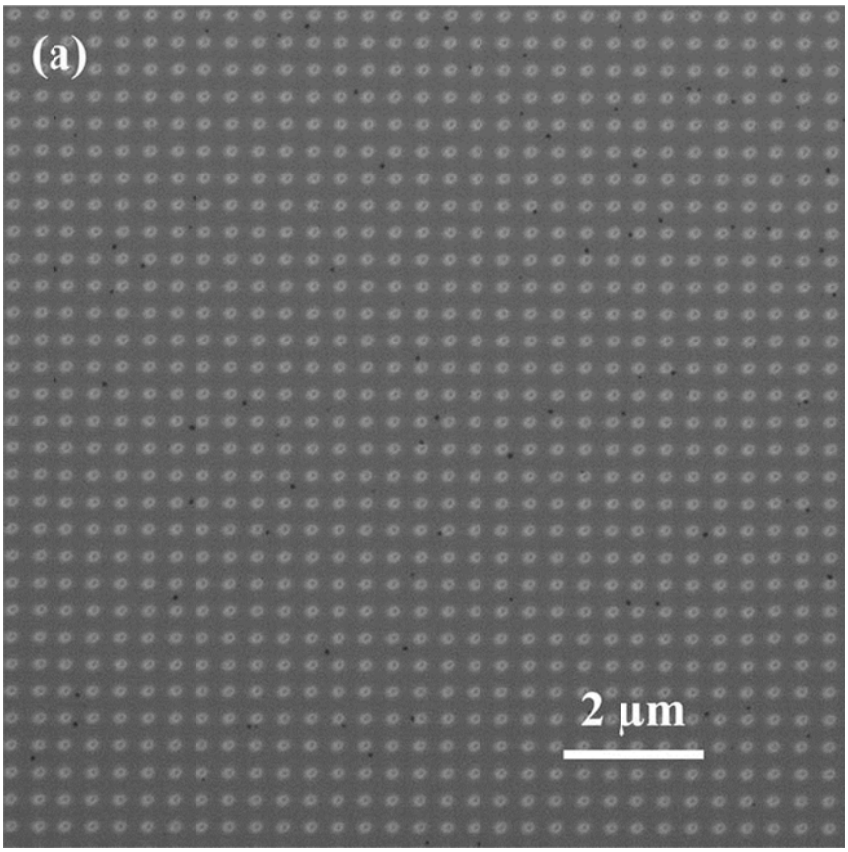

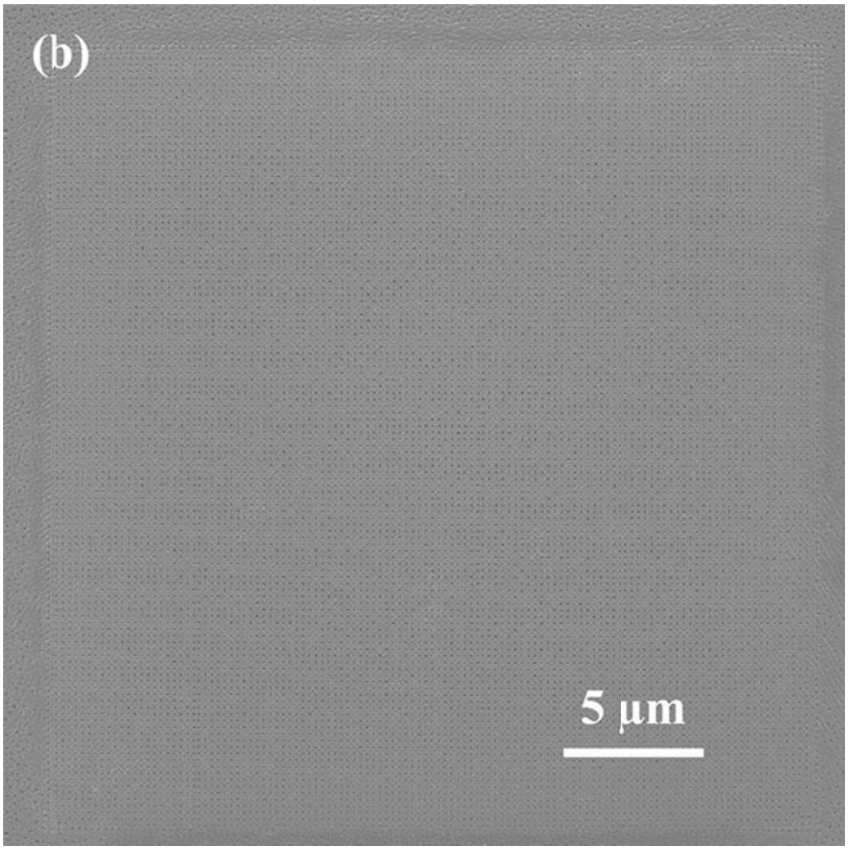

Figure 2-22 FIB guided 30 μm × 30 μm sized pattern. (a) FIB guided pattern, (b) pattern develop after anodization.

However, we need to face up to potential difficulty for large area patterning. The surface roughness will influence the nanoimprint method, causing misalignment problem. It will also lead to "focus" problem for FIB guided anodization, even though this method can better tolerate the surface roughness. Ion beam out of focus will influence the pore shape, size and depth. In this case, a flat surface and good polishing are quite necessary.

2.5 Conclusion

This chapter discusses FIB guided anodization. Hexagonal and square pore pattern arrays at various interpore distances are successfully created by FIB lithography guided anodization. Depending on the interpore distance and pore arrangement, the FIB patterned arrays can grow as patterned, periodic cell patterns can appear around the patterned pores, or small pores can appear and grow at the conjunctions of the oxide layers of the surrounding pores. The new, small pores mesh with the FIB patterned large pores well when the interpore distance is within a certain range. The guiding role of the FIB patterned pores is also demonstrated for large area anodization across grain boundaries.

The fundamental mechanisms for the new findings are discussed. Two important fields determine the existing pore growth and new pore formation: electrical field and mechanical stress field. The electrical field defines terminal pore size and pore growth rate. New pores form when the interpore distance of the guiding patterns is larger than that required for the pseudo terminal pore size. Mechanical stress field affects the pore arrangement and the oxide layer growth direction. As a combined result of the above two elements, non-hexagonal pore arrangement, non-spherical pores, and controlled meshing of the FIB patterned pores and newly anodization pores are achieved. The formation of the small pores can predict, as well as their shapes and locations.

2.6 References

1. Asoh, H., K. Nishio, M. Nakao, A. Yokoo, T. Tamamura, and H. Masuda, Fabrication of ideally ordered anodic porous alumina with 63 nm hole periodicity using sulfuric acid. *Journal of Vacuum Science & Technology B*, 2001. **19**(2) p. 569-572.
2. Sulka, G.D., S. Stroobants, V. Moshchalkov, G. Borghs, and J.P. Celis, Synthesis of well-ordered nanopores by anodizing aluminum foils in sulfuric acid. *Journal of the Electrochemical Society*, 2002. **149**(7) p. D97-D103.
3. Masuda, H., F. Hasegwa, and S. Ono, Self-ordering of cell arrangement of anodic porous alumina formed in sulfuric acid solution. *Journal of the Electrochemical Society*, 1997. **144**(5) p. L127-L130.
4. Chu, S.Z., K. Wada, S. Inoue, M. Isogai, and A. Yasumori, Fabrication of ideally ordered nanoporous alumina films and integrated alumina nanotubule arrays by high-field anodization. *Advanced Materials*, 2005. **17**(17) p. 2115.
5. Lee, K., Y. Tang, and M. Ouyang, Self-Ordered, Controlled Structure Nanoporous Membranes Using Constant Current Anodization. *Nano Letters*, 2008. **8**(12) p. 4624-4629.
6. Kanakala, R., P.V. Singaraju, R. Venkat, and B. Das, Modeling of porous alumina template formation under constant current conditions. *Journal of the Electrochemical Society*, 2005. **152**(1) p. J1-J5.

7. Asoh, H., K. Nishio, M. Nakao, T. Tamamura, and H. Masuda, Conditions for fabrication of ideally ordered anodic porous alumina using pretextured Al. *Journal of the Electrochemical Society*, 2001. **148**(4) p. B152-B156.

8. Li, F.Y., L. Zhang, and R.M. Metzger, On the growth of highly ordered pores in anodized aluminum oxide. *Chemistry of Materials*, 1998. **10**(9) p. 2470-2480.

9. Masuda, H., H. Yamada, M. Satoh, H. Asoh, M. Nakao, and T. Tamamura, Highly ordered nanochannel-array architecture in anodic alumina. *Applied Physics Letters*, 1997. **71**(19) p. 2770-2772.

10. Zhao, N.Q., X.X. Jiang, C.S. Shi, J.J. Li, Z.G. Zhao, and X.W. Du, Effects of anodizing conditions on anodic alumina structure. *Journal of Materials Science*, 2007. **42**(11) p. 3878-3882.

11. Masuda, H., K. Yada, and A. Osaka, Self-ordering of cell configuration of anodic porous alumina with large-size pores in phosphoric acid solution. *Japanese Journal of Applied Physics Part 2-Letters*, 1998. **37**(11A) p. L1340-L1342.

12. Li, A.P., F. Muller, A. Birner, K. Nielsch, and U. Gosele, Hexagonal pore arrays with a 50-420 nm interpore distance formed by self-organization in anodic alumina. *Journal of Applied Physics*, 1998. **84**(11) p. 6023-6026.

13. Lee, W., R. Ji, U. Gosele, and K. Nielsch, Fast fabrication of long-range ordered porous alumina membranes by hard anodization. *Nature Materials*, 2006. **5**(9) p. 741-747.

14. Garcia-Vergara, S.J., H. Habazaki, P. Skeldon, and G.E. Thompson, Formation of porous anodic alumina at high current efficiency. *Nanotechnology*, 2007. **18**(41)

15. Ono, S., M. Saito, and H. Asoh, Self-ordering of anodic porous alumina induced by local current concentration: Burning. *Electrochemical and Solid State Letters*, 2004. **7**(7) p. B21-B24.

16. Tian, Z.P., K. Lu, and B. Chen, Unique nanopore pattern formation by focused ion beam guided anodization. *Nanotechnology*, 2010. **21**(40)

17. Rauf, A., M. Mehmood, Z.H. Yuan, D. Yue-Qin, and A. Waheed, The effects of ordering on the morphology of two-layer alumite-Forming a patterned interface. *Materials Letters*, 2009. **63**(18-19) p. 1601-1604.

18. Shingubara, S., K. Morimoto, H. Sakaue, and T. Takahagi, Self-organization of a porous alumina nanohole array using a sulfuric/oxalic acid mixture as electrolyte. *Electrochemical and Solid State Letters*, 2004. **7**(3) p. E15-E17.

19. Kashi, M.A., A. Ramazani, M. Noormohammadi, M. Zarei, and P. Marashi, Optimum self-ordered nanopore arrays with 130-270nm interpore distances formed by hard anodization in sulfuric/oxalic acid mixtures. *Journal of Physics D-Applied Physics*, 2007. **40**(22) p. 7032-7040.

20. Lippens, B.C. and J.J. Steggerda, Physical and Chemical Aspects of Adsorbents and Catalysts. *Ed. B.G. Linsen, Acad. Press, London-N.Y.*, 1970.

21. Johnson, M.F.L. and J. Mooi, The Origin and Types of Pores in Some Alumina Catalysts. *JOURNAL OF CATALYSIS*, 1968. **10** p. 342-354.

22. Li, B.T., K. Maruyama, M. Nurunnabi, K. Kunimori, and K. Tomishige, Temperature profiles of alumina-supported noble metal catalysts in autothermal reforming of methane. *Applied Catalysis a-General*, 2004. **275**(1-2) p. 157-172.

23. Masuda, H., M. Yamada, F. Matsumoto, S. Yokoyama, S. Mashiko, M. Nakao, and K. Nishio, Lasing from two-dimensional photonic crystals using anodic porous alumina. *Advanced Materials*, 2006. **18**(2) p. 213.

24. Masuda, H., M. Ohya, K. Nishio, H. Asoh, M. Nakao, M. Nohtomi, A. Yokoo, and T. Tamamura, Photonic band gap in anodic porous alumina with extremely high aspect ratio formed in phosphoric acid solution. *Japanese Journal of Applied Physics Part 2-Letters*, 2000. **39**(10B) p. L1039-L1041.

25. Yanagishita, T., K. Nishio, and H. Masuda, Two-dimensional photonic crystal composed of ordered polymer nanopillar arrays with high aspect ratios using anodic porous alumina templates. *Applied Physics Express*, 2008. **1**(1) p. 012002.

26. Yanagishita, T., T. Kondo, K. Nishio, and H. Masuda, Optimization of antireflection structures of polymer based on nanoimprinting using anodic porous alumina. *Journal of Vacuum Science & Technology B*, 2008. **26**(6) p. 1856-1859.

27. Yanagishita, T., K. Nishio, and H. Masuda, Antireflection polymer hole array structures by imprinting using metal molds from anodic porous alumina. *Applied Physics Express*, 2008. **1**(6).

28. Yanagishita, T., K. Nishio, and H. Masuda, Anti-Reflection Structures on Lenses by Nanoimprinting Using Ordered Anodic Porous Alumina. *Applied Physics Express*, 2009. **2**(2).

29. Yanagishita, T., K. Yasui, T. Kondo, Y. Kawamoto, K. Nishio, and H. Masuda, Antireffection polymer surface using anodic porous alumina molds with tapered holes. *Chemistry Letters*, 2007. **36**(4) p. 530-531.

30. Yuzhakov, V.V., H.C. Chang, and A.E. Miller, Pattern formation during electropolishing. *Physical Review B*, 1997. **56**(19) p. 12608-12624.

31. Wu, M.T., I.C. Leu, and M.H. Hon, Effect of polishing pretreatment on the fabrication of ordered nanopore arrays on aluminum foils by anodization. *Journal of Vacuum Science & Technology B*, 2002. **20**(3) p. 776-782.

32. Jaafar, M., D. Navas, M. Hernandez-Velez, J.L. Baldonedo, M. Vazquez, and A. Asenjo, Nanoporous alumina membrane prepared by nanoindentation and anodic oxidation. *Surface Science*, 2009. **603**(20) p. 3155-3159.

33. Masuda, H., K. Kanezawa, and K. Nishio, Fabrication of ideally ordered nanohole arrays in anodic porous alumina based on nanoindentation using scanning probe microscope. *Chemistry Letters*, 2002(12) p. 1218-1219.

34. Yasui, K., T. Morikawa, K. Nishio, and H. Masuda, Patterned magnetic recording media using anodic porous alumina with single domain hole configurations of 63 nm hole interval. *Japanese Journal of Applied Physics Part 2-Letters & Express Letters*, 2005. **44**(12-15) p. L469-L471.

35. Choi, J., G. Sauer, K. Nielsch, R.B. Wehrspohn, and U. Gosele, Hexagonally arranged monodisperse silver nanowires with adjustable diameter and high aspect ratio. *Chemistry of Materials*, 2003. **15**(3) p. 776-779.

36. Choi, J., K. Nielsch, M. Reiche, R.B. Wehrspohn, and U. Gosele, Fabrication of monodomain alumina pore arrays with an interpore distance smaller than the lattice constant of the imprint stamp. *Journal of Vacuum Science & Technology B*, 2003. **21**(2) p. 763-766.

37. Sun, Z.J. and H.K. Kim, Growth of ordered, single-domain, alumina nanopore arrays with holographically patterned aluminum films. *Applied Physics Letters*, 2002. **81**(18) p. 3458-3460.

38. Liu, N.W., A. Datta, C.Y. Liu, and Y.L. Wang, High-speed focused-ion-beam patterning for guiding the growth of anodic alumina nanochannel arrays. *Applied Physics Letters*, 2003. **82**(8) p. 1281-1283.

39. Peng, C.Y., C.Y. Liu, N.W. Liu, H.H. Wang, A. Datta, and Y.L. Wang, Ideally ordered 10 nm channel arrays grown by anodization of focused-ion-bearn patterned aluminum. *Journal of Vacuum Science & Technology B*, 2005. **23**(2) p. 559-562.

40. Liu, C.Y., A. Datta, and Y.L. Wang, Ordered anodic alumina nanochannels on focused-ion-beam-prepatterned aluminum surfaces. *Applied Physics Letters*, 2001. **78**(1) p. 120-122.

41. Lu, K., Hierarchical and Nanosized Pattern Formation Using Dual Beam Focused Ion Beam Microscope. *Journal of Nanoscience and Nanotechnology*, 2009. **9**(4) p. 2598-2602.

42. Liu, N.W., A. Datta, C.Y. Liu, C.Y. Peng, H.H. Wang, and Y.L. Wang, Fabrication of anodic-alumina films with custom-designed arrays of nanochannels. *Advanced Materials*, 2005. **17**(2) p. 222.

43. Liu, N.W., C.Y. Liu, H.H. Wang, C.F. Hsu, M.Y. Lai, T.H. Chuang, and Y.L. Wang, Focused-ion-beam-based selective closing and opening of anodic alumina nanochannels for the growth of nanowire arrays comprising multiple elements. *Advanced Materials*, 2008. **20**(13) p. 2547.

44. Chen, B., K. Lu, and Z. Tian, Gradient and Alternating Diameter Nanopore Templates by Focused Ion Beam Guided Anodization. *Electrochimica Acta*, 2010.

45. Lu, K. and J.Z. Zhao, Focused Ion Beam Lithography and Anodization Combined Nanopore Patterning. *Journal of Nanoscience and Nanotechnology*, 2010. **10**(10) p. 6760-6768.

46. Jinzhong., Z., L. Kathy, C. Bo, and T. Zhipeng, Patterning by focused ion beam assisted anodization. *Ceramic Transactions, John Wiley & Sons, accepted*, 2010.

47. Tseng, A.A., Recent developments in nanofabrication using focused ion beams. *Small*, 2005. **1**(10) p. 924-939.

48. Asoh, H., S. Ono, T. Hirose, M. Nakao, and H. Masuda, Growth of anodic porous alumina with square cells. *Electrochimica Acta*, 2003. **48**(20-22) p. 3171-3174.

49. Asoh, H., S. Ono, T. Hirose, I. Takatori, and H. Masuda, Detailed observation of cell junction in anodic porous alumina with square cells. *Japanese Journal of Applied Physics Part 1-Regular Papers Short Notes & Review Papers*, 2004. **43**(9A) p. 6342-6346.

50. I, V.A., O.E. A, and K.A. A, Self-organized growth mechanism for porous aluminum anodic oxide. *Russ. Microelectron*, 2007. **36** p. 384-391.

51. Masuda, H., H. Asoh, M. Watanabe, K. Nishio, M. Nakao, and T. Tamamura, Square and triangular nanohole array architectures in anodic alumina. *Advanced Materials*, 2001. **13**(3) p. 189-192.

52. Jessensky, O., F. Muller, and U. Gosele, Self-organized formation of hexagonal pore arrays in anodic alumina. *Applied Physics Letters*, 1998. **72**(10) p. 1173-1175.

53. Thompson, G.E. and G.C. Wood, Porous Anodic Film Formation on Aluminum. *Nature*, 1981. **290**(5803) p. 230-232.

54. Choi, J., Y. Luo, R.B. Wehrspohn, R. Hillebrand, J. Schilling, and U. Gosele, Perfect two-dimensional porous alumina photonic crystals with duplex oxide layers. *Journal of Applied Physics*, 2003. **94**(8) p. 4757-4762.

55. P., H.T. and M.N. F., A mechanism for the formation of porous anodic oxide films on aluminum. *J. Phys. Chem. Solids*, 1959. **9** p. 97-99.

56. P., O.s.J. and W.G. C., The morphology and mechanism of formation of porous anodic films on aluminium. *Proc. Roy. Soc. Lond.*, 1970. **317** p. 511-543.

57. P., P.V. and S.V. I., Theoretical modelling of porous oxide growth on aluminium. *J. Phys. D: Appl. Phys.*, 1992. **25** p. 1258-1263.

58. Thamida, S.K. and H.C. Chang, Nanoscale pore formation dynamics during aluminum anodization. *Chaos*, 2002. **12**(1) p. 240-251.

59. Choi, J., R.B. Wehrspohn, and U. Gosele, Mechanism of guided self-organization producing quasi-monodomain porous alumina. *Electrochimica Acta*, 2005. **50**(13) p. 2591-2595.

60. Saleh, R.M. and A.A. Elhosary, Thermal Phenomena during Anodizing of Aluminum in Sulfuric-Acid. *Journal of Thermal Analysis*, 1983. **26**(2) p. 263-268.

61. Lide, D.R., CRC Handbook of Chemistry and Physics, CRC Press: Boston. 1992. **12-119**.

62. Schneider, S.J., Engineered Materials Handbook. *Ceramics and Glasses, ASM International, Cleveland, OH, 30*, 1991. **4**.

63. Takahashi, H., K. Fujimoto, H. Konno, and M. Nagayama, Distribution of Anions and Protons in Oxide-Films Formed Anodically on Aluminum in a Phosphate Solution. *Journal of the Electrochemical Society*, 1984. **131**(8) p. 1856-1861.

64. Giannuzzi, L.A. and F.A. Stevie, Introduction to Focused Ion Beams: Instrumentation, Theory, Techniques and Practice. *Springer, NY*, 2005.

65. Woodall, J.M., Making of hydrogen from aluminum. *http://hydrogen.ecn.purdue.edu/*, 2007.

66. Hillebrand, R., F. Müller, K. Schwirn, W. Lee, and M. Steinhart, Quantitative Analysis of the Grain Morphology in Self-Assembled Hexagonal Lattices. *ACS Nano*, 2008. **2**(5) p. 913-920.

Chapter 3 Ion beam guided anodic titania

3.1 Introduction to anodic titania

Titanium oxide is a multi-functional material that has been widely used as photocatalysts,[1, 2] hydrophilic/hydrophobic substrates,[3, 4] and sensors.[5, 6] In recent years, interest has increased tremendously because of the extraordinary photo response of TiO_2 under ultraviolet light [7].

Anodic TiO_2 is generated by anodizing Ti metal and Ti alloys. The morphology of anodic TiO_2 is quite different from anodic alumina. Instead of growing a porous surface, anodic TiO_2 gives a nanotube outlook. In this section, anodic TiO_2 is discussed.

3.1.1 Anodization under different electrolytes

Similar to anodic alumina, researchers have already tried to grow TiO_2 nanotubes in different electrolytes. They can be categorized as acid based electrolytes and neutral electrolytes.

3.1.1.1 Andization under acid electrolytes

The first developed electrolytes are acid electrolytes. The Ti metal is very stable to many acids, only HF can successfully create TiO_2 nanotubes. Usually, the anodization is carried out at room temperature [8]. Using HF based electrolyte, the suitable applied voltage is limited, ~ 20 V. Sometimes the nanotube length is less than 1 μm [9]. Previous work indicated that the ultimate nanotube length is controlled by the formation of the

TiO_2 at the metal bottom and the dissolution of the as-formed TiO_2 top tip in the HF electrolyte [10]. Short nanotube length means a high solution rate of TiO_2 in the fluoride acid. The TiO_2 dissolve rate can slow down by carefully controlling the PH value and getting a length up to micron scale. In Macak et al's work, they obtaind a tube length approximately 2.5 μm [11].

3.1.1.2 Anodization under neutral electrolytes

Nanotubes's length with only hundreds of nanometers greatly confines their further applications. As a good photo-electric response material, the length in some occasions needs to be over than 10 μm. To increase the nanotube length and aspect ratio, anodizaition in the neutral electrolyte has been developed. Instead of aqueous acid solution, neutral solutions, such as glycerol,[12, 13] ethylene,[14, 15] have been used, and NH_4F was added instead of HF. These kinds of neutral electrolytes have high viscosity, as a result greatly slow down the dissolving rate of the TiO_2 nanotube tips. Under this condition, TiO_2 nanotube length > 100 μm [16, 17] have been successfully synthesized with very large aspect ratio. Research has tried to apply this long length TiO_2 nanotube to the water photo-catalysis and dye-sensitized solar cell [17]. It is very interesting that the TiO_2 nanotubes generated in the neutral electrolytes have very smooth walls along the whole tube [18]. Anodization carried out in the neutral electrolyte can tolerate a large range of applied voltage variations. By alternating a sequence of 120 V and 40 V applied voltage, a bamboo-shaped nanotube arrays was obtained [19]. Researchers are continuously optimizing the component of the neutral electrolyte, like the

influence of the water content on the anodic TiO_2 morphology [20]. The water content can influence the nanotube density and tube wall formation.

3.1.2 Application of TiO_2 nanotubes

TiO_2 is more chemically stable than Al_2O_3. It will not react with a lot of acids, even strong acids such as HCl and HNO_3. It can endure a high temperature. Moreover, TiO_2 has interesting photo-induced properties, which results in its application in multiple areas.

Except for a large geometric surface area, TiO_2 nanotubes have been reported to enhance electron collection and transfer along the orientated tubes in dye-sensitized solar cells.[21, 22] TiO_2 nanotube layers perform a very high quality electrochromic property with fast switching speed.[23, 24] The Ag particle modified TiO_2 nanotubes array shows a significantly improved photochromic performance [25]. Better ion diffusion through the nanotube hole may be one important reason. As described above, TiO_2 has strong photo-induced hydrophilic/hydrophobic property. TiO_2 nanotubes give more variables for wettability control, as a result lead to super-hydrophilic/hydrophobic surface.[4, 26] For porous AAO, researchers have found some methods to open the bottom end of the pores, so that liquid, air can flour through the membrane [27]. Uniform sized nano-porous membrane can act as particle filter. A free-standing TiO_2 nanotube layer can also be prepared by opening the close end of the nanotubes. The photo-catalytic character of TiO_2 has widened the application of this free-standing porous membrane. For a practical example, the methylene blue in the solution can be totally decomposed when it goes

through the UV light explored TiO_2 nanotube membrane [1]. Compared to nanoparticles, TiO_2 nanotube shows better photocatalytic activity [2], and this performance will enhance a lot when depositing noble metals (Ag or Au) onto the tube walls [28], or introducing external electrical bias [29]. As we know, TiO_2 is biocompatible. By investigating the interaction between the TiO_2 nanotube layers and living cells, it has been discovered that some stem cell shows differences in adhesion, spreading, and growth [30]. Carefully develop the TiO_2 based bio-technics may lead to novel application in our daily life in a desired manner.

To sum up, the TiO_2 nanotube has exhibited its practical value in a wide area, and has shown a brilliant future.

3.1.3 Ordered titania nanotubes

Once again, if an application just bases on the large surface area, we do not need an ordered structure. However in some occasions, an ordered structure may give other interesting property. For the light absorption of highly ordered TiO_2 membrane under visible light, simulation work indicates that longer nanotubes have better absorption when the light wavelength is between 380 nm and 435 nm. For those that propagate through the nanotube arrays with a wavelength between 435 nm and 600 nm, decrease the tube diameter will significantly increase the light absorption [31]. Of course, ordered structure can avoid the influence of local effects.

Compared to ordered AAO template, highly ordered anodic TiO_2 nanotubes are less reported. Researcher has not developed any direct “guiding” method to make ordered

TiO_2 nanotube. The chemically stable nature of Ti may be one reason. The formation of highly ordered anodic porous alumina benefits from a nearly "perfect" surface before anodization. The Al foil can be annealed to remove the mechanical stress and electropolished in a perchloric acid and ethanol mixture to obtain a surface roughness less than 1 nm [32]. In comparison, most of the published studies on TiO_2 nanotubes use commercial Ti foils directly and have not addressed the effect of the surface roughness on anodization. Surface conditions and their influence on the formation of nanotubular TiO_2 structures have been reported [33]. However, Ti surface roughness was not quantified.

One method that has been chosen is to make use of the material's inherent nature. When anodizing for quite a long time under very stable applied voltage, due to the self-organization of the electrical field, the nanopore/nanotube trend to approach a hexagonal arrangement. This phenomenon has been observed in both AAO and anodic TiO_2. Researchers have developed a second time anodization method. After a long time anodization, the first layer is peeled off from the substrate, leaving relatively ordered concaves. During the second anodization under the same condition, these concaves act as the seeds that guiding the following pore/tube formation. This method is called secondary anodization [34]. However, the electrical self-organization process is very slow. Sometimes, we need to repeat several times to get an acceptable result.

The disadvantages of this indirect "guiding" effect are evident. It is time consuming; needs a very stable power source; more important, it cannot overcome the influences of the defects and dislocations.

3.2 Experimental section

Anodic TiO_2 was generated on 100 μm thick and 99.99% pure Ti foils (Goodfellow Corporation, Oakdale, PA). The Ti foil was first cut to 1.6 cm × 0.2 cm in size and then cleaned successively in acetone, isopropanol, and methanol for 5 minutes each.

The chemical polishing electrolyte was composed of 40 wt% hydrofluoric acid, hydrogen peroxide, and deionized water with a volume ratio of 1:6:3. The cleaned Ti foil was immersed into the electrolyte for 1 minute at room temperature.

Mechanical polishing was carried out on a grinding polisher using micron sized diamond/oil mixture (Leco Corporation, MI) as the polishing agent. The mechanical polishing was first done at 3 μm for about 40 minutes, then at 0.5 μm for roughly an hour, and finally at 0.1 μm for about 2 hours to obtain a uniform mirror surface. The polishing times varied depending on different initial Ti surface conditions.

For electropolishing polishing, the electrolyte was composed of glacial acid and perchloric acid with a volume ratio of 9:1. The electropolishing of the titanium foils was performed in a two-electrode configuration. The Ti foil was used as the anode and the platinum mesh was used as the counter electrode. The electropolishing was conducted at 40 V constant voltage at 5 °C for 1 minute using a DC power source.

The anodization was carried out in the same two-electrode configuration at 0 °C in a 0.1 M NH_4F ethylene glycol solution (10 vol% DI water) at 100 V for 10 mins.

The surface morphologies of the anodized samples were evaluated using a scanning electron microscope (SEM, Quanta 600 FEG, FEI Company, Hillsboro, OR).

The surface roughness was measured by an atomic force microscope (AFM, Veeco metrology group, MA, USA). The AFM measurement area was 10 μm × 10 μm.

3.3 Results and discussion

3.3.1 Polishing effect

3.3.1.1 Different polishing conditions

Figure 3-1 shows Ti foil surfaces at different polishing conditions. The as-received Ti sample (Figure 3-1(a)) has rough tracks with small cracks randomly distributed on the surface. The surface height varies widely in different regions. AFM measurement (Figure 3-1(b)) shows that the roughness is 46.3 nm. After the chemical polishing in a HF/H_2O_2 mixture for 1 minute (Figure 3-1(b)), the surface morphology improves drastically and shows a reticulated texture "divided" into small regions from less than one micron to several microns in size. Although the AFM measurement indicates that chemical polishing can smooth each local region and get rid of the rough tracks and cracks on the Ti surface, the surface height variation actually increases and the roughness is 69.3 nm. The boundaries between the local regions are the highest points on the surface. It is highly possible that the Ti surface consists of Ti grains in different crystallographic orientations. The differences of chemical etching rates on differently orientated Ti grains cause the textured surface. Still, the large surface height variation is surprising and could imply some uneven chemical attack. Mechanical polishing, on the other hand, creates a flat surface, even though tiny shallow scratches are found on the surface (Figure 3-1(c)).

The average surface roughness is 7.9 nm. The eletropolished Ti surface (Figure 3-1(d)) shows a very uniform surface with a surface roughness at 5.3 nm.

Figure 3-1(e) illustrates the surface height variations along the white lines shown in the AFM images from the bottom left to the top right for the samples polished at individual conditions. The as-received sample has random and large height variation. The chemically polished sample has smooth height transitions for each local region but the height variation is still large. The mechanically polished sample has much smaller surface roughness. The electropolished sample has the most uniform surface with small surface roughness. Overall, mechanically polished and electropolished sample surfaces have the most desirable surface morphologies for anodization.

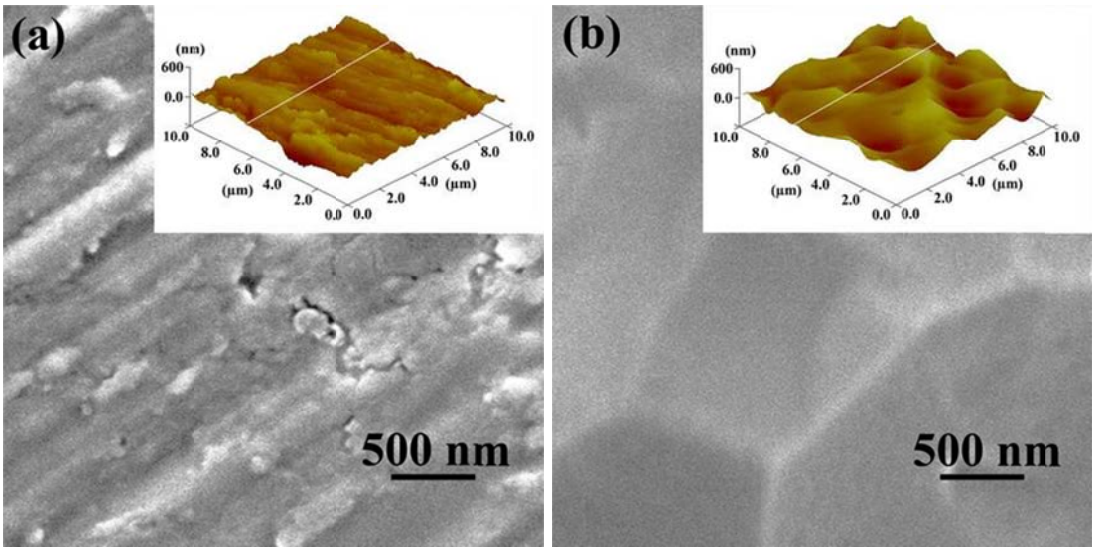

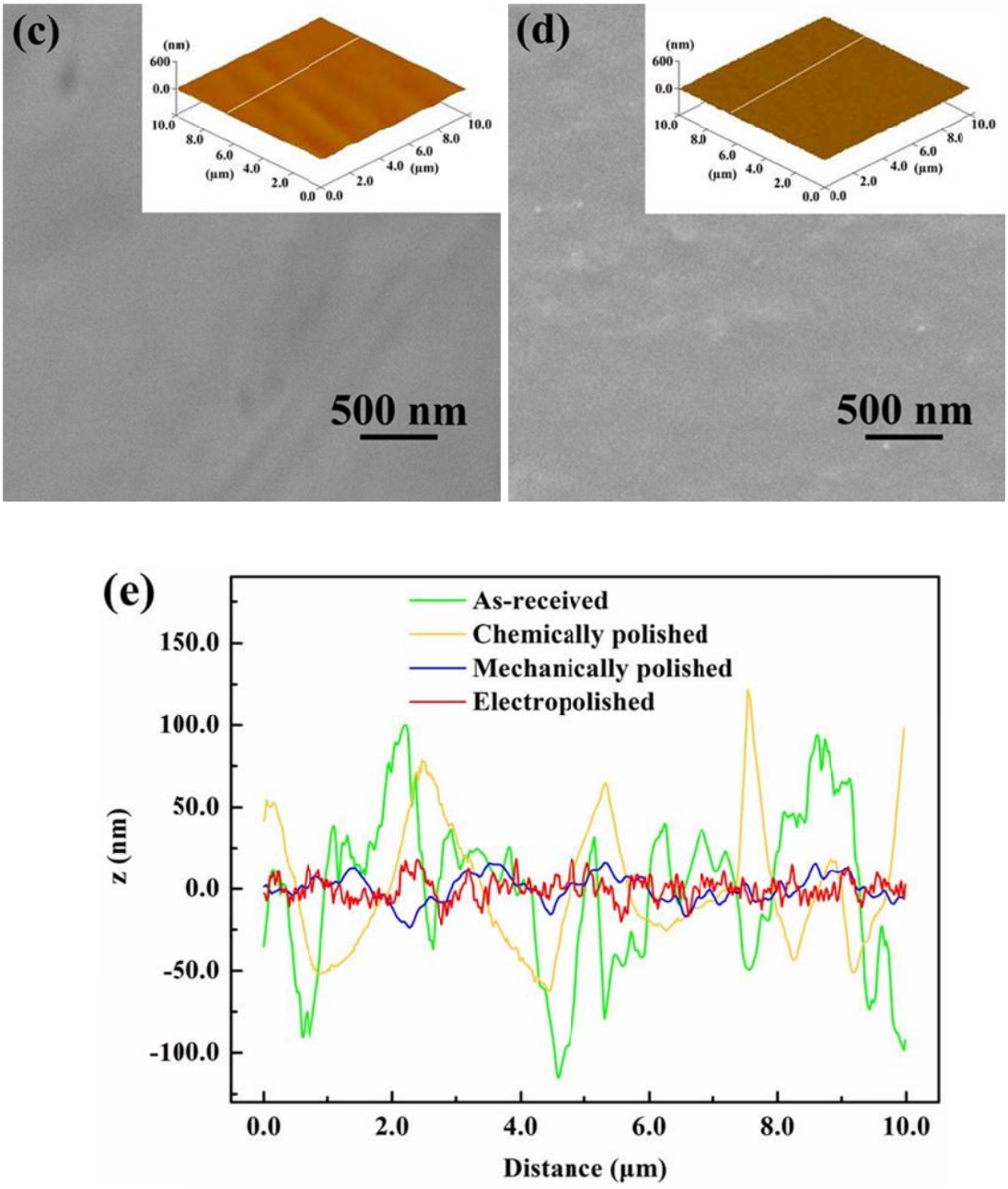

Figure 3-1 SEM and AFM images of Ti samples at different polishing conditions. (a) as-received, (b) chemically polished, (c) mechanically polished, (d) electropolished, (e) surface height variations across the surfaces.

3.3.1.2 Polishing effect on anodization

Figures 3-2 shows the surface morphologies of anodized Ti foils with respect to the four polishing conditions described above, respectively. The as-received Ti foil (Figure 3-2(a)) shows non-uniform nanotube formation after the anodization. The surface is made up of regions varying in height. Patches of oxidized layers cover the TiO_2 nanotubes. The nanotube outer diameter is ~130 nm and the inter-tube distance is ~200 nm. The wall thickness is ~35 nm.

The chemically polished Ti surface (Figure 3-2(b)) still shows a textured surface with sloped grains similar to those of the original chemically polished surface. Surprisingly, no nanotubes but nano-pores appear on the surface. The pore size and the inter-pore distance are not uniform. To further identify the microstructure beneath the surface, the cross-section of the same sample is shown as an insert in Figure 3-2(b). TiO_2 nanotubes clearly grow under the oxidized surface layer. The top oxide layer is ~200 nm thick. The inner tube diameter is ~ 65 nm. Wall thickness is ~ 90 nm. The inter-tube distance is ~245 nm.

The mechanically polished Ti foil exhibits a flat surface and uniform TiO_2 nanotubes form after the anodization. The tubes are randomly arranged and their shapes are not perfectly round. The inner tube diameter is ~50 nm and the inter-tube distance is ~100 nm. The wall thickness is ~25 nm. Compared to Figure 3-2(a), both the tube diameter and the inter-tube distance are reduced by ~40%.

Figure 3-2(d) shows the anodization result of the electropolished Ti sample. Similar to Figure 3-2(b), a thin porous layer remains on the top of the TiO_2 nanotubes. Before this

thin oxide layer is removed, it is difficult to identify the nanotube structure. A similar phenomenon was reported before [34], but the underneath structure was not reported. When the surface oxide layer is broken, the nanotubes are revealed. These tubes are more spherical and have thicker walls than those of the mechanically polished sample. The inner tube diameter is ~70 nm, the wall thickness is ~ 50 nm, and the inter-tube distance is about 210 nm. Among the nanotubes, there are missing, small local regions.

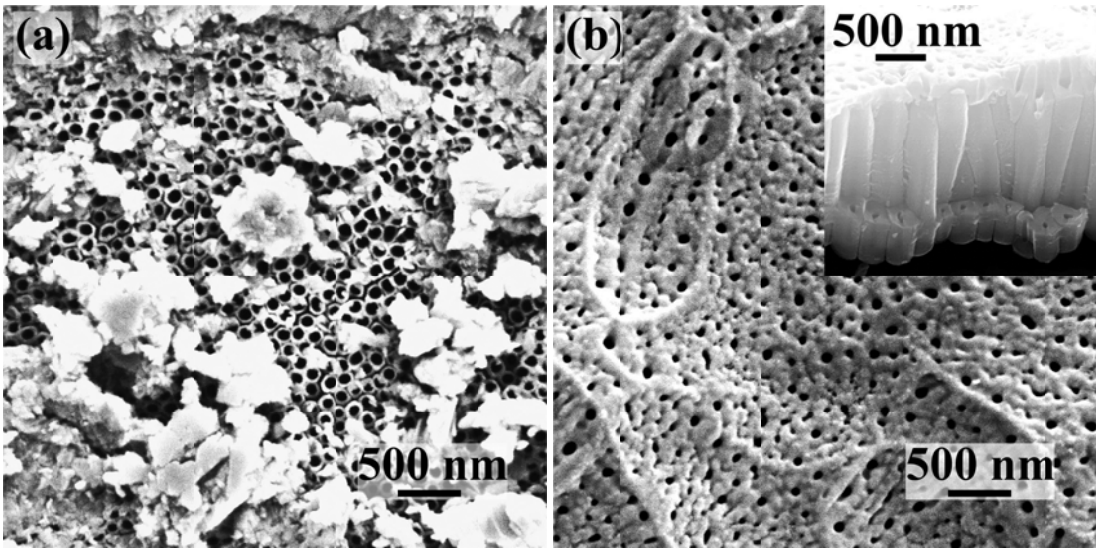

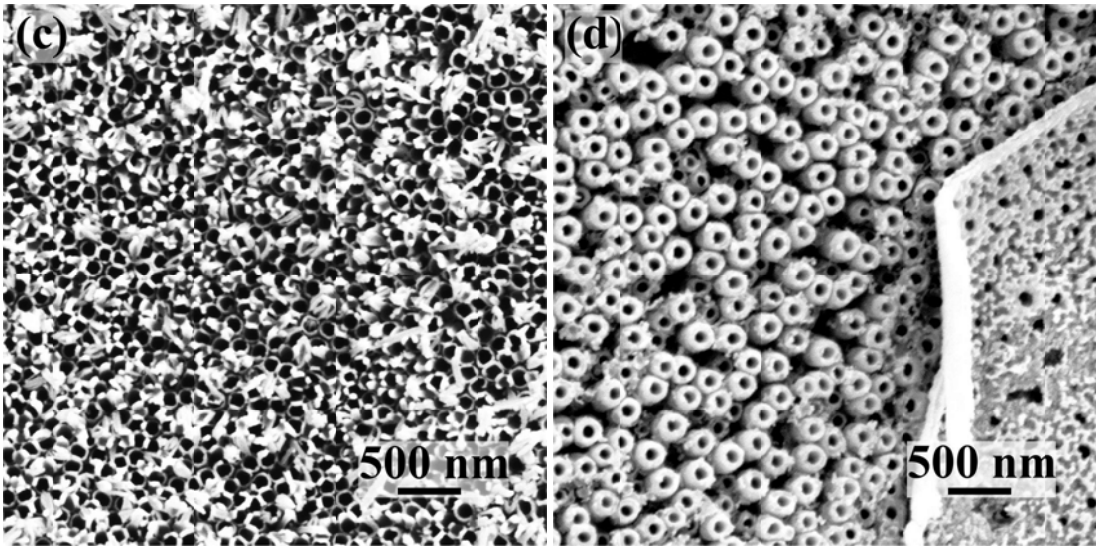

Figure 3-2 Anodized Ti foil surfaces with different polishing conditions. (a) as-received, (b) chemically polished, (c) mechanically polished, and (d) electropolished.

3.3.1.3 Mechanism

To understand the surface morphology effect on the TiO_2 nanotube formation and growth, the current density vs. anodization time curves for each surface condition are obtained as shown in Figure 3-3. All the samples have very similar current density vs. anodization time trends even though the magnitudes and transition points vary widely. All the polished samples possess a relatively large current density at the beginning of the anodization. The initial current densities are 158 mA/cm^2 for the as-received sample, 14.8 mA/cm^2 for the chemically polished sample, 250 mA/cm^2 for the mechanically polished sample, and 31 mA/cm^2 for the electropolished sample. The large initial current density reflects the surface oxidization process. During this process, a surface oxide layer forms and nanotubes start to initiate and grow. Hydrogen gas will generate under the reaction:

$$Ti+2H_2O \rightarrow TiO_2+2H_2 \uparrow \qquad (1)$$

Gas generation was observed at the beginning of the anodization. In this step, the current density is high. As the anodization going on, the gas generation slows down and finally stops. In the following anodization, TiO_2 nanotube continues to develop. Ti and O ions diffuse through the electrolyte/substrate interface under the electrical field and form oxide barrier layer around the nanotubes under the reaction:

$$Ti^{4+}+4OH^- \rightarrow TiO_2+2H_2O \qquad (2)$$

As the same time, the TiO_2 barrier layer graduate dissolve in the electrolyte by reacting with F^-, forming $[TiF_6]^{2-}$:

$$TiO_2+6F^-+4H^+ \rightarrow [TiF_6]^{2-}+2H_2O \qquad (3)$$

The growth and dissolve of the oxide layer reach a balance for stable anodization. At a certain point, when the voltage drop in the horizontal oxide layer direction becomes equal to the applied voltage, the oxide layer growth stops. Moreover, when the nanotube walls contact with each other, they will also stop growing in the horizontal direction. However, at the nanotube bottom, reaction (2) and (3) will process continuously, so that the nanotube will grow deep into the Ti substrate in the vertical direction for long time anodization. When the nanotube walls fully develop, the current densities drop quickly and stay at a much lower constant value, which mainly reprresents the stable anodization carrying out at the nanotube bottom. The stable current densities for the samples are ~17 mA/cm^2, ~10.5 mA/cm^2, ~5 mA/cm^2, and ~6.5 mA/cm^2 for the as-received sample, the chemically polished sample, the mechanically polished sample, and the electropolished

sample, respectively, which reflects the stable anodization conditions needed for the vertical nanotube growth. For the horizontal direction, the pore size and arrangements are believed to be balanced, and no tube size or morphology change is expected. At the tube bottom, the oxide layer continues to dissolve. Nanotubes only grow vertically. This explains why all the polished samples have nearly the same current density at the steady state. For the as-received sample, the current density continuously decreases during the entire anodization process. This is likely because the random oxide layer patches influence the electrical field distribution during the anodization. The TiO_2 nanotubes do not distribute uniformly across the surface and the Ti underneath the oxide patches anodizes continuously. In this case, the current density trends to decrease with the anodization time and a stable anodization state might request extra time to establish.

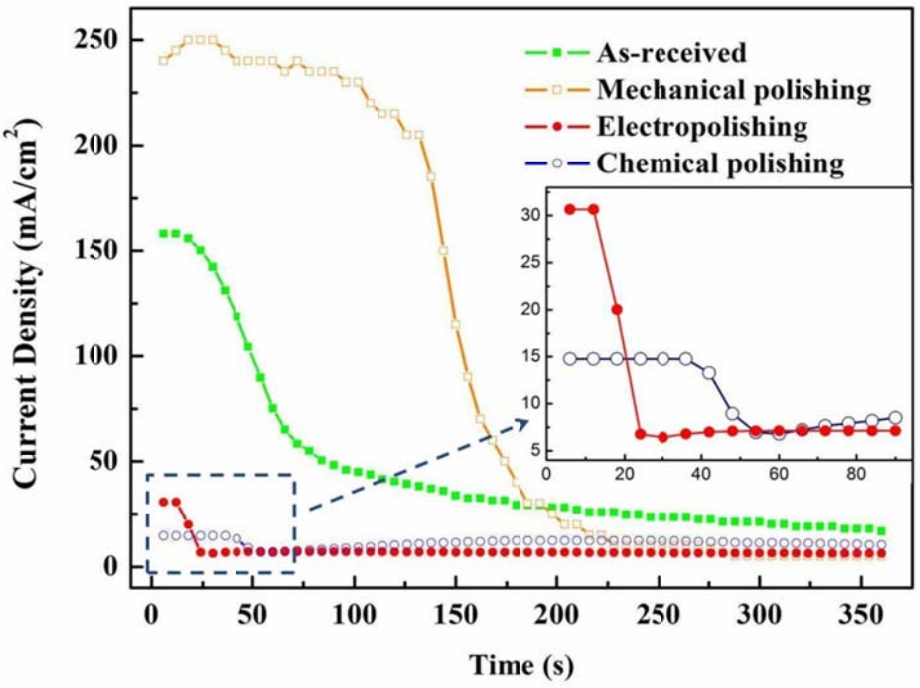

Figure 3-3 Current density vs. anodization time for four Ti surface conditions: as-received, mechanically polished, chemically polished, and electropolished.

The differences in the initial current densities match with those of the morphologies of the TiO_2 nanotubes. While the tube inner diameter and the inter-tube distance don't show obvious trends, the top oxide layer and nanotube wall thickness are two major differences. For the mechanically polished sample, the top oxide layer is removed and the nanotube wall is the thinnest, ~ 25 nm. This corresponds to the largest initial current density. For the as-received samples, the Ti foil surface has patched oxide layers. The nanotube wall thickness is 35 nm after the anodization. For the chemically polished and electropolished samples, the surfaces retain the top oxide layer and the TiO_2 nanotube walls are thicker: 90 nm and 50 nm, respectively. The initial current density is lowest.

Based on the data, the tube wall thickness decreases exponentially with the initial current density increase. The exponent is ~0.4. These differences can be explained as follows. During the anodization, the oxide layer forms at the very beginning. A smaller current density induces a slower rate of TiO_2 formation and dissolution. The oxide layer cannot be effectively removed because of the slow ion exchange and transport. Based on the results, it seems that the absence of the surface layer (mechanically polished followed by as-received, electropolished, and chemically polished) is the leading factor for nanotube formation and growth. This leads to thicker TiO_2 nanotube walls. However, the current densities and the tube wall thickness don't correlate with the surface roughness. After the applied voltage is balanced by the voltage across the oxide layer, nanotube diametric growth stops and similar tube inner diameter results while the inter-tube distances are different.

To further investigate the influence of the surface roughness on the TiO_2 growth, especially for the tube bottom barrier layer, a layer of anodic nanotubes was peeled off from the Ti substrate for the as-received sample (Figure 3-4(a)), chemically polished sample (Figure 3-4(b)), mechanically polished sample (Figure 3-4(c)), and electropolished sample (Figure 3-4(d)). As seen in Figure 3-1, both as-received and chemically polished samples have uneven, mildly modulated surface textures. The curved bottom barrier layer (Figures 3-4(a) and 3-4(b)) in different local regions reflects this. The mechanically polished and electropolished samples have flat surfaces to start with and the bottom barrier layers after the anodization (Figures 3-4(c)) and 3-4(d)) are also flat.

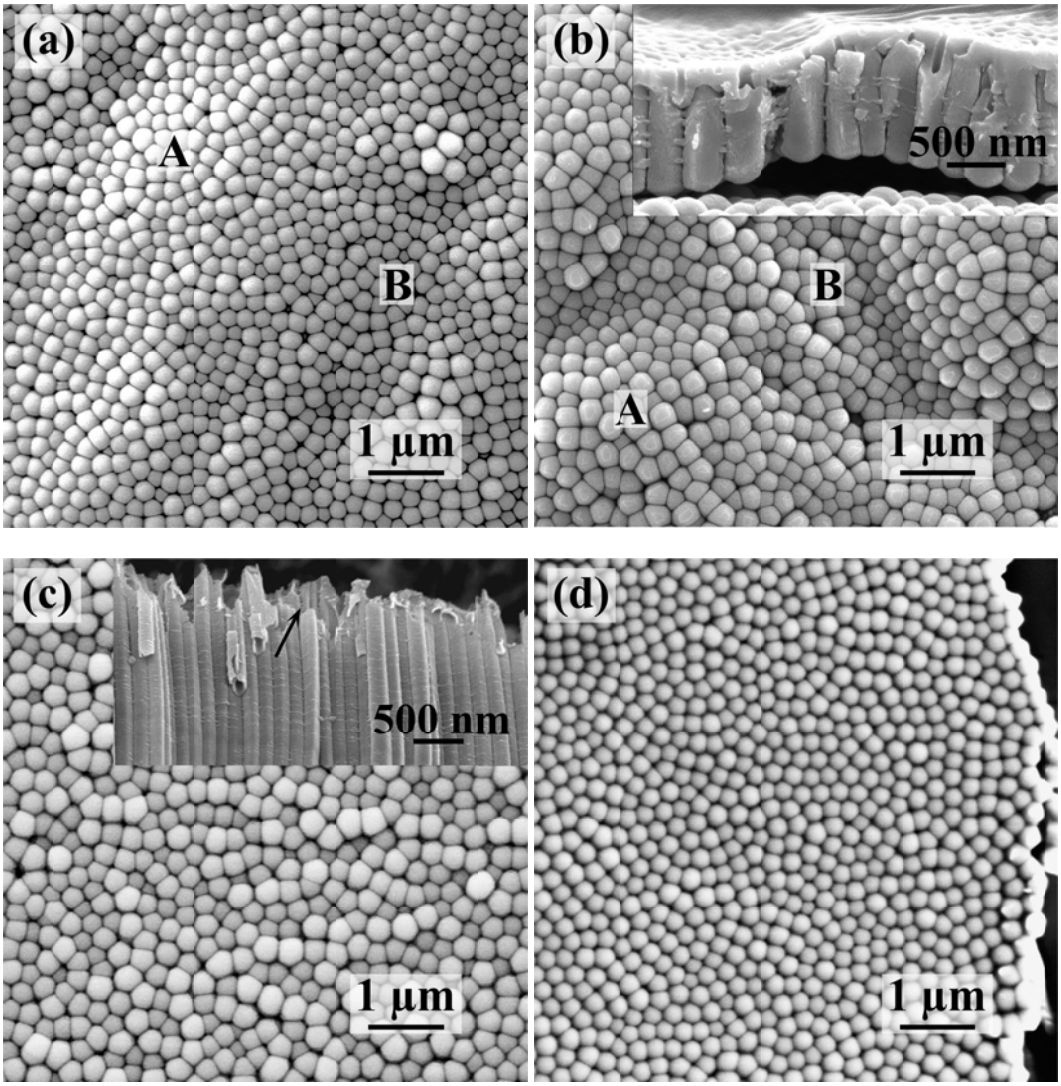

Figure 3-4 Bottom barrier layers of different polished samples and sketch of TiO_2 nanotube formation for an uneven surface: (a) chemically polished, (b) mechanically polished, (c) electropolished, and (d) nanotube formation on a curved surface.

Figure 3-5 sketches the formation process of the bottom layer for the uneven surfaces. The arrows in Figure 3-4(d) indicate the electrical field direction. At the beginning of the anodization, the electrical field is perpendicular to the Ti metal surface and the nanotubes

grow along the electrical field direction. Since the ion transfer is mainly along the voltage drop direction, the electrical field has a major effect on the nanotube growth direction. When the Ti foil surface is locally tilted, the electrical field also tilts locally. This subsequently influences the ion migration and thus nanotube growth direction to tilt in the same direction. Similar phenomenon has been reported for anodic porous alumina [35]. The initial tube formation guides the subsequent growth of the nanotubes. In this case, a curved bottom barrier layer reflects a curved top surface and tilted tube growth.

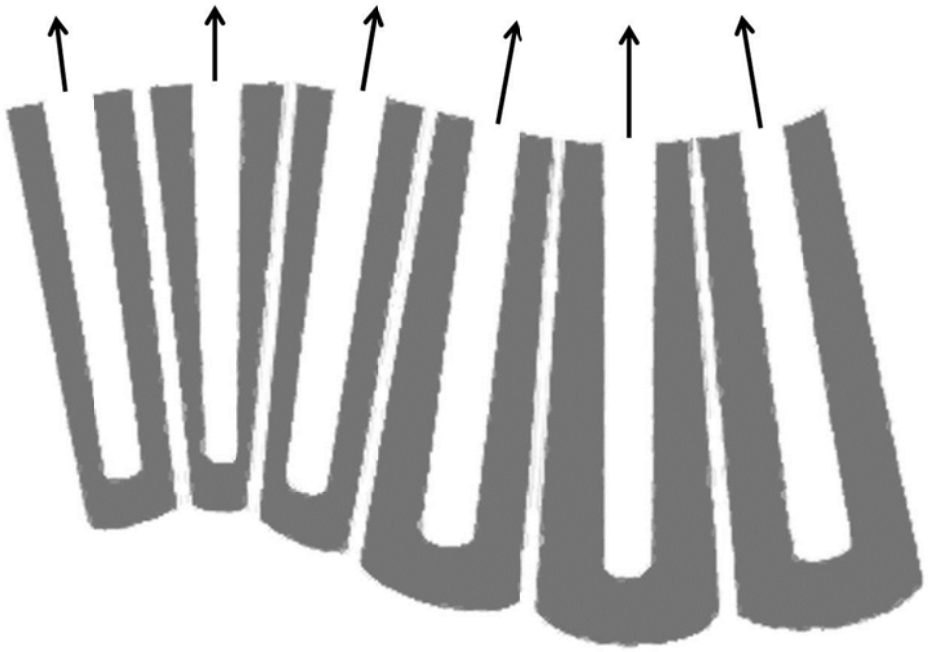

Figure 3-5 Nanotubes grow from curved surface.

The curved initial Ti surfaces also influence the barrier layer size at each tube bottom, which also represents the corresponding nanotube size. In Figures 3-4(a) and 3-4(b), region A has larger sized nanotube bottom barrier layer while region B has smaller

sized nanotube bottom barrier layer. Tracking back to the nanotube top surface, region A should be concave and region B should be convex. The Figure 3-4(b) insert is the cross-section of the anodized nanotubes started from curved chemically polished Ti surface. It is clear that the nanotubes generated from the concave regions have a little larger nanotube bottom size. This means a concave surface is beneficial for large nanotube size formation. Figure 3-5 also sketches the barrier layer constraining effect. As schematically shown in Figure 3-5, the nanotubes generated from the concave area grow deeper than those form the convex area. The barrier layer of the deeper nanotubes confines the growth of the shallower nanotubes. Figures 3-4(c) and 3-4(d) show the flat nanotube bottom surfaces from the mechanical polishing and electropolishing conditions. The nanotube sizes in Figure 3-4(c) vary from ~200 nm to ~300 nm. Figure 3-4(d) shows more uniform nanotube size distribution at ~ 250 nm.

One interesting phenomena is shown for the mechanically polished sample Figure 3-4(c). The size of the bottom barrier layer is larger than that of the top nanotube. The bottom barrier layer size varies from 200 nm to 300 nm, while the top outer nanotube diameter is only ~100 nm. That means that not all the nanotubes appear on the top surface can fully develop. The insert in Figure 3-4(c) indicates that after anodizing for around 500 nm deep, the narrow sized nanotubes (point out by an arrow) become wide and keep this size grow into the substrate. This phenomena may be similar to the anodic porous alumina, at a given applied voltage, the interpore distance is 2.5 nm/V [36], which is determined by the material intrinsic characteristic. The anodic TiO_2 nanotube may have similar property. Even though the initial nanotubes have small tube size, the stable anodization will grow at a larger nanotube size. However, the nanotube widen

mechanism is still unclear. It can be a random process deduced from the bottom the uneven nanotube size distribution.

To sum up this part, as-received and chemically polished samples do not have uniform nanotube size due to their curved surface. Mechanically polished sample does not have even nanotube size because the differences between nanotube initiation and stable anodization. Only electropolished sample has better nanotube size distribution.

3.3.2 FIB guided anodization

The polishing effects on the anodic morphologies are discussed in the above section. A desired smooth surface is obtained via electropolishing. In this part, FIB guided anodization is applied to the electropolished Ti sample, so as to investigate the guiding effect of the anodic TiO_2 and to create ordered nanotube arrays.

3.3.2.1 FIB guiding patterns

Figures 3-6 shows the FIB patterns in different interpore distances: (a) 200 nm, (b) 250 nm, (c) 300 nm, and (d) 350 nm, respectively. The morphologies are similar to the FIB patterned pores on the Al surface, white rings appear around each pores, a result of Al amorphization and the implantation of the high atomic number Ga^+. Though the surface roughness is lower than 6 nm, we can still see many shallow concaves on the Ti surface. There is no such pattern on the well electropolished Al surface (roughness < 1nm).

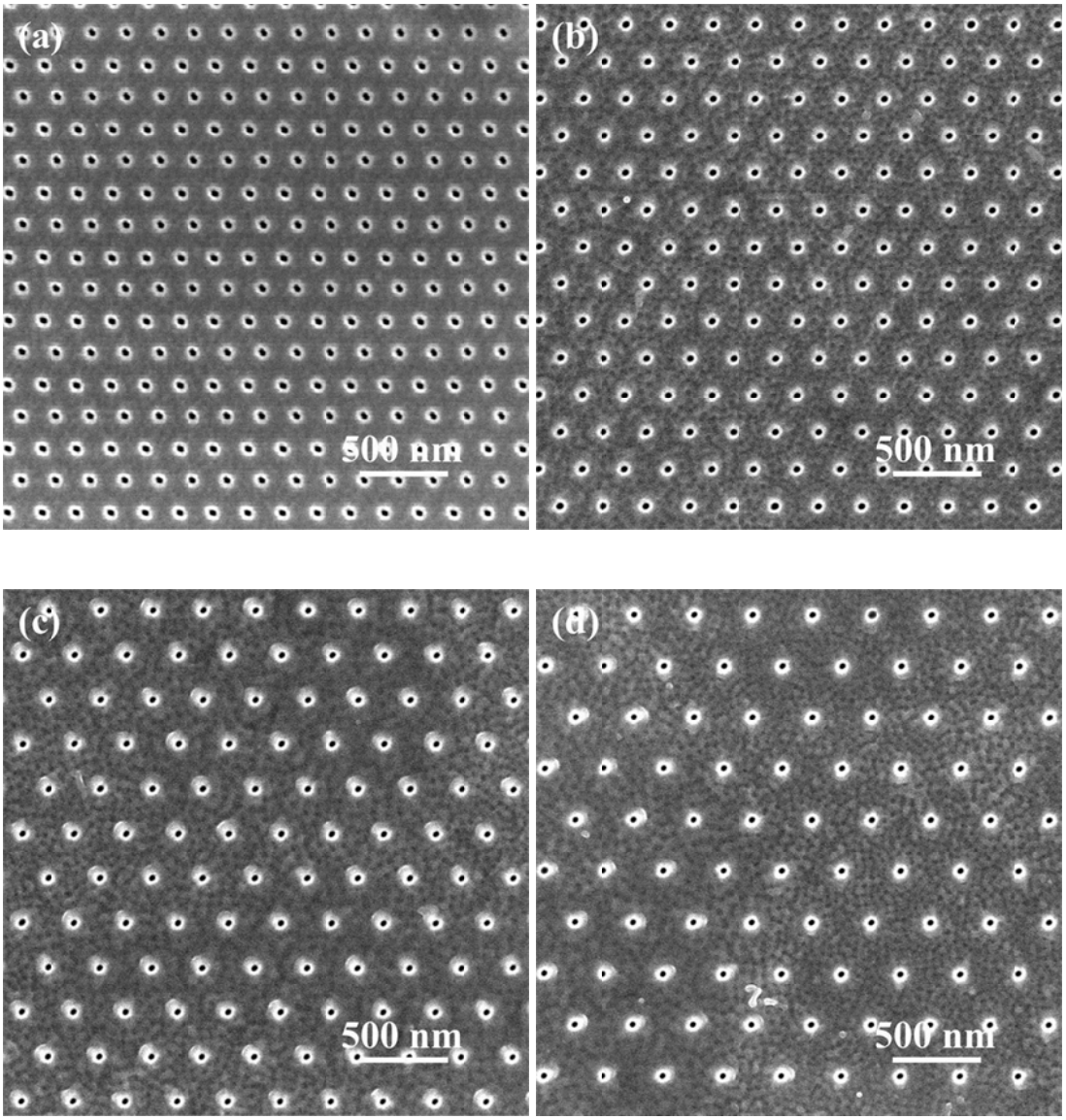

Figure 3-6 FIB guiding patterns with different interpore distance before anodization. (a) 200 nm, (b) 250 nm, (c) 300 nm, and (d) 350 nm.

3.3.2.2 Anodic titania under FIB guiding

Figures 3-7 (a) - (d) show the anodized TiO_2 surface according to the guiding patterns of Figures 3-6 (a) - (d), respectively. All the FIB guided pores have further

generated into the Ti foil. The original patterns are kept. Clear differences appear on the surface. At small guiding pore distances (200 nm and 250 nm, Figures 3-7 (a) and (b)), no other pores clearly generate on the surface, which means the existing guiding pores develop fast, and all surface room is taken up by them that no new pores can generate any more. When the guiding pore distance increases to 300 nm (Figure 3-7 (c)), some shallow pores tend to develop. Those shallow pores have random locations, and their depth is not deep. When the guiding pore distance increases to 350 nm (Figure 3-7 (d)), new pores generate, and distribute randomly on the patterned surface. It is highly possible that the formation mechanism of those new pores is quite different from that is for the porous AAO, so that the new pores' locations cannot be predicted.

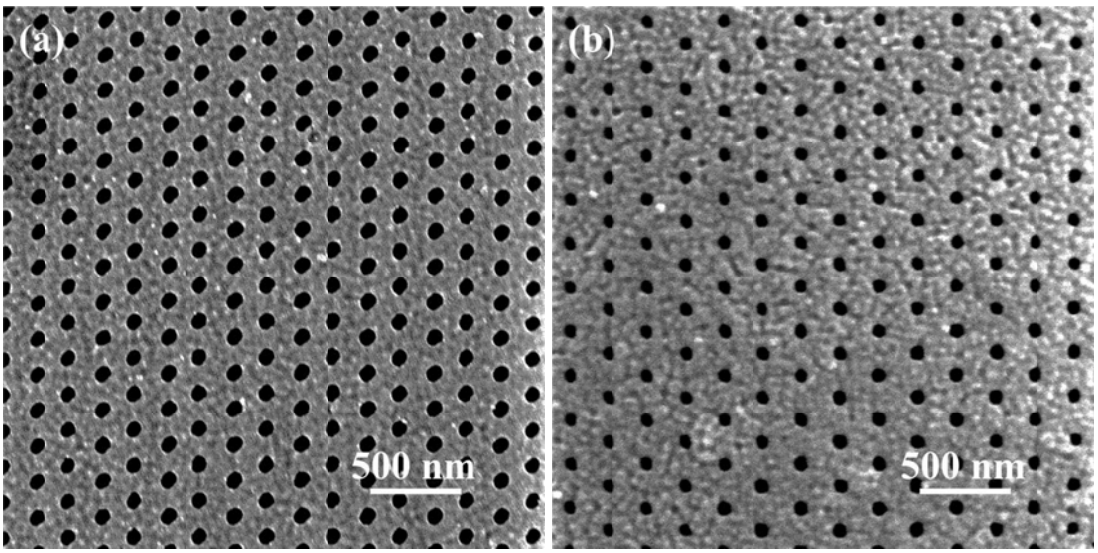

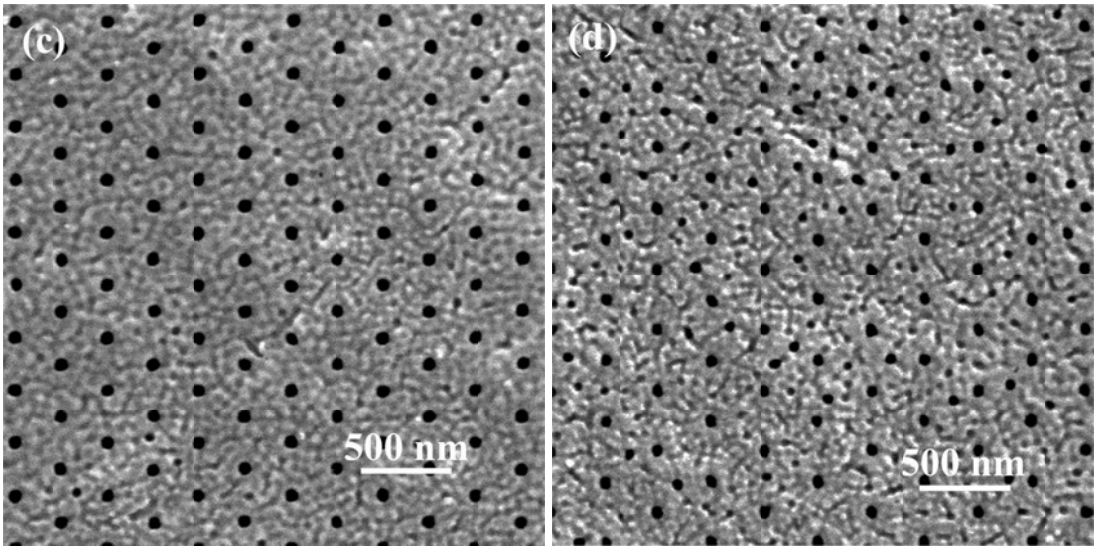

Figure 3-7 Anodic TiO_2 surface under FIB guiding effect. The guiding patterns have different interpore distances: (a) 200 nm, (b) 250 nm, (c) 300 nm, and (d) 350 nm.

3.3.2.3 Structure identification

Similar to Figures 3-2 (b) and (d), it is impossible to say that nanotubes are generated from the top SEM images. To better understand the structure, a corrosive gas XeF_2 which is equipped in FIB is applied to etch on the anodic surface, aiming to get rid of the top layer. Etching result is shown as Figure 3-8. After etching off a thin layer of TiO_2, ~ 100 nm thick, the guiding pattern still maintains. At this depth, it is still a porous structure.

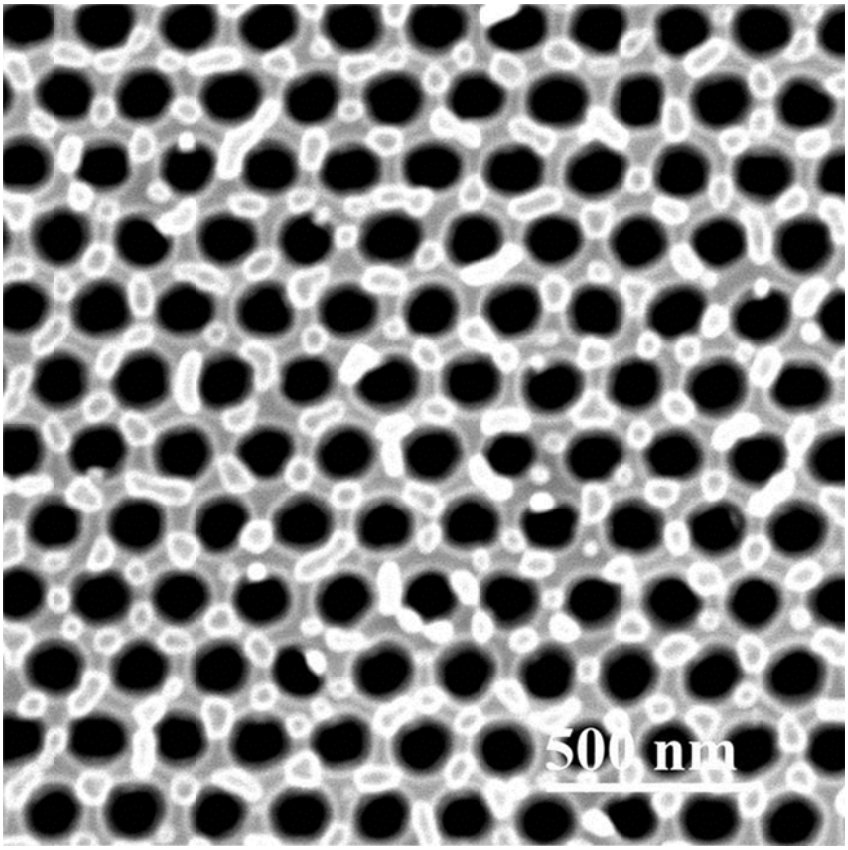

Figure 3-8 Anodized guiding pattern is etched by XeF_2. The interpore distance is 200 nm.

To further investigate the structure along the "pores", a cross-section is made by FIB cutting inside the substrate (Figure 3-9). The cross-section is a layered structure. On top is a condensed layer, similar to Figures 3-2 (b) and (d). Below the condensed layer, tubular structure starts to appear. The arrow points out the line that two nanotubes distinguish from each other. In contrast, if they are pores, no clear lines will appear in between the two pores (Figure 2-16 (b)). More importantly, the nanotubes will grow straightly into the substrate over than 2 μm; and the inter-tube distance is the same as FIB pre-designed pattern, which means this guiding pattern can further develop during the

anodization and create ordered arrays. However, other problems need to be addressed. The formation and the function of the condensed top layer are still unclear. The ultimate structure of the TiO_2 nanotube is difficult to predict.

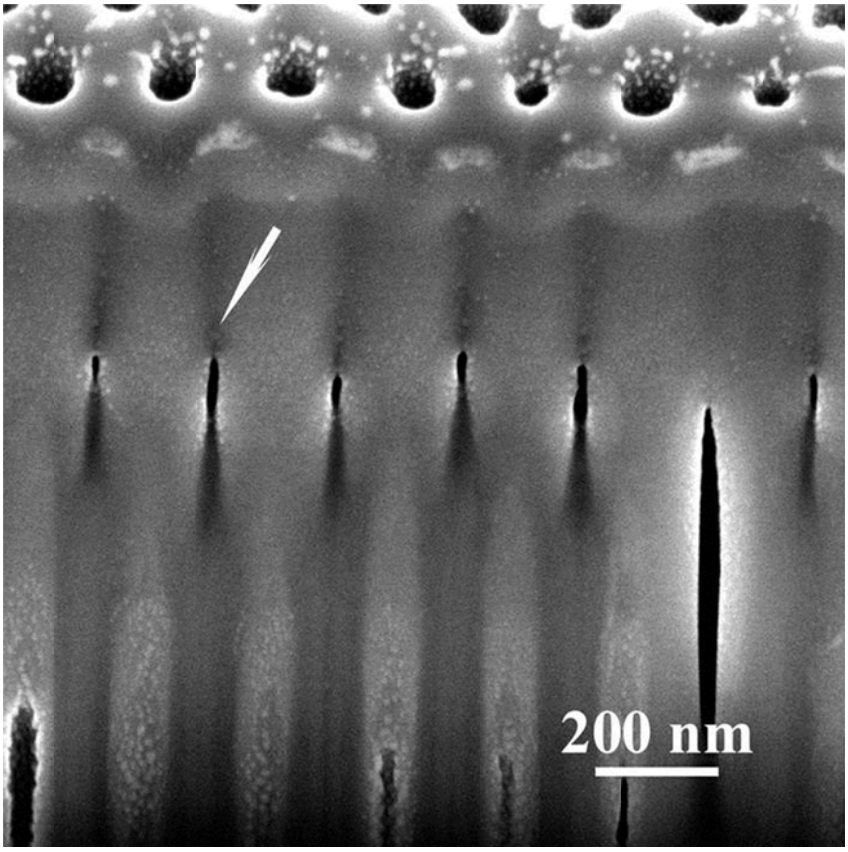

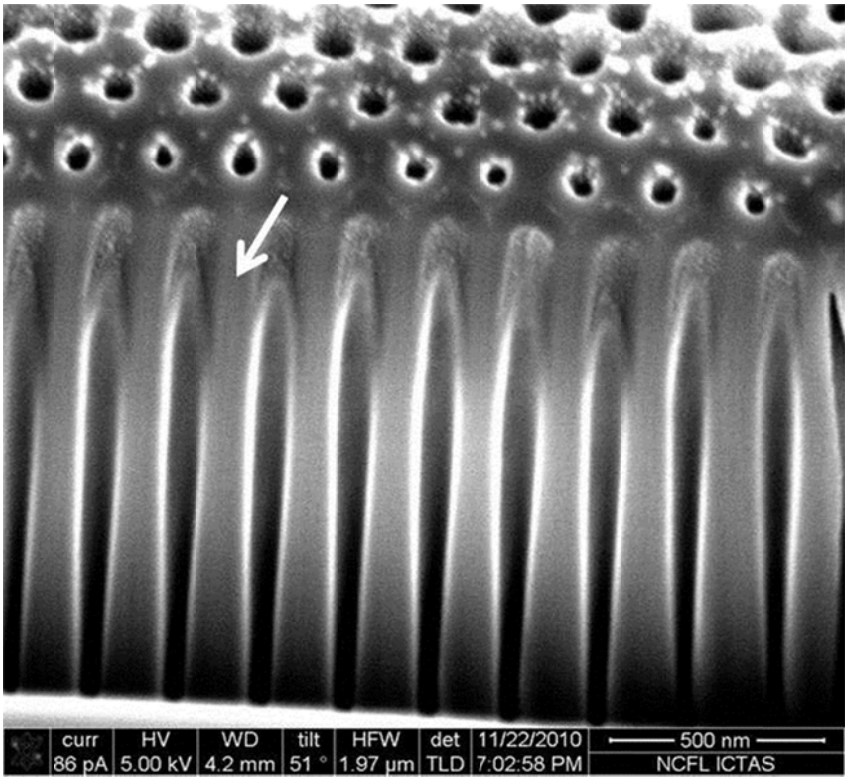

Figure 3-9 Cross-section of the developed FIB guided pattern with 200 nm interpore distance.

Due to the above observation, a deep XeF_2 etching is carried out. Figure 3-10 shows the etching depth ~ 1 µm inside the guided pattern. In this depth, the top oxide layer should disappear. It shows clearly an ordered hexagonal arrangement and nanotube boundaries.

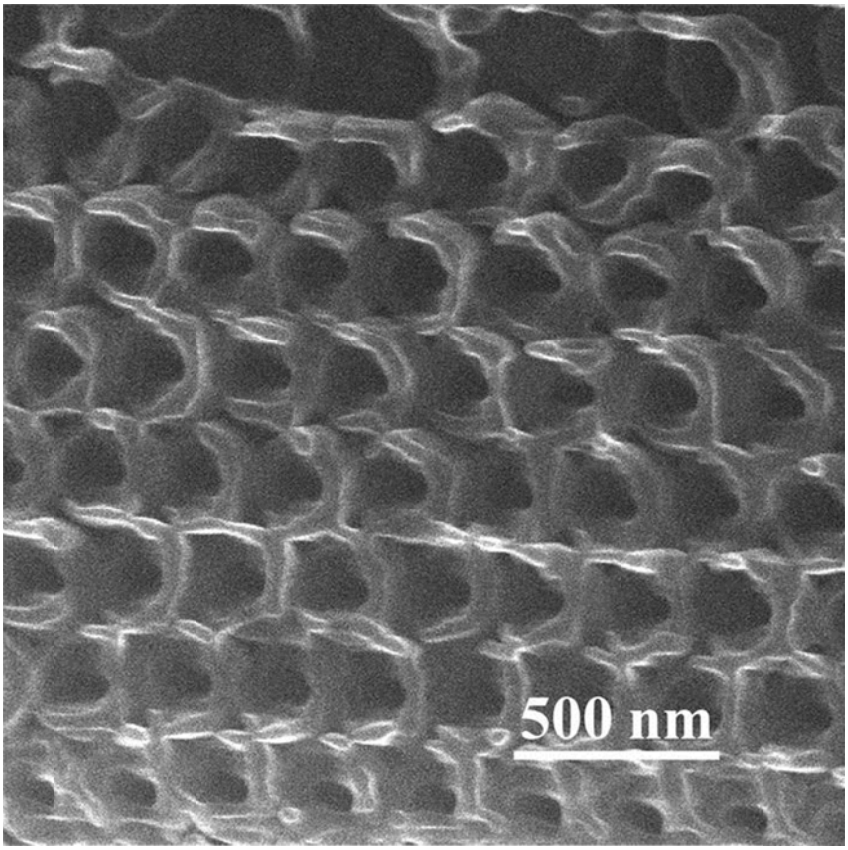

Figure 3-10 XeF_2 deep etching of the anodic FIB guided pattern.

3.3.2.2 Guided anodization for sophisticated patterns

It is known that traditional anodization without any modification will only create hexagonal arranged nanotube. Here square patterns with different interpore distances were created by FIB in order to reveal the guiding effect. Figure 3-11 shows the anodic TiO_2 with the guiding interpore differences at (a) 150 nm, (b) 200 nm, (c) 250 nm, (d) 300 nm. It can be seen that the anodized results are also related to the interpore distance. At small guiding interpore distances (150nm Figure 3-11(a) and 200 nm Figure 3-11(b)), the guided patterns maintain well and no new pores are observed on the Ti surface. At

larger guiding interpore distance (250 nm Figure 3-11(c)), some shallow pores start to develop. These shallow pores distribute randomly. When the guiding pore distance increases to 300 nm (Figure 3-11(d)), stable new pores form and distribute randomly on the patterned surface.

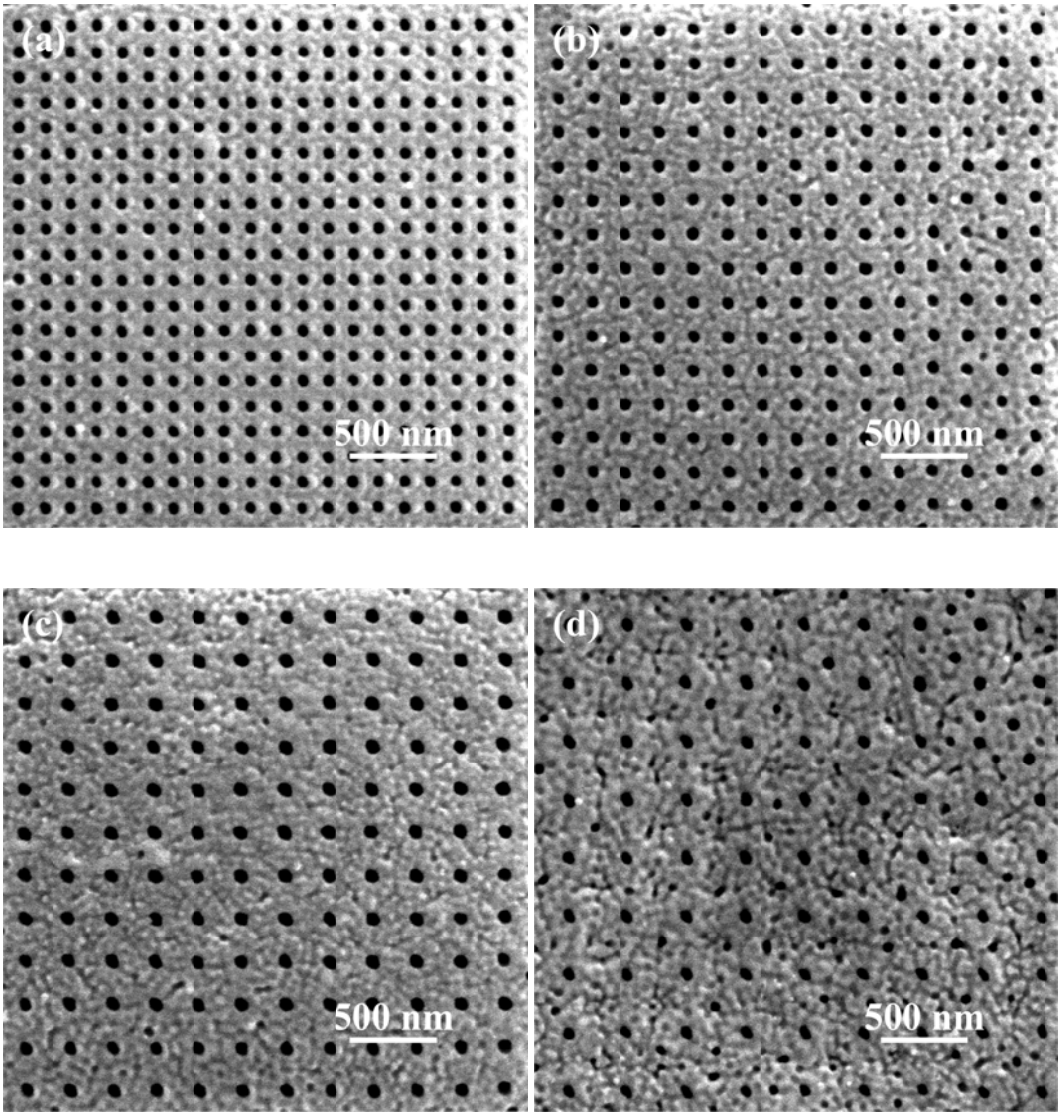

Figure 3-11 Anodic TiO_2 nanotubes under square guiding patterns. The guiding interpore distance is (a) 150 nm, (b) 200 nm, (c) 250 nm, and (d) 300 nm.

3.4 Summary and further directions

In this chapter, four different surface polished samples, as-received, chemically polished, mechanically polished, and electropolished samples, are investigated for the influence of the polishing effect on the anodic TiO_2 nanotube morphologies. The as-received and mechanically polished samples show clear nanotube morphologies. For chemically polished and electropolished samples, a condensed oxide layer lies on top of the nanotube. Of all these polishing methods, electropolishing provides a desired smooth surface for guided anodization. Hexagonal pore arrangements with different interpore distances are pre-patterned on the electropolished Ti surface. They can further develop into the substrate and the arrangements keep well. As a result, ordered TiO_2 natotube arrays are created by a direct FIB guided anodization. They may contribute to novel applications. FIB guided anodization is also proved again to be an effective guiding method.

Further work will be carried out based on the achieved results. Nanotube development mechanism under guided anodization is still unclear. Other variables, such as FIB patterning condition, applied voltage, anodization time, electrolyte optimization, can be tried to fully understand the guided anodization process. Elements that have a major effect on the anodization should be clarified. We can try guiding patterns other than hexagons to reveal the relationship between guiding and self-organization effect.

3.5 References

1. Albu, S.P., A. Ghicov, J.M. Macak, R. Hahn, and P. Schmuki, Self-organized, free-standing TiO2 nanotube membrane for flow-through photocatalytic applications. *Nano Letters*, 2007. **7**(5) p. 1286-1289.
2. Macak, J.M., M. Zlamal, J. Krysa, and P. Schmuki, Self-organized TiO2 nanotube layers as highly efficient photocatalysts. *Small*, 2007. **3**(2) p. 300-304.
3. Balaur, E., J.M. Macak, L. Taveira, and P. Schmuki, Tailoring the wettability of TiO2 nanotube layers. *Electrochemistry Communications*, 2005. **7**(10) p. 1066-1070.
4. Balaur, E., J.M. Macak, H. Tsuchiya, and P. Schmuki, Wetting behaviour of layers of TiO2 nanotubes with different diameters. *Journal of Materials Chemistry*, 2005. **15**(42) p. 4488-4491.
5. Zheng, Q., B.X. Zhou, J. Bai, L.H. Li, Z.J. Jin, J.L. Zhang, J.H. Li, Y.B. Liu, W.M. Cai, and X.Y. Zhu, Self-organized TiO2 nanotube array sensor for the determination of chemical oxygen demand. *Advanced Materials*, 2008. **20**(5) p. 1044.
6. Mor, G.K., M.A. Carvalho, O.K. Varghese, M.V. Pishko, and C.A. Grimes, A room-temperature TiO2-nanotube hydrogen sensor able to self-clean photoactively from environmental contamination. *Journal of Materials Research*, 2004. **19**(2) p. 628-634.
7. Fujishima, A. and K. Honda, Electrochemical Photolysis of Water at a Semiconductor Electrode. *Nature*, 1972. **238** p. 37-38.

8. Gong, D., C.A. Grimes, O.K. Varghese, W.C. Hu, R.S. Singh, Z. Chen, and E.C. Dickey, Titanium oxide nanotube arrays prepared by anodic oxidation. *Journal of Materials Research*, 2001. **16**(12) p. 3331-3334.

9. Bauer, S., S. Kleber, and P. Schmuki, TiO2 nanotubes: Tailoring the geometry in H3PO4/HF electrolytes. *Electrochemistry Communications*, 2006. **8**(8) p. 1321-1325.

10. Beranek, R., H. Hildebrand, and P. Schmuki, Self-organized porous titanium oxide prepared in H2SO4/HF electrolytes. *Electrochemical and Solid State Letters*, 2003. **6**(3) p. B12-B14.

11. Macak, J.M., H. Tsuchiya, and P. Schmuki, High-aspect-ratio TiO2 nanotubes by anodization of titanium. *Angewandte Chemie-International Edition*, 2005. **44**(14) p. 2100-2102.

12. Macak, J.M., H. Tsuchiya, L. Taveira, S. Aldabergerova, and P. Schmuki, Smooth anodic TiO2 nanotubes. *Angewandte Chemie-International Edition*, 2005. **44**(45) p. 7463-7465.

13. Albu, S.P., A. Ghicov, J.M. Macak, and P. Schmuki, 250 mu m long anodic TiO2 nanotubes with hexagonal self-ordering. *Physica Status Solidi-Rapid Research Letters*, 2007. **1**(2) p. R65-R67.

14. Wang, J. and Z.Q. Lin, Freestanding TiO2 nanotube arrays with ultrahigh aspect ratio via electrochemical anodization. *Chemistry of Materials*, 2008. **20**(4) p. 1257-1261.

15. Macak, J.M. and P. Schmuki, Anodic growth of self-organized anodic TiO2 nanotubes in viscous electrolytes. *Electrochimica Acta*, 2006. **52**(3) p. 1258-1264.

16. Paulose, M., K. Shankar, S. Yoriya, H.E. Prakasam, O.K. Varghese, G.K. Mor, T.A. Latempa, A. Fitzgerald, and C.A. Grimes, Anodic growth of highly ordered TiO2 nanotube arrays to 134 mu m in length. *Journal of Physical Chemistry B*, 2006. **110**(33) p. 16179-16184.

17. Shankar, K., G.K. Mor, H.E. Prakasam, S. Yoriya, M. Paulose, O.K. Varghese, and C.A. Grimes, Highly-ordered TiO2 nanotube arrays up to 220 mu m in length: use in water photoelectrolysis and dye-sensitized solar cells. *Nanotechnology*, 2007. **18**(6).

18. Macak, J.M., S. Aldabergerova, A. Ghicov, and P. Schmuki, Smooth anodic TiO2 nanotubes: annealing and structure. *Physica Status Solidi a-Applications and Materials Science*, 2006. **203**(10) p. R67-R69.

19. Albu, S.R., D. Kim, and P. Schmuki, Growth of aligned TiO2 bamboo-type nanotubes and highly ordered nanolace. *Angewandte Chemie-International Edition*, 2008. **47**(10) p. 1916-1919.

20. Berger, S., J. Kunze, P. Schmuki, A.T. Valota, D.J. LeClere, P. Skeldon, and G.E. Thompson, Influence of Water Content on the Growth of Anodic TiO2 Nanotubes in Fluoride-Containing Ethylene Glycol Electrolytes. *Journal of the Electrochemical Society*, 2010. **157**(1) p. C18-C23.

21. Zhu, K., N.R. Neale, A. Miedaner, and A.J. Frank, Enhanced charge-collection efficiencies and light scattering in dye-sensitized solar cells using oriented TiO2 nanotubes arrays. *Nano Letters*, 2007. **7**(1) p. 69-74.

22. Mor, G.K., K. Shankar, M. Paulose, O.K. Varghese, and C.A. Grimes, Use of highly-ordered TiO2 nanotube arrays in dye-sensitized solar cells. *Nano Letters*, 2006. **6**(2) p. 215-218.

23. Ghicov, A., H. Tsuchiya, R. Hahn, J.M. Macak, A.G. Munoz, and P. Schmuki, TiO2 nanotubes: H+ insertion and strong electrochromic effects. *Electrochemistry Communications*, 2006. **8**(4) p. 528-532.

24. Hahn, R., A. Ghicov, H. Tsuchiya, J.M. Macak, A.G. Munoz, and P. Schmuki, Lithium-ion insertion in anodic TiO2 nanotubes resulting in high electrochromic contrast. *Physica Status Solidi a-Applications and Materials Science*, 2007. **204**(5) p. 1281-1285.

25. Paramasivam, I., J.M. Macak, A. Ghicov, and P. Schmuki, Enhanced photochromism of Ag loaded self-organized TiO2 nanotube layers. *Chemical Physics Letters*, 2007. **445**(4-6) p. 233-237.

26. Bauer, S., J. Park, K. von der Mark, and P. Schmuki, Improved attachment of mesenchymal stem cells on super-hydrophobic TiO2 nanotubes. *Acta Biomaterialia*, 2008. **4**(5) p. 1576-1582.

27. Dalvie, S.K. and R.E. Baltus, Transport Studies with Porous Alumina Membranes. *Journal of Membrane Science*, 1992. **71**(3) p. 247-255.

28. Paramasivalm, I., J.M. Macak, and P. Schmuki, Photocatalytic activity of TiO2-nanotube layers loaded with Ag and Au nanoparticles. *Electrochemistry Communications*, 2008. **10**(1) p. 71-75.

29. Zlamal, M., J.M. Macak, P. Schimuki, and J. Krysa, Electrochemically assisted photocatalysis on self-organized TiO2 nanotubes. *Electrochemistry Communications*, 2007. **9**(12) p. 2822-2826.

30. Park, J., S. Bauer, K. von der Mark, and P. Schmuki, Nanosize and vitality: TiO2 nanotube diameter directs cell fate. *Nano Letters*, 2007. **7**(6) p. 1686-1691.

31. Ong, K.G., O.K. Varghese, G.K. Mor, and C.A. Grimes, Numerical simulation of light propagation through highly-ordered titania nanotube arrays: Dimension optimization for improved photoabsorption. *Journal of Nanoscience and Nanotechnology*, 2005. **5**(11) p. 1801-1808.

32. Chen, B., K. Lu, and Z. Tian, Gradient and alternating diameter nanopore templates by focused ion beam guided anodization. *Electrochimica Acta*, 2010. **56**(1) p. 435-440.

33. Seyeux, A., S. Berger, D. LeClere, A. Valota, P. Skeldon, G.E. Thompson, J. Kunze, and P. Schmuki, Influence of Surface Condition on Nanoporous and Nanotubular Film Formation on Titanium. *Journal of the Electrochemical Society*, 2009. **156**(2) p. K17-K22.

34. Shin, Y. and S. Lee, Self-Organized Regular Arrays of Anodic TiO2 Nanotubes. *Nano Letters*, 2008. **8**(10) p. 3171-3173.

35. Lelonek, M., O. Kopp, and M. Knoll, Pore bifurcation, growth and pore termination in nanoporous alumina with concave and convex surfaces. *Electrochimica Acta*, 2009. **54**(10) p. 2805-2809.

36. Lee, W., R. Ji, U. Gosele, and K. Nielsch, Fast fabrication of long-range ordered porous alumina membranes by hard anodization. *Nature Materials*, 2006. **5**(9) p. 741-747.

Chapter 4 Summary and future work

4.1 Summary of current work

In this study, FIB guided anodization is introduced and discussed. The guiding effect is investigated in porous AAO and anodic TiO_2 nanotubes. Ordered periodic porous AAO is synthesized successfully. Electrical field and mechanical stress are two important elements that govern the anodization process and final result. For a given voltage, interpore distance is one important parameter for guided anodization. By carefully varying the interpore distance, new small pores can be generated and their locations and shapes are able to be predicted. It provides a potential practical way to create more complex patterns. The guiding process may even overcome the grain boundary effect. Ordered TiO_2 nanotubes can also be obtained via FIB guided anodization. Different polishing conditions are discussed for their influences on the anodic morphologies. Of all of them, the electropolishing provides a desired smooth Ti surface for further FIB guiding works. Layered structure is found and discussed when obtaining a cross-section by cutting though the anodic TiO_2 substrate. Experimental results prove that FIB guided anodization is an effective direct guiding method in this research area.

4.2 Suggestion for future work

Based on the obtained experimental results, I suggest that some further work can be done. The guided anodization mechanism, especially the formation of the anodic TiO_2

nanotubes needs to be clarified. More variables, such as applied voltage, anodization time, and electrolyte optimization, can be tried.

Since nanopore/nanotube membrane arrays with ordered structure are successfully prepared, other work that relate to this structure can be done, such as using ordered AAO as a template, filled in with other materials. The light scattering/reflection through an nanostructured surface can be investigated.

Appendix:

Derivation of effective dielectric permittivity

A column capacitor model can be used to calculate the effective dielectric permittivity ε. ε_1, ε_2 represent the dielectric permittivity of Al_2O_3 and Al respectively. R_1 is the pore diameter and R_2 is the distance from the pore center to the oxide barrier layer outer boundary. Assuming the composition of the inner oxide layer side (R_1) is pure Al_2O_3 and that of the outer oxide layer side (R_2) is pure Al; the composition between R_1 and R_2 is AlO_x ($0<x<1.5$), changing linearly from Al_2O_3 to Al with R; $\varepsilon(R)$ changes linearly from the inner ring R_1 to the outer ring R_2:

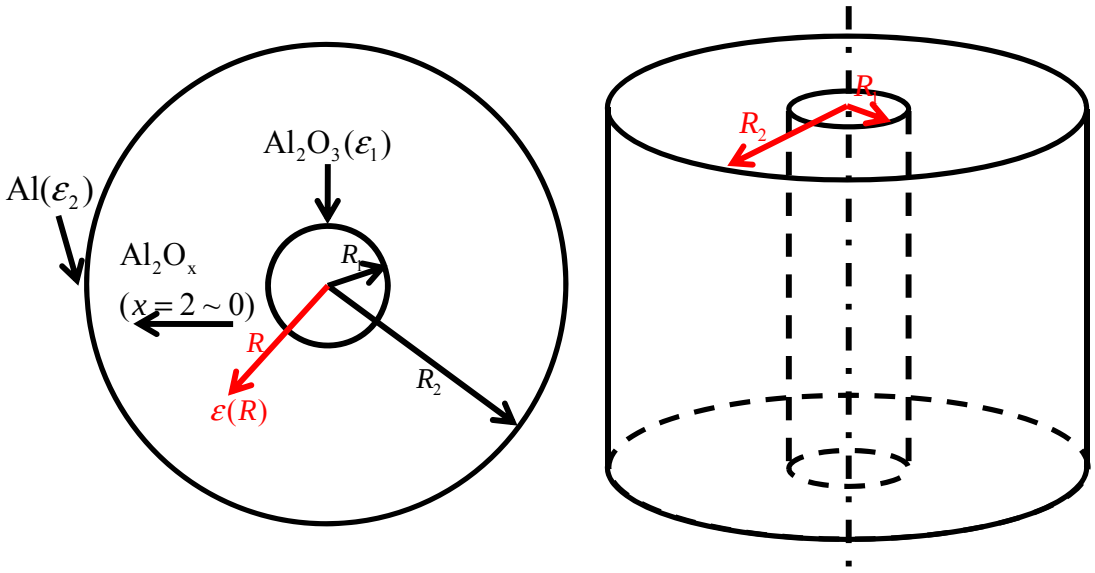

$$\frac{\varepsilon(R)-\varepsilon_1}{\varepsilon_2-\varepsilon_1}=\frac{R-R_1}{R_2-R_1}$$

$$\varepsilon(R)=\frac{(R-R_1)(\varepsilon_2-\varepsilon_1)}{(R_2-R_1)}+\varepsilon_1$$

$$= \frac{R(\varepsilon_2 - \varepsilon_1)}{R_2 - R_1} - \frac{R_1\varepsilon_2 - R_2\varepsilon_1}{R_2 - R_1}$$

$$= \frac{R(\varepsilon_2 - \varepsilon_1)}{R_2 - R_1} + C$$

$$(C = -\frac{R_1\varepsilon_2 - R_2\varepsilon_1}{R_2 - R_1})$$

Assuming an electrical charge accumulates from the pore center axis to the wall of the inner ring, with a uniform line electron density λ along the axis, following the Gauss theory, the voltage between the R_1 ring and the R_2 ring is:

$$\mathrm{U} = \int_{R_1}^{R_2} \frac{\lambda}{2\pi\varepsilon(R)} \times \frac{1}{R} dR$$

$$= \frac{\lambda}{2\pi} \int_{R_1}^{R_2} \frac{1}{\frac{R(\varepsilon_2 - \varepsilon_1) + C(R_2 - R_1)}{R_2 - R_1}} \times \frac{1}{R} dR$$

$$= \frac{\lambda(R_2 - R_1)}{2\pi(\varepsilon_2 - \varepsilon_1)} \int_{R_1}^{R_2} \frac{1}{R + C'} \times \frac{1}{R} dR$$

$$(C' = \frac{C(R_2 - R_1)}{\varepsilon_2 - \varepsilon_1})$$

For the $\int_{R_1}^{R_2} \frac{1}{R + C'} \times \frac{1}{R} dR$ part:

$$\int_{R_1}^{R_2} \frac{1}{R + C'} \times \frac{1}{R} dR$$

$$= -\frac{1}{C'} \ln \frac{R + C'}{R} \Big|_{R_1}^{R_2}$$

$$= -\frac{1}{C'} (\ln \frac{R_2 + C'}{R_2} - \ln \frac{R_1 + C'}{R_1})$$

$$= -\frac{\varepsilon_2 - \varepsilon_1}{R_2 \varepsilon_1 - R_1 \varepsilon_2} \ln \frac{R_1 \varepsilon_2}{R_2 \varepsilon_1}$$

For the total equation:

$$U = \frac{\lambda (R_2 - R_1)}{2\pi (\varepsilon_2 - \varepsilon_1)} \int_{R_1}^{R_2} \frac{1}{R + C'} \times \frac{1}{R} dR$$

$$= -\frac{\lambda (R_2 - R_1)}{2\pi (R_2 \varepsilon_1 - R_1 \varepsilon_2)} \ln \frac{R_1 \varepsilon_2}{R_2 \varepsilon_1}$$

Let $\varepsilon_1 = \varepsilon_2 = \varepsilon$, which means a homogeneous dielectric material:

$$U = \frac{\lambda}{2\pi \varepsilon} \ln \frac{R_2}{R_1}$$

So the effective dielectric permittivity can be obtained as follows:

$$\frac{\lambda}{2\pi \varepsilon} \ln \frac{R_2}{R_1} = -\frac{\lambda (R_2 - R_1)}{2\pi (R_2 \varepsilon_1 - R_1 \varepsilon_2)} \ln \frac{R_1 \varepsilon_2}{R_2 \varepsilon_1}$$

$$\varepsilon = \frac{(R_2 \varepsilon_1 - R_1 \varepsilon_2) \ln \frac{R_2}{R_1}}{(R_2 - R_1) \ln \frac{R_2 \varepsilon_1}{R_1 \varepsilon_2}}$$